**FEDERAL UNIVERSITY OF TECHNOLOGY - PARANÁ**
**DEPARTMENT OF MECHANICAL ENGINEERING**
**POSTGRADUATE PROGRAMME IN MECHANICAL AND MATERIALS ENGINEERING**

**VINICIUS DAROZ**

# LARGE-EDDY SIMULATION OF AN ANNULAR-SECTOR DUCT ROTATING IN PARALLEL MODE

A thesis submitted as partial fulfilment for the degree of Master of Science

**CURITIBA**
**2018**

**VINICIUS DAROZ**

# LARGE-EDDY SIMULATION OF AN ANNULAR-SECTOR DUCT ROTATING IN PARALLEL MODE

MSc thesis presented to the Postgraduate Programme in Mechanical and Materials Engineering - PPGEM from the Federal University of Technology - Paraná, as partial fulfilment of the requirements for the degree of Master of Science.

Supervisor: Prof. Dr. Admilson T. Franco
Co-supervisor: Prof. Dr. Eduardo M. Germer
Co-supervisor: Diogo B. Pitz, PhD

**CURITIBA**
**2018**

**Dados Internacionais de Catalogação na Publicação**

D224L 2018

Daroz, Vinicius
Large-Eddy Simulalation of an Annular-sector Duct Rotating in Parallel Mode / Vinicius Daroz.-- 2018.
127 f.: il.; 30 cm.

Disponível também via World Wide Web.
Texto em inglês, com resumo em português.
Dissertação (Mestrado) - Universidade Tecnológica Federal do Paraná. Programa de Pós-Graduação em Engenharia Mecânica e de Materiais, Curitiba, 2018
Bibliografia: p. 113-118

1. Simulação de grandes escalas. 2. Turbulência. 3. Escoamento. 4. Engenharia térmica. 5. Engenharia mecânica - Dissertações. I. Franco, Admilson Teixeira, orient. II. Germer, Eduardo Matos, coorient. III. Pitz, Diogo Berta, coorient. IV. Universidade Tecnológica Federal do Paraná - Programa de Pós-Graduação em Engenharia Mecânica e de Materiais, inst. V. Título.

CDD: Ed. 22 -- 620.1

Biblioteca Central da UTFPR, Câmpus Curitiba
Lucia Ferreira Littiere – CRB 9/1271

Ministério da Educação
Universidade Tecnológica Federal do Paraná
Diretoria de Pesquisa e Pós-Graduação

# TERMO DE APROVAÇÃO DE DISSERTAÇÃO Nº 321

A Dissertação de Mestrado intitulada **Large-Eddy Simulation of an Annular Sector Duct Rotating in Parallel Mode**, defendida em sessão pública pelo Candidato **Vinicius Daroz**, no dia **03 de maio de 2018**, foi julgada para a obtenção do título de Mestre em Engenharia, área de concentração: Engenharia Térmica, e aprovada em sua forma final, pelo Programa de Pós-Graduação em Engenharia Mecânica e de Materiais – PPGEM.

BANCA EXAMINADORA:
Prof. Dr. Admilson Teixeira Franco - UTFPR
Prof. Cezar Otaviano Ribeiro Negrão, Ph.D. - UTFPR
Prof. Dr. Cesar José Deschamps - UFSC
Prof. Dr. Carlos Henrique Marchi - UFPR

A via original deste documento encontra-se arquivada na Secretaria do Programa, contendo a assinatura da Coordenação após a entrega da versão corrigida do trabalho.

Curitiba, _____de _____de 20___.

Carimbo e assinatura do Coordenador do Programa

_____

# ACKNOWLEDGEMENTS

In first place, I aknowledge my parents for teaching me the most precious lesson: the value of knowledge. They always encouraged me and provide me with the necessary tools to build my life up to here.

To my supervisor, Admilson T. Franco, who has been guiding me since I was first shown the scientific world and has been always available for encouraging conversations both in personal and professional aspects.

To my co-supervisor, Eduardo M. Germer, for sharing his experience with numerical methods and being supportive all along the way.

To my friend and co-supervisor, Diogo B. Pitz, crucial in the every stage of this research. His availability and knowledge were fundamental to accomplish the solution of the problem.

Finally, I thank my love Andressa, with whom I have always been able to share my accomplishments but also my failures. Her love and affection during all these years were undoubtedly key to this additional step in my life.

*Vether it's worth goin' through so much, to learn so little,*
*as the charity-boy said ven he got to the end of the alphabet,*
*is a matter o' taste.*
Charles Dickens, Pickwick Papers

DAROZ, VINICIUS. **Large-Eddy Simulalation of an Annular-sector Duct Rotating in Parallel Mode**. Dissertação (Mestrado em Engenharia) – Programa de Pós-Graduação em Engenharia Mecânica e de Materiais, Universidade Tecnológica Federal do Paraná, Curitiba, 128 páginas, 2018.

## ABSTRACT

In this research the turbulent flow within an annular-sector duct rotating about a parallel axis is numerically solved using large-eddy simulation (LES). The study is motivated by the lack of in-depth understanding of the interplay between rotation- and shear-induced phenomena over turbulence-related quantities for a problem that has vast applicability in rotating machinery and internal cooling systems. As a first approach, the solution of the problem is performed with the aid of a commercial computational fluid dynamics (CFD) code. The numerical procedure and solution methodology were verified against reference solution data in order to grant reliability to the obtained results. The annular-sector problem was investigated by means of hydrodynamical and geometrical parameters. First, the swirl parameter, which represents the ratio of rotational to axial Reynolds number, was found to cause substantial change in the mean flow profiles and turbulent quantities. Interestingly, increasing rotation promotes a stabilising effect in the flow bulk region. On the other hand, rotation increases the overall friction factor. The duct apex angle effect was found to alter both primary and secondary motion patterns. The ratio of the inner to outer radius influence resembles that of the apex angle. Intriguingly, the friction factor presented a minimum point suggesting that an optimal hydrodynamical configuration may be obtained.

**Keywords:** Large-Eddy Simulation, turbulence, parallel-mode rotation, annular-sector.

DAROZ, VINICIUS. **Large-Eddy Simulalation of an Annular-sector Duct Rotating in Parallel Mode**. Dissertação (Mestrado em Engenharia) – Programa de Pós-Graduação em Engenharia Mecânica e de Materiais, Universidade Tecnológica Federal do Paraná, Curitiba, 128 páginas, 2018.

## RESUMO

No presente trabalho, o escoamento em regime turbulento através de um duto com seção transversal com formato de um setor anular, com rotação imposta ao redor de um eixo paralelo, é numericamente resolvido por meio da simulação das grandes escalas (Large-Eddy Simulation). O estudo é motivado pela falta de conhecimento do efeito competitivo entre fenômenos induzidos pela rotação e/ou cisalhamento sobre o campo médio de escoamento e quantidades turbulentas, para um problema que é vastamente empregado em máquinas de fluxo e sistemas de arrefecimento interno. Como uma primeira abordagem, a solução do problema é obtida através de um código comercial de dinâmica dos fluidos computacional (DFC). O procedimento numérico e metodologia de solução foram verificados com base em solução de referência encontradas na literatura, conferindo confiabilidade aos resultados obtidos. O problema do setor anular foi investigado por meio de parâmetros hidrodinâmicos e geométricos. Primeiramente, o parâmetro de swirl, que representa a razão entre os números de Reynolds rotacional a axial, causou alterações substanciais no campo médio e quantidades turbulentas. Curiosamente, aumentando-se a rotação leva a uma estabilização do escoamento na região central do duto. Por outro lado, o aumento da rotação aumenta o fator de atrito global. Em seguida, o efeito do ângulo do setor anular foi considerado. Sua modificação altera completamente o padrão dos escoamentos primário e secundário. Por último, a razão de raios do duto apresenta influência semelhante àquela do ângulo do setor anular. É intrigante, no entanto, que o fator de atrito apresentou um ponto mínimo, sugerindo que uma configuração ótima, hidrodinamicamente falando, pode ser encontrada.

**Palavras-chave:** Simulação das grandes escalas, turbulência, rotação em modo paralelo, setor anular.

# LIST OF FIGURES

# LIST OF TABLES

# LIST OF ABBREVIATIONS AND ACRONYMS

| | |
|---|---|
| CFD | Computational Fluid Dynamics |
| CPU | Central Processing Units |
| DNS | Direct Numerical Simulation |
| LDV | Laser Doppler Velocimetry |
| LES | Large-Eddy Simulation |
| PIV | Particle Image Velocimetry |
| RANS | Reynolds-Averaged Navier-Stokes |
| RANSE | Reynolds-Averaged Navier-Stokes Equations |
| RRF | Rotating Reference Frame |
| RSM | Reynolds Stress Model |
| WALE | Wall Adapting Local Eddy-viscosity |
| SEM | Synthetic Eddy Method |
| SGS | Subgrid-Scale |
| SST | Shear Stress Transport |

# NOMENCLATURE

## Roman letters and symbols

| | | |
|---|---|---|
| $u_i$ | Velocity component in the $i^{\text{th}}$ direction | $[m\ s^{-1}]$ |
| $x_i$ | $i^{\text{th}}$ direction in a Cartesian coordinate system | $[m]$ |
| $t$ | Time | $[s]$ |
| $\delta t$ | Time-step | $[s]$ |
| $D_h$ | Hydraulic diameter $\frac{4R(1-\eta)}{1+\frac{2}{\alpha}\frac{1-\eta}{1+\eta}}$ | $[m]$ |
| $H$ | Annular-sector height | $[m]$ |
| $H^*$ | Annular-sector normalised height $H/D_h$ | $[m]$ |
| $p$ | Pressure | $[Pa]$ |
| $R$ | Radius | $[m]$ |
| $r$ | Radial coordinate | $[m]$ |
| $r^*$ | Non-dimensional radial coordinate $(r/R-\eta)/(1-\eta)$ | $[-]$ |
| $R$ | Two-point correlation function | $[-]$ |
| $U$ | Characteristic velocity | $[m\ s^{-1}]$ |
| $u$ | Large eddy velocity scale | $[m\ s^{-1}]$ |
| $l$ | Large eddy length scale | $[m]$ |
| $k$ | Turbulent kinetic energy per unit mass | $[m^2\ s^{-2}]$ |
| $G$ | Filter function | $[-]$ |
| $V$ | Computational cell volume | $[m^3]$ |
| $f$ | Generic flow quantity | $[-]$ |
| $C_S$ | Smagorinsky model constant | $[-]$ |
| $z$ | Axial coordinate | $[m]$ |

## Vectors and Tensors

| | | |
|---|---|---|
| $\mathbf{a}$ | Surface area vector | $[m^2]$ |
| $\mathbf{g}$ | Gravity vector | $[m\ s^{-2}]$ |
| $\mathbf{\Omega}$ | Rotation vector | $[rad\ s^{-1}]$ |
| $\mathbf{R}$ | Reynolds stress tensor | $[Pa]$ |
| $S_{ij}$ | Rate of strain tensor | $[s^{-1}]$ |
| $\mathbf{T}$ | Viscous stress tensor | $[Pa]$ |
| $\mathbf{T}^{\text{SGS}}$ | Subgrid-scale stress tensor | $[Pa]$ |
| $\mathbf{u}$ | Velocity vector | $[m\ s^{-1}]$ |
| $\mathbf{x}, \mathbf{r}$ | Position vector | $[m]$ |

## Greek letters

| | | |
|---|---|---|
| $\alpha$ | Annular-sector apex angle | $[deg]$ |

| | | |
|---|---|---|
| $\theta$ | Tangential coordinate | $[rad]$ |
| $\epsilon$ | Rate of dissipation of turbulent kinetic energy | $[m^2\ s^{-3}]$ |
| $\phi$ | Generic scalar function | |
| $\tau_w$ | Wall shear stress magnitude | $[Pa]$ |
| $\rho$ | Density | $[kg\ m^{-3}]$ |
| $\nabla$ | Nabla operator | $[-]$ |
| $\nabla^2$ | Laplacian operator | $[-]$ |
| $\nu$ | Kinematic viscosity | $[m^2\ s^{-1}]$ |
| $\mu$ | Dynamic viscosity | $[Pa\ s]$ |
| $\omega$ | Reference frame rotation speed | $[rad\ s^{-1}]$ |
| $\Omega$ | Rotation speed | $[rad\ s^{-1}]$ |
| $\vartheta$ | Smallest eddies velocity scale | $[m\ s^{-1}]$ |
| $\eta$ | Smallest eddies length scale | $[m]$ |
| $\eta$ | Annular-sector radius ratio | $[-]$ |
| $\ell$ | Characteristic length | $[m]$ |
| $\kappa$ | Von Kármán constant | $[-]$ |
| $\delta$ | Annular-sector radial gap | $[m]$ |
| $\delta_{ij}$ | Kronecker delta | $[-]$ |
| $\Pi$ | Rate of transfer of kinetic energy per unit mass | $[m^2\ s^{-3}\ kg^{-1}]$ |

**Non-dimensional parameters**

| | | |
|---|---|---|
| $Re$ | Reynolds number $8\rho U^2/\tau_w$ | $[-]$ |
| $Re_\Omega$ | Rotational Reynolds number $\Omega Rd/nu$ | $[-]$ |
| $Re_\omega$ | Annular-sector rotational Reynolds number $\omega D_h^2/\nu$ | $[-]$ |
| $Re_b$ | Annular-sector bulk Reynolds number $W_b D_h/\nu$ | $[-]$ |
| $Re_\eta$ | Smallest eddies Reynolds number $\vartheta\eta/\nu$ | $[-]$ |
| $Ta$ | Taylor number $\Omega^2 d^3 R/\nu^2$ | $[-]$ |
| $\Gamma$ | Swirl parameter $Re_\omega/Re_b$ | $[-]$ |

**Superscripts**

| | |
|---|---|
| $(\,)'$ | Fluctuation or modelled subgrid-scale field |
| $\overline{(\,)}$ | Time-averaged quantity, space-filtered quantity |
| $\widetilde{\overline{(\,)}}$ | Test-filter space-filtered quantity |
| $(\,)^{\mathrm{SGS}}$ | Related to subgrid-scale |
| $(\,)^+$ | Measured in wall units |
| $(\,)^R$ | Related to Reynolds stresses |
| $(\,)^T$ | Total |
| $(\,)^{\mathrm{T}}$ | Transpose |
| $(\,)^*$ | Characteristic scale |

## Subscripts

| | |
|---|---|
| $(\,)_w$ | Evaluated at the wall |
| $(\,)_t$ | Turbulent |
| $(\,)_\tau$ | Defined in terms of the friction velocity |
| $(\,)_\omega$ | Defined in terms of the reference frame rotation speed |
| $(\,)_\Omega$ | Defined in terms of the rotation speed |
| $(\,)_{\mathrm{SGS}}$ | Related to the subgrid-scale |

# CONTENTS

# 1 Introduction

*Turbulence is all around us. The air flowing in and out of our lungs is turbulent, as is the natural convection in the room in which you sit. Glance outside; the wind which gusts down the street is turbulent, and it is turbulence that disperses the pollutants, which belch from the rear of motor cars, saving us from asphyxiation. Turbulence controls the drag on cars, aeroplanes, and bridges, and it dictates the weather through its influence on large-scale atmospheric and oceanic flows. The liquid core of the earth is turbulent, and it is this turbulence that maintains the terrestrial magnetic field against the natural forces of decay. Even solar flares are a manifestation of turbulence, since they are triggered by vigorous motion on the surface of the sun. It is hard not to be intrigued by a subject which pervades so many aspects of our lives.*

Davidson (2004)

## 1.1 Context

Turbulent flows have always been of considerable engineering and scientific interest. In nature and industrial applications, flows are mostly turbulent, motivating researchers who devoted their lives to scratch the surface of a topic that remains only partially understood. The intrinsic intermittency and scale spectra of turbulent flows have been slowing down its comprehension since it was first formalized. The fundamental structures of turbulence are not easy to measure in experiments and direct solutions of the Navier-Stokes equations are still limited by advances in numerical methods and computer hardware.

Despite the advances in experimental techniques, numerical approaches have become very attractive as they reduce testing and prototyping costs. Even with the aforementioned limitations, the present day computing power and models/methodologies provide great insight into the overall behaviour of turbulent flows. Associated with the fast-growing need for more efficiency in industrial processes, solutions for environmental issues, aerodynamic optimisations, among others, numerical simulations have been key tools on enhancing our understanding over several fields of science.

The particular case of wall-bounded turbulent flows in rotating geometries may be found in some of the most important machinery of the modern society. In heat exchangers, turbomachinery, chemical reactors, electric generators, to name a few examples, rotation-induced effects increase the complexity of flow and restrict the available approaches to face the problem. Experimental rigs become hard to design and simplistic approaches to turbulence, e.g. standard eddy-viscosity models, do not account for rotation and curvature effects unless ad-hoc corrections are used.

When such effects are taken into account, additional stresses due to centrifugal and Coriolis forces become present. These stresses weaken even more the Boussinesq hypothesis for the eddy viscosity, which in spite of providing satisfactory predictions for simple flows, is not valid and is still the core assumption of most turbulence models (SCHMITT, 2007). Additionally, secondary flow may also develop and compete with the primary flow for energy supply. The results appear as collateral effects in what may be the main interests of engineering purposes: head loss and heat transfer. The comprehension of such

interferences on the overall behaviour of the flow and heat transfer is of great importance to design and improve such machineries.

## 1.2 Problem description

For several reasons such as operational velocities, combustion, friction, electric heating, etc., most of the rotating equipments have to be cooled by means of a coolant fluid, which is chosen in accordance to the application. In some of them, the flow takes place within channels that are built in parallel to the rotation axis. These channels happen to be of the most varied geometries (circular, square, rectangular, elliptical) and are responsible for dissipating heat, with attention paid to the required pressure drop, as well as in some cases, lubricate the rotating components. Since heat transfer is highly influenced by the flow dynamics, the correct prediction of the hydrodynamics is imperative to obtain assertive predictions of the thermal field (FÉNOT et al., 2011).

Specifically for rotor/stator geometries, in addition to rotation-induced effects, the flow experiences the presence of a stationary wall recalling the problem known as Taylor-Couette. If an axial flow is superimposed, it becomes a Taylor-Couette-Poiseuille problem. For the sake of the example, let the rotor/stator be represented by a common oil drill bit as illustrated in Fig. 1.1. In the illustration, the flow follows the direction indicated by the arrows in Fig. 1.1a. During its path through the drill bit, the fluid passes within baffles as in Fig. 1.1b where it has to extract heat in order to cool the drill bit, transport the cuttings and keep the pressure at the well walls as stable as possible (BOURGOYNE et al., 1986). The geometry of these channels may be represented by an annular-sector rotating about a parallel axis as in Fig. 1.1b. The stationary wall, representing the well wall, characterises the stator.

The full simulation (Direct Numerical Simulation) of complex geometries as the one shown in Fig. 1.1a is not feasible due to present days hardware limitations. Experiments regarding detailed flow dynamics are not available and simplistic numerical approaches lack reliability for such complex flows. In this situation, from a numerical perspective, the solution is to stay in between both extremes, that is, not the full simulation neither the complete modelling. The simulation of the flow largest scales while modelling the smallest, known as Large-Eddy Simulation (LES), is a well-established technique that is intended to provide very accurate solutions with fair computational cost.

## 1.3 Objectives

The objective of this study is to perform a large-eddy simulation to investigate the Newtonian turbulent flow in an annular-sector rotating about a parallel axis, such as the one shown in Fig. 1.1b. The study is focused on the fundamental hydrodynamics and the comprehension of the flow mechanics in isothermal conditions. The numerical solution will be otained from the commercial CFD software STAR-CCM+ R.12.04.

The investigation will be carried out by varying the swirl parameter $\Gamma$, which represents the ratio between the axial and rotational Reynolds numbers. The competitive effect between rotation- and shear-

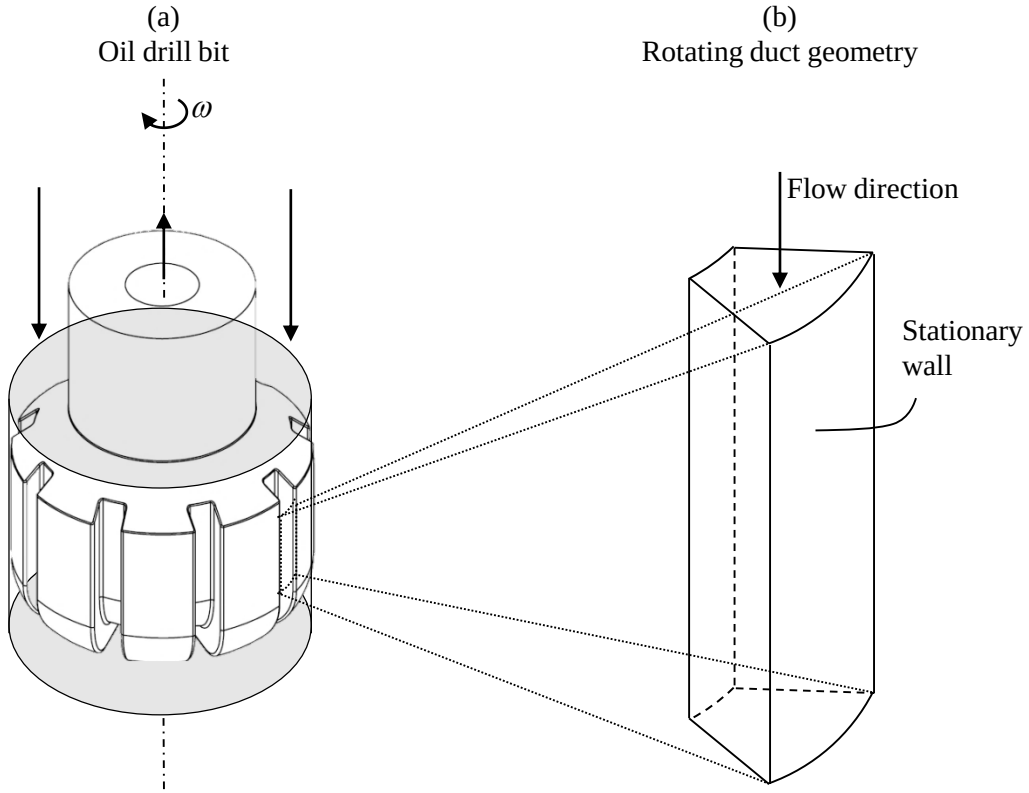


Figure 1.1 – Problem description. (a) Common oil drill bit geometry. (b) Rotating duct geometry.

induced forces will be analysed by varying the angular and radial gaps. Attention will be given to the influence of such parameters on the mean flow variables and turbulence statistics of first and second-order.

## 1.4 Document outline

Chapter 2 discusses fundamental concepts regarding turbulence as well as time- and space-averaging approaches to treat turbulence in the Navier-Stokes equations.

Chapter 3 brings the literature review, responsible for condensing the latest studies available in the literature so they will serve as guidance tools for the project development.

In Chapter 4, a formal description of the geometry, boundary conditions and simplifying assumptions are presented. The governing equations of the problem and its filtered counterpart are also presented. The LES formulation adopted to account for residual stresses is also explained.

Chapter 5 is devoted to show the way STAR-CCM+ deals with the chosen formulation. The employed numerical schemes are discussed and the grid construction process is detailed.

In Chapter 6, reference solution data found in the literature are compared with the results provided by STAR-CCM+ for different numerical configurations. The best setup is then employed to perform a grid-independence test.

Chapter 7 summarises the effect of the problem parameters in the mean flow and turbulence statistics.

Chapter 8 elucidates the drawn conclusions and future work ideas are also presented.

# 2 Theoretical Basis

This chapter discusses fundamental concepts regarding turbulence as well as time- and space-averaging approaches to treat turbulence in the Navier-Stokes equations.

## 2.1 The Navier-Stokes equation

The Navier-Stokes equation is known to model the motion of any constant-property Newtonian fluid, as long as the continuum hypothesis is respected (POPE, 2000). It is a second-order non-linear partial differential equation, based on Newton's second law, and relates the fluid portion acceleration to surface and body forces imposed on it. The derivation of the Navier-Stokes equation passes through the Stokes hypothesis for the second coefficient of viscosity, which informations can be found in White and Corfield (2006). For an incompressible isothermal fluid, the Navier-Stokes equation assumes the form:

$$\rho\left(\mathbf{u}\cdot\nabla\right)\mathbf{u} = \rho\mathbf{g} - \nabla p + \mu\nabla^2\mathbf{u} \tag{2.1}$$

where $\rho$ is fluid density, $\mathbf{u}$ is the velocity vector, $p$ is the pressure and $\mu$ is the fluid dynamic viscosity. In Eq. 2.1, the total acceleration of a fluid particle, left-hand side, is balanced by the interplay between pressure, gravity and viscous shear stress, on the right-hand side. The non-linear term on the left-hand side is responsible for the modelling capability of fascinating phenomena such as turbulence.

## 2.2 Turbulence

### 2.2.1 The experiments of Reynolds and Taylor

It has been known for a quite long time that the motion of a high-viscosity or slow-moving fluid tends to be well behaved or laminar. On the other hand, by reducing the fluid viscosity or if the motion happens more rapidly, the movement of the fluid becomes irregular, that is, turbulent. Taylor and Reynolds, by performing some simple experiments, illustrated this laminar-to-turbulent transition quite nicely (DAVIDSON, 2004), as described below.

Starting in 1883, Reynolds conducted an experiment in which water was put to flow in a pipe of a certain diameter. He introduced what he called a new form for the laws of resistance for all velocities and all diameters of pipes in a simple and elegant equation of only two terms. Years later, this equation was named after him and became the well known Reynolds number $Re$. With this equation, the flow regimes, laminar and turbulent, could then be distinguished by a certain value of $Re$. Reynolds pointed out that turbulence is a result of the natural amplification of instabilities which makes this type of flow very sensitive to disturbances such as initial conditions. In that time, Reynolds obtained laminar flow up to $Re \sim 13000$ arguing that there is a required amount of instabilities for turbulence to set in and that below a critical value of $Re$ turbulence decays (REYNOLDS, 1883). He was searching for a definite value, a

critical limit that would guarantee laminar flow and found that for straight smooth pipes there was one in fact. Reynolds stated that for $Re < 1900$ the flow would be stable while for $Re > 2000$ it would be unstable.

The Reynolds number can be expressed for any geometry as a relation between the dynamic pressure and the flow resistance, as shown on Eq. 2.2:

$$Re = \frac{8\rho U^2}{\tau_w}. \tag{2.2}$$

For pipe flow, it assumes a more usual form as given by Eq. 2.3 (WHITE; CORFIELD, 2006).

$$Re = \frac{\rho U d}{\mu} \tag{2.3}$$

In Eqs. 2.2 and 2.3, $\rho$ is the fluid density, $U$ is the characteristic velocity, $\tau_w$ is the wall shear stress, $\mu$ is the fluid dynamic viscosity and $d$ the pipe diameter.

In 1923 Taylor was dealing with another simple but intriguing experiment. With two concentric cylinders separated by a gap filled with fluid where the inner cylinder was put to rotate while the outer remained stationary, Taylor noted different flow regimes as illustrated in Fig. 2.1. At low rotational speeds, the fluid being dragged by the inner cylinder would act as expected creating a laminar motion within the gap. At a critical speed, however, toroidal vortices suddenly appeared creating a secondary motion superimposed on the primary circular motion (Fig. 2.1a). Nevertheless, the flow was still well behaved characterizing a flow pattern composed by axisymmetric toroidal structures known as Taylor vortices. The motion of a fluid particle may now be described by a helical path. Increasing the cylinder velocity, these structures became unstable losing their symmetry. Taylor described it as wavy vortices (Fig. 2.1b). Finally, when the inner cylinder reaches a certain critical velocity, the fluid breaks down into an eddy motion described as turbulent Taylor vortices (Fig. 2.1c) (DAVIDSON, 2004).

The secondary motion shown in Fig. 2.1a happens as a consequence of the centrifugal forces arising from rotation. Since there is a radial velocity gradient there is also a radial pressure gradient which until some critical point, balances the centrifugal force.

By extending Reynolds theory for straight smooth pipes, Taylor proposed a non-dimensional parameter which may be used to distinguish between the flow regimes shown in Fig. 2.1. The Taylor number $\mathrm{Ta}$ may be expressed as (DAVIDSON, 2004):

$$\mathrm{Ta} = \frac{\Omega^2 d^3 R}{\nu^2} \tag{2.4}$$

where $\nu$ is the kinematic viscosity of the fluid and the remaining variables are defined in Fig. 2.1. For rotating flows such as the one presented in in Fig. 2.1, it is also usual to define the rotational Reynolds number in the form:

$$Re_\Omega = \frac{\Omega R d}{\nu}. \tag{2.5}$$

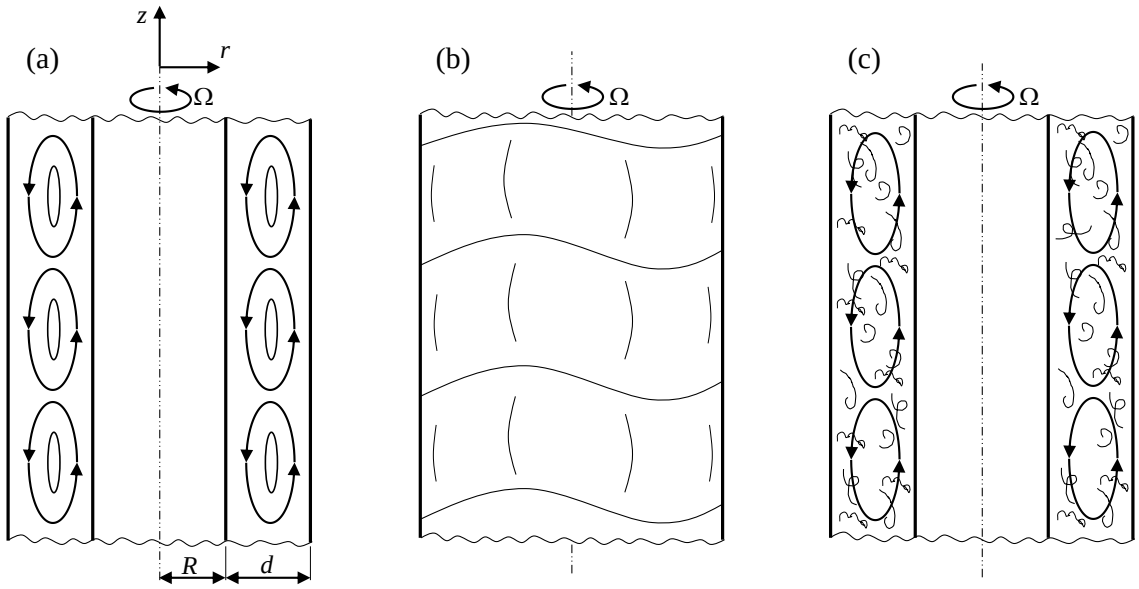


Figure 2.1 – Flow between concentric cylinders. Representation of the Taylor vortices. Source: Adapted from Davidson (2015).

### 2.2.2 A brief discussion on the scales of turbulence and the energy cascade

In the beginning of the XVI century, Leonardo da Vinci painted his observations of turbulence in which he described the eddying motion and variety of scales in the surface of a tank in which water was flowing in from a channel above the tank surface (ZOLLNER, 2004). For the subsequent centuries, scientists have been putting their efforts on the most common flows in nature, that is, turbulent flows.

Turbulence cannot exist by itself, in the sense that it requires a continuous supply of energy. In three-dimensional turbulence, the energy supply comes from the mean flow and/or body forces, creating eddies that inherit the mean flow scale $l$ and velocity $u$. These large eddies are also subjected to instabilities and soon break-up into smaller eddies and so on, cascading energy to smaller and smaller structures. This process continues until viscosity plays its role dissipating this energy by the action of viscous stresses. This process is schematically illustrated in Fig. 2.2 in which the flux of kinetic energy is directed from the large, energy-containing eddies, referred to as first instabilities, to the small, energy-dissipating eddies of length scale $\eta$ and velocity scale $\vartheta$, referred to as smallest instability.

Assuming that the lifespan of most eddies is of a time scale of their own turn-over time (based on experimental evidence), the kinetic energy per unit mass is passed down to the smaller scales at a rate of:

$$\Pi \sim \frac{u^2}{l/u} = \frac{u^3}{l} \tag{2.6}$$

where $u$ and $l$ are the length and time scales of the more energetic eddies, as illustrated in Fig. 2.2.

For statistically steady conditions, this rate of energy transfer must balance the rate at which energy is

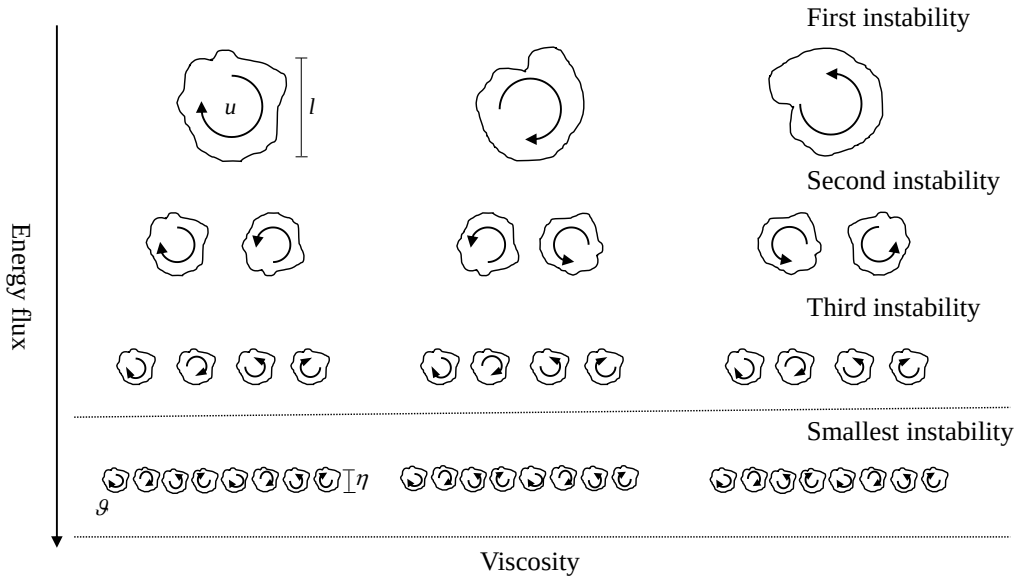


Figure 2.2 – Schematic representation of the energy cascade and turbulence scales. Adapted from Davidson (2004)

dissipated at the smallest scales (DAVIDSON, 2004). The dissipation rate is given by:

$$\varepsilon \sim \nu S_{ij} S_{ij} \tag{2.7}$$

where $S_{ij} = (1/2)[\nabla \mathbf{u} + (\nabla \mathbf{u})^{\mathrm{T}}]$ is the rate of strain tensor associated with the smallest scales. Performing a scale analysis it is seen that $S_{ij} \sim \vartheta/\eta$ and therefore Eq. 2.7 yields:

$$\varepsilon \sim \nu \frac{\vartheta^2}{\eta^2}. \tag{2.8}$$

Assuming an equilibrium state, combining Eq. 2.6 and 2.7 gives:

$$\frac{u^3}{l} \sim \nu \frac{\vartheta^2}{\eta^2} \tag{2.9}$$

An outcome of Kolmogorov's second hypothesis is that the smallest scales Reynolds number $Re_\eta = \vartheta\eta/\nu \sim 1$, which is consistent with the idea that energy is cascaded to smaller and smaller scales until dissipation is effective (POPE, 2000), and taking the largest scales $Re_l = ul/\nu$, it is possible to derive a few correlations to express the scales of turbulent flows. Combining the equations above results in, as an example, a relation between the largest and smallest scales as follows:

$$\eta \sim l Re_l^{-3/4}. \tag{2.10}$$

The scales $\eta$ and $\vartheta$ are called the Kolmogorov microscales (KOLMOGOROV, 1941). Using Eq. 2.10 it is possible to estimate the magnitude of time and dimensional limit scales contained in a turbulent flow. Taking a circular pipe, for example, where water flow is characterized by $Re_l \sim 10^5$ and assuming $l \sim d \sim 1$ cm, the smallest eddies would have the size of $\eta \sim 10^{-4}$ cm and a lifespan $\tau = \eta^2/\nu$ of only $10^{-2}$ s. This is the reason of such high computational effort behind DNS simulations and the obstacle that prevents the technique of being applied to higher $Re$.

## 2.3 Turbulence modelling

On the duty of trying to develop an universal theory to describe turbulent flows, scientists, engineers, physicists and mathematicians have struggled for centuries. Although the Navier-Stokes equations are known for a quite long time and are also capable of representing any Newtonian flow, the effect of the non-linear terms takes the possibility of finding a deterministic solution to an insane level of complexity. That complexity is based on the fact that, as any other non-linear phenomena, turbulent flows are extremely sensitive to initial conditions and the next result will always differ from the last. Even for computer calculations on which exactly the same initial conditions can be set, the simple presence of rounding errors will take the solution to a different end (DAVIDSON, 2004).

The way researchers found to overcome the intrinsic randomness of turbulence was to call upon statistical techniques. Although the instantaneous values for a local variable are not repeatable its time-average is (for a representative amount of time) (DAVIDSON, 2004). This means that, as long as one is not interested in the instantaneous flow field with its $n$-order fluctuations, the time-averaged solution is reproducible and perfectly fits most of engineering purposes.

It sounds perfect for the construction of an universal theory that comprises, at least, any turbulent mean flow. So let us start by time-averaging the Navier-Stokes equations based on the Reynolds decomposition. Reynolds proposed that a quantity may be expressed as the sum of a steady mean component and a time varying fluctuating component with zero mean value:

$$\phi(\mathbf{x},t) = \overline{\phi}(\mathbf{x}) + \phi'(\mathbf{x},t). \tag{2.11}$$

Substituting Eq. 2.11 in the Cartesian Navier-Stokes equations yields:

$$\rho\frac{\partial\overline{u}_i}{\partial t} + \rho\overline{u}_j\frac{\partial\overline{u}_i}{\partial x_j} = -\frac{\partial\overline{p}}{\partial x_i} + \frac{\partial}{\partial x_j}\left[\overline{\tau}_{ij} - \rho\overline{u_i'u_j'}\right] \tag{2.12}$$

where $\overline{u}_i$ is the time-averaged $i-th$ component of the velocity vector, $\overline{p}$ is the time-averaged pressure, $\overline{\tau}_{ij}$ the time-averaged viscous shear stress tensor and $-\rho\overline{u_i'u_j'}$ the Reynolds stresses originated from the time-averaging process. They are interpreted as additional stresses caused by momentum flux exchange of the fluctuating quantities with the mean flow (DAVIDSON, 2004).

Equation 2.12 is named the Reynolds-averaged Navier-Stokes equation. In this form, turbulent flows may now present one dimensionality and steadiness properties which is a characteristic of many advantages when speaking of CFD modelling. On the other hand, the time-averaged non-linear term produced nine new unknowns as shown below for an arbitrary orthogonal coordinate system.

$$\overline{u_i'u_j'} = \begin{bmatrix} \overline{u_1'u_1'} & \overline{u_1'u_2'} & \overline{u_1'u_3'} \\ \overline{u_2'u_1'} & \overline{u_2'u_2'} & \overline{u_2'u_3'} \\ \overline{u_3'u_1'} & \overline{u_3'u_2'} & \overline{u_3'u_3'} \end{bmatrix} \tag{2.13}$$

No matter how much algebra effort is put into deriving a new set of equations for these unknown quantities there will always be more unknowns than equations. This problem is known as the *Turbulence*

*Closure Problem*. Therefore, it is necessary to conceive the missing relations to pair equations and their unknowns and then solve them via some CFD technique.

This is the challenge of classical turbulence models based on time-averaged equations. The first attempt to overcome this situation probably dates back to Boussinesq's work in the 1870s. He proposed a shear-stress strain-rate relationship for time-averaged flows of one-dimensional nature of the form:

$$\overline{\tau}_{xy} + \tau^R_{xy} = \rho\left(\nu + \nu_t\right)\frac{\partial \overline{u}_x}{\partial y} \tag{2.14}$$

where he named $\nu_t$ as the *eddy viscosity* or *turbulent viscosity* (DAVIDSON, 2004). The idea behind Eq. 2.14 is that the role of turbulence is to bump the effective viscosity from $\nu$ to $\nu + \nu_t$, where $\nu_t$ is presumably greater than $\nu$. The concept generalization for three-dimensional flows is given as:

$$\tau^R_{ij} = -\rho\overline{u'_i u'_j} = \rho\nu_t\left[\frac{\partial \overline{u}_i}{\partial x_j} + \frac{\partial \overline{u}_j}{\partial x_i}\right] - \frac{\rho}{3}\overline{u'_k u'_k}\delta_{ij} \tag{2.15}$$

Inserting 2.15 in 2.12 and substituting the viscous stress for its Newtonian correlation gives

$$\rho\frac{D\overline{u}_i}{Dt} = -\frac{\partial \overline{p}}{\partial x_i} + \rho\frac{\partial}{\partial x_j}\left[\nu\left(\frac{\partial \overline{u}_i}{\partial x_j} + \frac{\partial \overline{u}_j}{\partial x_i}\right) + \nu_t\left(\frac{\partial \overline{u}_i}{\partial x_j} + \frac{\partial \overline{u}_j}{\partial x_i}\right) - \frac{1}{3}\overline{u'_k u'_k}\delta_{ij}\right] \tag{2.16}$$

which can be rearranged yielding:

$$\rho\frac{D\overline{u}_i}{Dt} = -\frac{\partial \overline{p}}{\partial x_i} + \rho\frac{\partial}{\partial x_j}\left[\left(\nu + \nu_t\right)\left(\frac{\partial \overline{u}_i}{\partial x_j} + \frac{\partial \overline{u}_j}{\partial x_i}\right) - \frac{1}{3}\overline{u'_k u'_k}\delta_{ij}\right] \tag{2.17}$$

The last term is known as the turbulence kinetic energy and it is defined as one half the trace of 2.13:

$$k = \frac{1}{2}\overline{u'_i u'_i} \tag{2.18}$$

It is coupled to the pressure term to become the modified mean pressure. Equation 2.17 is then rewritten to yield:

$$\rho\frac{D\overline{u}_i}{Dt} = -\frac{\partial\left(\overline{p} + \frac{2}{3}k\right)}{\partial x_i} + \rho\frac{\partial}{\partial x_j}\left[\left(\nu + \nu_t\right)\left(\frac{\partial \overline{u}_i}{\partial x_j} + \frac{\partial \overline{u}_j}{\partial x_i}\right)\right] \tag{2.19}$$

Although the fluctuating terms were eliminated based on the eddy viscosity hypothesis, there is still one unknown which must be determined in order to solve Eq. 2.19, that is, the eddy viscosity itself. If the turbulent viscosity hypothesis is accepted as an adequate approximation, all that remains is to determine an appropriate specification for it. In general, this can be done by multiplying a velocity $u^*(\mathbf{x}, t)$ by a length $\ell^*(\mathbf{x}, t)$ scale:

$$\nu_t = u^*\ell^* \tag{2.20}$$

In algebraic models like the *mixing length model*, $\ell^*$ is specified based on geometric characteristics of the flow. In two-equation models like the $k - \epsilon$ model, $u^*$ and $\ell^*$ are related to $k$ and $\epsilon$, for which modelled transport equations are derived and solved.

## 2.4 Large-Eddy simulation

The unsteady irregular motion that is associated with turbulent flows has an impact in momentum and heat transfer. The associated quantities such as temperature, concentration distribution, to stress out a few examples, are significantly influenced. Therefore, any successful computation of such phenomena must take the effect of turbulent motion into account in a proper manner (RODI et al., 2013).

As briefly mentioned before, the only way of accounting for the whole energy spectra is to perform a DNS. In the other extreme, RANS based models account for the turbulent effect in the mean flow through the action of the so called Reynolds Stresses. In this case, the whole spectrum of turbulent motion is modelled. The problem with DNS is the CPU time demand which leaves it out of the picture for engineering purposes. The problem with RANS is that the large energy-containing structures depend on the problem geometry, boundary conditions and the very nature of the flow, that is, wall-bounded or free-shear, rotating or non-rotating. The closuring constants for RANS models are calibrated empirically which creates a sort of link between one model and the problem it was calibrated for.

The idea of LES is that, since the small scales are not far from being isotropic (JIMÉNEZ, 2013), their role of mopping up whatever energy is cascaded to them is modelled whilst the large, energy-containing and boundary-dependent structures are resolved. By modelling the small scales, the computational cost is dramatically reduced but the turbulent motion effect is mostly accounted for.

To accomplish that, the resolved and modelled spectra must be somehow split apart. This task is done by filtering the governing equations with the aid of some adequate technique. Ideally, this separation or cut-off length takes place in a region that only energy transfer occurs, that is, no production or dissipation exists. In Fig. 2.3, an expected energy spectrum is represented for DNS and LES. The cut-off wave-number $k_{\mathrm{cut-off}}$ represents the separation between resolved and unresolved scales. As mentioned before, the $k_{\mathrm{cut-off}}$ is placed in a region called inertial subrange, where only energy transfer exists.

The three classical and most used filters for LES are the Gaussian filter, Fourier cut-off filter and box filter (POPE, 2000). Mathematically, the filtering process corresponds to the convolution of any flow quantity $f(\mathbf{r}, t)$ by the filter function $G$ in the form of the Eq. 2.21 (LESIEUR et al., 2005).

$$\overline{f}(\mathbf{r}, t) = \int_D G(\mathbf{r}, \mathbf{r}', \Delta) f(\mathbf{r}', t) dV' \tag{2.21}$$

In Eq. 2.21, $\overline{f}$ is the filtered parcel of $f$, $G$ is the filter function and $\Delta$ is the filter width. The filter function $G$ must satisfy the normalization function, that is

$$\int_D G(\mathbf{r}, \mathbf{r}', \Delta) dV' = 1 \tag{2.22}$$

The subgrid-scale field $f'$ is therefore the departure of the actual flow with respect to the filtered field:

$$f = \overline{f} + f' \tag{2.23}$$

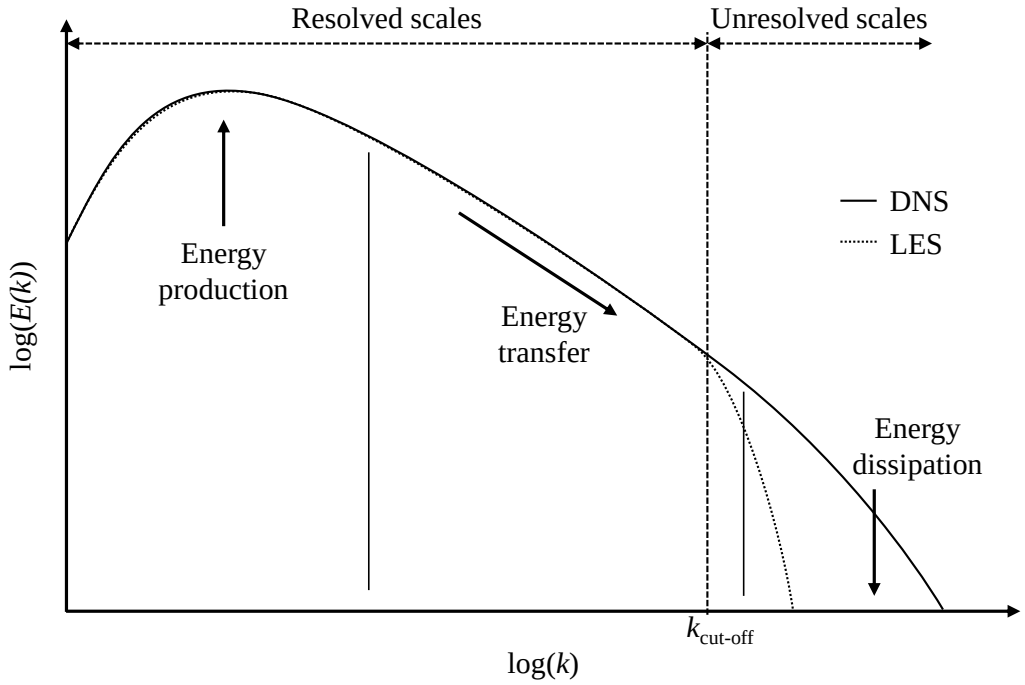


Figure 2.3 – Schematic representation of the energy spectrum for DNS and LES

The filtered field $\overline{f}$, which is three-dimensional and time-dependent, represents the large eddies motion (POPE, 2000).

The filtering operation may be performed in physical or spectral space and it can be done implicitly or explicitly. In explicit filtering, the filter function appears explicitly in the governing equations and the result is a continuous distribution of the filtered field. For implicit filtering, the grid size plays the role of the filter resulting in cell averaged values and a discontinuous distribution of the filtered field.

When deriving the filtered Navier-Stokes equations, as well as for the RANS equations, the non-linear term produces a set of unknowns which must be somehow accounted for in order to close the equations. These unknowns are named subgrid-scale stresses $\tau_{ij}^{\mathrm{SGS}}$ (Eq. 2.24) and represent the effect of the unresolved, small-scale turbulence on the resolved/filtered motion (RODI et al., 2013).

$$\tau_{ij}^{\mathrm{SGS}} = \overline{u_i u_j} - \overline{u_i}\,\overline{u_j} \tag{2.24}$$

There are two forms of accounting for $\tau_{ij}^{\mathrm{SGS}}$ effect: through explicit or implicit modelling. The former consists of deriving a model which must dissipate the correct amount of energy from the calculated large-scale flow and allow a realistic energy exchange for the resolved scales. The latter relies on the dissipative effect of the numerical scheme to mop up the energy descending from the large-scale motion.

In practice, the implicit modelling is the most used and the most famous models are based on the Boussinesq hypothesis for the eddy viscosity. For detailed information regarding filtering operations as well as SGS models, the reader can refer to relevant literature (POPE, 2000; LESIEUR et al., 2005). A discussion about the filter and SGS models used in this study is given in Chapter 4.

# 3 Literature Review

In this chapter, a brief but comprehensive review of turbulent flows in stationary ducts are presented in first place. Subsequently, relevant studies involving turbulent flows in the presence of rotation is provided. Lastly, the effect of curvature over the mean flow and turbulence-related quantities is also discussed.

## 3.1 Stationary channel and duct flow

Turbulent flows in ducts of varied cross-sections are the core of many industrial applications. Although the pressure-drop per unit length is the most desired information, in many situations, knowing the details of flow structure is indispensable for characterizing processes such as heat transfer or multiphase flows (DEAN, 1978).

Prior to the advent of computer simulations and elaborated experimental techniques, researchers were concerned with determining the onset of turbulent motion. The classical experiments of Osbourne Reynolds (REYNOLDS, 1883) show the importance of determining whether or not the flow is turbulent and its impact on the overall resistance. Later on, the results were extended to other geometries and their influence on the criterion itself as reported in the work of Davies and White (1928). In the latter work, the onset of turbulence was investigated for a square-sectioned duct and one important conclusion was drawn when the authors stated that for a certain value of $Re$ based on the hydraulic diameter, the turbulence created at the test-section simply died out as the fluid travelled along the duct.

In the 70's, the advances in computer power allowed a different scenario for the study of turbulent flows. Deardorff (1970) made a ground-breaking study when he first implemented a LES solution of a three-dimensional turbulent Poiseuille channel flow. The author provided a large amount of data regarding turbulent quantities for large $Re$, some of which could not be obtained experimentally. The results, obtained with a modest number of grid points and the Smagorinsky model for the subgrid-scale (SGS) stresses, were compared with the experiments of Laufer (1950) showing reasonable agreement in the regions away from the wall. In the near-wall region, the law of the wall was employed resulting in some discrepancies.

The improvement in experimental techniques were no less important to turbulent flow investigations. The behaviour of the fluctuating velocity components at the wall regions of a rectangular channel was experimentally investigated by Kreplin and Eckelmann (1979). The flow was taken to be fully developed and the Reynolds number based on the channel width and centre line velocity was kept constant at $Re = 7700$. Although the $Re$ is low, the measurements were done down to $y^+ = u_\tau y/\nu \approx 3$ ($u_\tau = \sqrt{\tau_w/\rho}$ is the friction velocity) in the streamwise and down to $y^+ \approx 1.5$ in the spanwise directions providing data to numerical validation. The authors shared the complexity of measuring that close to the wall and stated that in this region, the simple presence of the probe may alter flow structures.

Not surprisingly it took almost 40 years for this sort of investigation to reach industrial applications. In the recent work of Schultz and Flack (2013), the turbulent channel flow was experimentally investigated

for $1000 \leq Re_\tau = u_\tau \delta / \nu \leq 6000$ (where $u_\tau$ stands for shear velocity or friction velocity). Probing the velocity field with the aid of a Laser Doppler Velocimetry (LDV) equipment, the measurements were done down to $y^+ \approx 1$ for the lower $Re$ but the closest point for the upper limit of $Re$ lies in $y^+ \approx 30$. The experiments are very difficult to be performed for such high values of $Re_\tau$ since the smallest scales of the flow are smaller than the measuring equipment leaving numerical solutions as the only option to investigate the flow in detail.

The first numerical study that truly calculated the flow in the vicinity of the wall was the one of Moin et al. (1978). According to the authors, the grid resolution was not adequate to capture the flow structure in the viscous sublayer but provided some experimentally observed features. The rigorous calculation of the near-wall flow is required since most of the turbulent energy production occurs in this region. The introduction of artificial boundary conditions to model the flow generally comes with under/over predictions of turbulent quantities.

By increasing grid resolution, Moin and Kim (1982) performed a LES simulation of the turbulent flow through a channel at $Re_\tau = 640$. They obtained the statistical properties of the flow and its structure and turbulent quantities were analysed in a certain detail. The attention was directed to the near-wall region and its influence on the mean flow. The scale of flow structures in the wall region, however, were generally larger than in experimental observations. Therefore, Kim et al. (1987) extended the later study by performing a DNS solution for $Re_\tau = 180$. In this study, a great amount of reliable data is provided regarding turbulent quantities. The results are still used in the present days as a data base to verify numerical solutions.

The interest behind higher $Re$ studies, from academical and industrial perspectives, is that some wall-bounded turbulence-associated characteristics first manifest for $Re_\tau > 10^3$ (LEE; MOSER, 2015). However, it is not trivial to obtain reliable numerical solutions for such values of $Re$. The DNS study of Kim et al. (1987) was carried out with $2 \times 10^6$ grid points and the recent work of Lee and Moser (2015), for $Re_\tau = 5200$, with astonishing $242 \times 10^9$ grid points, requiring half an year of CPU time in the IBM-MIRA super computer (RODI, 2017).

The channel flow has been used as a very suitable tool in turbulence investigations since periodicity may be assumed in both the streamwise and spanwise directions reducing the demanded computer power considerably. When the spanwise direction is restricted by the presence of solid boundaries, the flow becomes even more complex due to the strong anisotropy near the walls and the corners. In the duct flow, interaction is happening with four enclosed walls instead of two as in the channel flow case. The simple presence of these additional walls, not only distorts the streamwise flow but also creates secondary motion near the corners as a result of turbulent stresses imbalance (MADABHUSHI; VANKA, 1991). The correct prediction of this type of secondary motion strongly depends on the correct prediction of turbulent stresses, which restricts the application of RANS-based models. The enhanced RSM model of Reif and Andersson (2002) was able to predict the secondary motion but with lower intensity when compared to the DNS solution of Huser and Biringen (1992). The former work reports the difficulty of turbulence models on dealing with second moment closures. The physics of the secondary motion itself was very well explored in the recent work of Pinelli et al. (2010). By varying $Re$ from quasi-laminar up to full turbulent values, the first appearance of secondary motion and how it scales with $Re$ was investigated

via DNS.

In general, the computing power advances throughout the years have allowed DNS studies to be performed for higher $Re$ as shown in the brief historical outline in Table 3.1.

Table 3.1 – Historical outline for turbulent channel flow

| Authors | Geometry | Method | $Re_\tau$ |
|---|---|---|---|
| Deardorff (1970) | Channel | LES | - |
| Moin et al. (1978) | Channel | LES | 640 |
| Moin and Kim (1982) | Channel | LES | 640 |
| Kim et al. (1987) | Channel | DNS | 180 |
| Moser et al. (1999) | Channel | DNS | 590 |
| Lee and Moser (2015) | Channel | DNS | 5200 |

As very well reported in the work of Jiménez (2013), the interest on increasing the $Re$ has been devoted to expand the knowledge generated over the years on the best hope of fully describing a multi-scale turbulent process. In particular, the study highlights the importance of wall-bounded turbulent flows from scientific and industrial perspectives and condensates the state of the art on near-wall calculations.

These accomplishments in numerical simulations alongside with experimental advances, as reported in the work of Schultz and Flack (2013), may one day be used to improve turbulence models to deliver reliable solutions in feasible computing time.

## 3.2 Rotating channel flow

The flow subjected to span-wise rotation was vastly studied in the last decades. From theoretical and experimental (HART, 1971; JOHNSTON et al., 1972; NANBU, 1971; MOORE, 1973) to numerical investigations (GRUNDESTAM et al., 2008; KUBACKI et al., 2016), these studies bring up the influence of effects that emerge due to rotation over heat transfer and hydrodynamics. One of the most striking features is that of the competing effect of stabilized and destabilized regions coexisting as a result of the Coriolis force. The effect of rotation in this case, is to laminarize the flow field. In the present work, however, the interest is directed to the situation in which rotation occurs in parallel to the mean flow direction.

This particular case of the flow being parallel to the rotation axis was also vastly studied. The work of Mori and Nakayama (1967) showed from a theoretical perspective that as in flows subjected to span-wise rotation, parallel-mode rotation induces remarkable distortions in velocity and temperature profiles. The presence of secondary flow increases the heat transfer coefficient and hydrodynamic resistance. The effect of Coriolis force was found to decrease the pressure gradient responsible for driving the secondary motion, lessening flow resistance and heat transfer rate.

The influence of the rotation speed alongside with entry conditions was then investigated in a later experimental work by Johnson and Morris (1984). By testing a wide range of $Re$ on a circular cross-sectioned pipe, the authors showed that as long as the flow is fully developed, the rotation speed is

insignificant in the flow pattern increasing resistance in less than 10%. On the other hand, for non developed flow regions, the increase in rotation speed augment hydraulic resistance severely, reaching 30-40%. A similar study was conducted by Levy et al. (1986) where a rectangular cross-sectioned duct uniformly heated was experimentally investigated. The flow regime remained laminar and the results presented pressure drop increasings of about 30-35% corroborating the numerical previsions of Levy and Kannan (1985). Further numerical investigations over the same problem providing detailed flow structure and heat transfer mechanisms for a extended set of experimental conditions were performed by Soong and Yan (1999).

Sleiti and Kapat (2006) conducted a more robust numerical approach aiming to understand the physics under the simultaneous action of Coriolis and centrifugal/buoyancy forces by implementing a Reynolds-Stress model of a square duct rotating in parallel-mode. The most important conclusion regards the discrepancy between heat transfer rates for each duct surface as a consequence of stress imbalance. Increasings in pressure loss due to rotational effects were also noted.

Chiu et al. (2007) included the effect of radiation and implemented a vorticity-velocity method to solve the problem of a square duct rotating in parallel mode. The flow was investigated in laminar regime and the increase in rotation was found to increase the friction factor.

Fasquelle et al. (2014) implemented a numerical simulation of heated circular and elliptical cross-sectioned pipes rotating in parallel mode. Using an ANSYS Fluent code, turbulent quantities were calculated with the standard $k - \omega$ model. The aim of the study was to enhance heat transfer on a real size coolant duct used in electric generators.The focus was directed to heat transfer enhancements obtained for different geometric configurations. The numerical procedure was verified against empirical correlations for the average Nusselt number and showed good agreement. However, there is no evidence that the local quantities are well predicted.

From the literature review, it is clear that great effort has been devoted to understand the physics of rotation induced phenomena and its influence on the flow characteristics. For spanwise rotation, there are recent solution data available ((FANG et al., 2016), (HSIEH et al., 2016), (DAI et al., 2015)). In this field, the latest outcomes resemble those of straight stationary channels, that is, the advances in computer power have allowed the limits to be pushed forward. On the other hand, parallel-mode rotation effects still lack in-depth studies. Despite the fact that laminar flows are easier to implement, they are very rare in industrial applications and for the turbulent cases, as far as the author is aware, there is no detailed information in the literature regarding the flow characteristics.

## 3.3 Curvature-influenced flows

Curvature plays an important role in fluid mechanics studies. In industrial applications it is almost impossible to build pipelines without having any bend and coiled tubes are very useful geometries in heat exchangers. In aerodynamics and rotary machines, curvature effects are always present.

One of first investigations of such phenomena dates back to the early $20^{th}$ century, where the effects of curvature on flow resistance of water in circular cross-sectioned pipes were experimentally studied (EUSTICE, 1910). The results were compared with those obtained for straight pipes and an increase in

flow resistance was noted in the presence of curvature. In other words, the pressure gradient necessary to maintain the same flow rate is increased.

The presence of curvature, besides altering flow resistance, also change the transition criterion proposed by Reynolds (1894). In Eustice (1911) experiments, a statement is done regarding that there is no critical velocity for coiled pipes. Rather, the transition occurs in a gradual manner and starts in velocities lower than that expected for straight pipes. His conclusions were sustained by the theoretical analysis of Dean (1928a) for a curved channel. He proposed that the reason for the transition to occur prior to that expected for a straight pipe is that the curvature contributes for the flow to be unstable for small disturbances whilst it is stable in the case of straight channels. He shows that a type of small disturbance which could not persist in a straight channel is possible in a curved channel. It is likely to explain the absence of sudden transition as noticed by Eustice (1910).

Dean (1927), derived a theoretical solution for the flow of an incompressible fluid along a circular cross-sectioned pipe. He found some agreement between theory and the experiments of Eustice (1911) but failed to show the pressure gradient relation with the rate of flow. In this work, the Dean number concept was introduced, aggregating centripetal forces to the Reynolds number to determine the onset of turbulence on flows with curvature effects. In his next paper, Dean (1928b) extended the analysis and showed that the difference of pressure is necessary to sustain the secondary flow which occurs as a result of the centrifugal tendency of the fluid. This secondary flow, which is already taking place before the critical velocity is reached, is the responsible for the absence of sudden transition.

In the next year, White (1929) pointed out a few inconsistencies in Eustice (1911) experiments and came up with a completely different point of view about the onset of turbulence along pipe bends. By conducting a set of experiments, he argued that there is indeed a marked critical velocity for the transition to happen and that this velocity is higher than that expected for a straight pipe. The author stated that the effect of the curvature is to drive the flow to a streamline regime rather than anticipate the transition to turbulence. The problem in Eustice (1911) was that there were no measures taken to control the entry conditions of the flow in the test section. White (1929) showed that the initial conditions play a huge role in the results and also validates Dean's theory for streamline motion in curved pipes.

Intrigued with the discrepancy between White (1929) and Eustice (1911) results, Taylor (1929) decided to repeat some of Eustice (1911) experiments taking into account the provisions in the entry region as commented by White (1929). The results showed that steadiness persisted up to velocities where one would find turbulent motion in a straight pipe, corroborating the results found by White (1929).

The pure effect of curvature came to play in the 30's, when Wattendorf (1935) was dealing with the fully developed turbulent flow within a curved channel of rectangular cross section. In order to isolate the curvature effect, the author assembled an experimental apparatus consisting of a curved rectangular channel with large aspect ratio to prevent secondary flow to happen. In this study, it was found just a slight increase in flow resistance due to curvature effects when compared with the straight channel leading to the conclusion that the substantial losses are linked to the secondary motion. On the other hand, the velocity and pressure profiles were highly distorted along the channel bend with the velocity peak being shifted towards the inner wall.

Extending Wattendorf (1935) experiments, Eskinazi and Yeh (1956) took the analysis to the en-

ergy spectra approach and their results showed that turbulence production is more intense at the outer walls which leaves this region with the greatest turbulence intensity. An extensive review regarding the subsequent studies of flow in curved pipes was performed by Berger et al. (1983) and Ito (1987).

From a numerical perspective, Patankar et al. (1975) first employed the $k - \epsilon$ model to turbulent flows in curved pipes. The study covered both entry and fully developed flows and results displayed reasonable agreement with experimental data. The wall function approach was implemented to treat near-wall regions and ease computational effort which contributed to the discrepancies in the results.

Moser and Moin (1987) solved the Navier-Stokes equations directly for concentric cylinders. The flow was considered to be turbulent and fully developed. The effect of curvature was then investigated by comparing the flow field and turbulent quantities. The so called Taylor-Görtler vortices were responsible for a significant impact on the turbulence statistics and may not be neglected. The turbulent kinetic-energy terms as many other quantities are insensitive to the presence of curvature so that standard k-based turbulence models are not likely to produce significant curvature effects.

Kao (1987) investigated the effect of torsion on the fully developed laminar flow in a helix. He faced the problem with theoretical and numerical approaches. For the theoretical analysis, the Poiseuille solution was perturbed to derive a series solution for the helical geometry. The numerical solution was obtained by implementing a finite difference procedure together with the QUICK scheme for the advective terms. The main conclusions were directed to the influence of torsion on the secondary flow pattern and flow resistance along the pipe. The increase in torsion distort the secondary flow, which was symmetric in first place, but its effect on flow resistance when compared to the curvature's was considered to be always small for whole set of cases.

Di Piazza and Ciofalo (2010) assessed classical turbulence models when treating heat transfer and fluid flow along helically coiled pipes. They compared numerical predictions with both experimental and DNS data. The $k - \epsilon$ model led to underpredictions of the friction factor and Nusselt number. The reason was taken to be in spite of the weak wall treatment employed in this model which fails to capture boundary layer detachment and impingement in the inner and outer walls respectively. Both SST-$k - \omega$ and RSM-$\omega$ showed great agreement with reference data even for low Reynolds flows, below transition to fully turbulent, but failed to represent correctly.

Kang and Yang (2016) recently studied the effects of pipe curvature on heat transfer characteristics by performing LES of fully developed turbulent curved-pipe flow with constant wall heat flux. The sub-grid stresses were modelled with the Smagorinsky eddy-viscosity model and the procedure was validated against DNS and experimental results. The curved pipe was represented by a toroid and flow was driven by a mean pressure gradient. They found that the mean friction factor and mean Nusselt number increase with increasing curvature which indicates heat transfer enhancement at the expense of increased friction.

Curvature has also an interest effect in shear-flow turbulence (BRADSHAW, 1973). A slight curvature already changes the mean flow and turbulent quantities by means of a new mode of instability which manifests in the form of Taylor-Görtler vortices (HUNT; JOUBERT, 1979). A very suitable tool to investigate curvature related phenomena in turbulent shear-flows is the Taylor-Coutte problem. As reported in the work of Dong (2007), since the experiments of Taylor himself, an overwhelming amount of studies have been published in this area. Most of the knowledge regarding turbulence mechanisms

and characteristic structures, however, comes from experimental studies while numerical approaches are mainly concentrated in the laminar regime. Dong (2007) tackled the problem through a DNS solution varying the rotational $Re$ from 1000 to 8000. In this range, he compared the laminar with fully turbulent flow and investigated the dynamical and statistical properties of such flow. The results corroborated experimental and theoretical predictions.

More recently, Ostilla-Mónico et al. (2016) extended the $Re$ range up to $Re_\tau = 4000$. The study was conducted through a DNS solution of a small gap system with the inner cylinder rotating at a constant speed. This configuration is known as a Rayleigh-unstable system. Taylor rolls were found to form in the bulk contributing to the transport of angular momentum via Reynolds stresses. Even for curvatures of 1%, Taylor rolls redistribute angular momentum altering the nature of the law of the wall. The introduction of a weak axial flow acts convecting Taylor rolls but do not change its topology.

If an axial Poiseuille flow is superimposed to the Taylor-Couette flow, the problem becomes even more complex. The axial flow has a stabilizing effect, delaying the transition to turbulent state or bringing the flow back to a laminar state. The capabilities of a RSM when dealing with such flow configuration were evaluated by Poncet et al. (2011) obtaining very favourable results when compared to experimental predictions. They extended the $Re$ for real operating conditions by performing a LES in order to investigate the influence of coherent structures over heat transfer (PONCET et al., 2014). The subgrid stresses were modelled with the WALE (Wall Adapting Local Eddy-vicosity) proposed by Nicoud and Ducros (1999). Some test cases were also run with the Dynamic Smagorinsky model providing very similar results but with an increase in computational effort of 12%.

Curvature is very well known to cause great change in flow dynamics and has motivated many studies to tackle the problem for increasingly high $Re$. For shear-dominated flows, curvature plays a significant role on redistributing momentum and modifying the way they are transported. Taylor-Couette flows are suitable to investigate such phenomena since periodicity is easily achieved in both azimuthal and axial directions reducing computational cost. RANS based models have shown, in general, not to be suitable due to the effect that curvature exerts on Reynolds stresses leaving LES and DNS as preferred methods to deal with the problem.

## 3.4 Specific objectives

In this chapter, a brief review regarding relevant studies to the present problem was presented. It is clear that the advances in computer hardware and experimental techniques lead studies to complex levels on the hope of digging deeper into the physics of turbulence. The establishment of high-fidelity numerical techniques such as DNS allowed the acquirement of data quantities that cannot be obtained experimentally. On the other hand, due to the substantial computer power that is required, it is still restricted to simple geometries and low-Reynolds flows, thus limiting its applicability to complex engineering problems in the foreseeable future. Simplistic approaches like RANS-based models, however, are very sensible to the geometry and intrinsic assumptions make them even more sensible to problems where streamline curvature and rotation are present. A viable solution to deal with it is to stay in between both approaches by means of LES. In LES, both streamline curvature and rotation are accounted for and as the smallest

isotropic scales are modelled, the required computer power falls down to something around 1% of that required for DNS (RODI, 2017).

The literature review has shown that a high volume of information regarding turbulent flows in straight channels, ducts, Taylor-Couette and Taylor-Couette-Poiseuille systems is available. For geometries accounting for system rotation, there is a disparity for spanwise and parallel-mode rotations. For systems rotating in parallel to the mean flow axis, studies are mainly concentrated in average heat transfer measurements in laminar regime revealing a blank in the understanding of this rotation mode influence in turbulence related quantities.

The present study, therefore, has the main goal to investigate the role of parallel-mode rotation in turbulent quantities and its competitive effect with geometry, curvature and shear-induced secondary motion. To accomplish that, the flow within an annular-sector duct rotating about a parallel axis with a stationary outer wall will be investigated. The flow dynamics as a function of the axial and rotational $Re$ as well as the geometric parameters will be obtained from a large-eddy simulation with the aid of a commercial CFD code.

# 4 Problem Formulation

In this chapter the problem mathematics will be derived. The governing equations accounting for rotation will be introduced with the adopted hypotheses. Geometry, boundary conditions, filtered equations and SGS models will be also provided.

## 4.1 Geometric configuration

The problem geometry and the coordinate system are shown in Fig. 4.1. The coordinate system rotates around the $z$-axis with an angular speed $\omega$. The domain is represented by an annular-sector duct. The outer wall counter-rotates with a constant speed $-\omega$, which implies it is stationary with respect to the rotating reference frame (RRF). The radial gap and apex angle are denoted by $\delta$ and $\alpha$, respectively. The ratio of the inner to the outer radius is given by $\eta$. The channel height $H$ is chosen in such a way that periodicity may be imposed in the streamwise direction. For this assumption to be true, there must be no relation between the flow structures crossing both domain interfaces. This condition is guaranteed by two-point correlation measurements which will be discussed in the next section. The domain walls are considered to be perfectly smooth and impermeable.

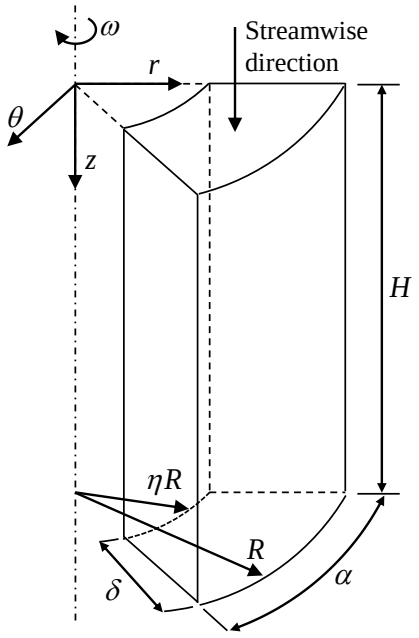


Figure 4.1 – Geometric configuration of the problem and adopted coordinate system

## 4.2 Boundary conditions

For the domain walls, no-slip condition is assumed, that is, the fluid velocity at the walls is that of the wall itself:

$$\begin{aligned} \mathbf{u}(r = \eta R, \theta, z, t) &= 0 \\ \mathbf{u}(r = R, \theta, z, t) &= -\omega R \\ \mathbf{u}(r, \theta = 0, z, t) &= 0 \\ \mathbf{u}(r, \theta = \alpha, z, t) &= 0 \end{aligned} \tag{4.1}$$

where $\mathbf{u}$ is the velocity vector defined on the rotating frame of reference. The initial condition to the set of equations is obtained from a steady RANS solution with a superimposed synthetic turbulent field. The Synthetic-Eddy Method (SEM) produces a divergence free velocity field with specified intensity and length scale (JARRIN et al., 2006). Therefore:

$$\mathbf{u}(r, \theta, z, t = 0) = \mathbf{u}^{\text{RANS+SEM}} \tag{4.2}$$

For the periodic boundaries, the assumption of periodicity implies that the velocity components repeat in space in the form:

$$\mathbf{u}(r, \theta, z) = \mathbf{u}(r, \theta, z + H). \tag{4.3}$$

As mentioned before, the choice of the adequate value for $H$ must be done very carefully. If $H$ is somewhat smaller than the size of the largest eddies contained in the flow, they will be artificially confined within the domain, which will lead to unphysical results (RODI et al., 2013). A safe value for $H$ may be extracted from two-point correlation coefficients given by:

$$R_{uu}(d) = \frac{\langle u'(z)u'(z+d)\rangle}{\langle u'^2\rangle} \tag{4.4}$$

where $d$ is the streamwise separation and $u$ is one of the velocity field components with its fluctuating counterpart represented by $u'$. The operator $\langle\ \rangle$ represents that the quantity was averaged in time. The idea behind Eq. 4.4 is that the value of $R_{uu}$ must go to zero when the velocities for two separated points are uncorrelated. That is to say that they do not belong to the same eddy structure. If this condition is respected, periodicity does not interfere in the results (RODI et al., 2013).

## 4.3 Governing equations

The governing equations are derived in physical space for a rotating frame of reference accounting for centrifugal and Coriolis forces. The flow is considered to be isothermal. The fluid is taken to be Newtonian and incompressible. Gravity is neglected.

For a rotating reference frame (RRF), the total derivative of the velocity field in an inertial frame is expressed as (DAVIDSON, 2013):

$$\frac{D\mathbf{u}}{Dt} = \left(\frac{D\mathbf{u}}{Dt}\right)_{\text{RRF}} + \boldsymbol{\Omega} \times (\boldsymbol{\Omega} \times \mathbf{r}) + 2\boldsymbol{\Omega} \times \mathbf{u}_{\text{RRF}} \tag{4.5}$$

where $\mathbf{u}$ is the velocity vector, $()_{\text{RRF}}$ denotes that the quantity is evaluated with respect to the rotating frame of reference, $\boldsymbol{\Omega}$ is the frame angular velocity vector and $\mathbf{r}$ is the position with respect to the RRF. Therefore, the continuity and momentum equations assume the form:

$$\nabla \cdot \mathbf{u}_{\text{RRF}} = 0 \tag{4.6}$$

$$\frac{\partial \mathbf{u}_{\text{RRF}}}{\partial t} + (\mathbf{u}_{\text{RRF}} \cdot \nabla)\, \mathbf{u}_{\text{RRF}} + 2\boldsymbol{\Omega} \times \mathbf{u}_{\text{RRF}} + \boldsymbol{\Omega} \times (\boldsymbol{\Omega} \times \mathbf{r}) = -\frac{1}{\rho}\nabla p + \frac{1}{\rho}\nabla \mathbf{T}_{\text{RRF}} \tag{4.7}$$

In Eq. 4.7, the terms $2\boldsymbol{\Omega} \times \mathbf{u}_{\text{RRF}}$ and $\boldsymbol{\Omega} \times (\boldsymbol{\Omega} \times \mathbf{r})$ represent the Coriolis and centrifugal forces per unit mass, respectively. In the right-hand side, $p$ stands for pressure and $\mathbf{T}$ is the viscous stress tensor. From this point, the subscripts RRF will be dropped out.

## 4.4 Filtered governing equations

As mentioned in Section 2.3, in order to separate the resolved from unresolved length scales, the governing equations must be subjected to a low-pass filter.

The general filtering operation is defined as the convolution of any flow quantity by the filter function $G$ as shown in Eq. 2.21 resulting in the decomposition represented in Eq. 2.23. Although very similar to the Reynolds decomposition as in Eq. 2.11, a very important difference lies in the fact that as $\overline{f}$ is a random field, in general, the filtered residual is not zero, that is (POPE, 2000):

$$\overline{f'(\mathbf{r}, t)} \neq 0. \tag{4.8}$$

Assuming the filter width $\Delta$ as being constant, it is shown that the space and time derivatives commute with the filter operator (POPE, 2000):

$$\overline{\frac{\partial f}{\partial x_i}} = \frac{\partial \overline{f}}{\partial x_i}. \tag{4.9}$$

Since the the centrifugal force is a conservative type of force it may be aggregated to the pressure term to form the modified pressure. Filtering Eqs. 4.6 and 4.7 yields the filtered continuity and momentum equations, respectively:

$$\nabla \cdot \overline{\mathbf{u}} = 0 \tag{4.10}$$

$$\frac{\partial \overline{\mathbf{u}}}{\partial t} + (\overline{\mathbf{u}} \cdot \nabla)\, \overline{\mathbf{u}} + 2\boldsymbol{\Omega} \times \overline{\mathbf{u}} = -\frac{1}{\rho}\nabla \overline{P} + \frac{1}{\rho}\nabla \left(\overline{\mathbf{T}} - \mathbf{T}^{\text{SGS}}\right) \tag{4.11}$$

In Eq. 4.11, the term $\overline{\mathbf{T}}$ is the resolved viscous stress tensor and $\mathbf{T}^{\mathrm{SGS}}$ is the subgrid-stress tensor. Analogously to the RANS equations, its appearance is due to the non-linear convective term. For convenience, assuming the suffix notation after Versteeg and Malalasekera (2007), $\mathbf{T}^{\mathrm{SGS}}$ is defined as:

$$\mathbf{T}^{\mathrm{SGS}} = \tau_{ij}^{\mathrm{SGS}} = \overline{u_i\, u_j} - \overline{u}_i \overline{u}_j \tag{4.12}$$

The term $\overline{u}_i \overline{u}_j$ above is the product of resolved-scale quantities and can be directly calculated. The closure problem for LES arises from the remaining part of $\mathbf{T}^{\mathrm{SGS}}$. Recalling the Reynolds decomposition and assuming that a quantity $\phi(\mathbf{r}, t)$ may be decomposed into a resolved parcel $\overline{\phi}(\mathbf{r}, t)$ and an unresolved parcel $\phi'(\mathbf{r}, t)$, the term $\overline{u_i\, u_j}$ can be rewritten in the form:

$$\begin{aligned}
\overline{u_i\, u_j} &= \overline{(\overline{u}_i + u_i')(\overline{u}_j + u_j')} = \overline{\overline{u_i}\,\overline{u_j}} + \overline{\overline{u_i} u_j'} + \overline{u_i'\,\overline{u_j}} + \overline{u_i' u_j'} \\
&= \overline{u_i}\,\overline{u_j} + \left(\overline{\overline{u_i}\,\overline{u_j}} - \overline{u_i}\,\overline{u_j}\right) + \left(\overline{\overline{u_i} u_j'} + \overline{u_i'\,\overline{u_j}}\right) + \overline{u_i' u_j'} \\
&= \overline{u_i}\,\overline{u_j} + L_{ij} + C_{ij} + R_{ij}
\end{aligned} \tag{4.13}$$

The terms $L_{ij}$, $C_{ij}$ and $R_{ij}$ are called Leonard stress tensor, cross-stress tensor and Reynolds subgrid-scale stress tensor, respectively (LESIEUR et al., 2005). Although the Leonard stresses are defined in terms of filtered quantities, the second averaging does not reproduces the result of a first one, i.e. $\overline{\overline{\phi}} \neq \overline{\phi}$ and consequently, $\overline{\overline{u_i}\,\overline{u_j}} \neq \overline{u_i}\,\overline{u_j}$ as it would be equal for time-averaging. Leonard (1974) proposed that, as $\overline{u}_i$ is fairly smooth, the unknown can be approximated by a Taylor series expansion:

$$\overline{\overline{u_i}\,\overline{u_j}} - \overline{u_i}\,\overline{u_j} = \frac{\Delta^2}{24} \overline{u_i}\,\overline{u_j} \tag{4.14}$$

Since the terms in the right hand side of Eq. 4.14 are scale-resolved quantities, they can be explicitly calculated. Ferziger (1977) proposed a similar approach to obtain the cross-stress term:

$$\overline{\overline{u}_i\, u_j'} + \overline{u_i'\,\overline{u}_j} = \frac{\Delta^2}{24} \left(\overline{u}_i \nabla^2 \overline{u}_j + \overline{u}_j \nabla^2 \overline{u}_i\right) \tag{4.15}$$

The remaining term, the SGS Reynolds stress tensor, has to be modelled. The most common approach is to invoke the Boussinesq hypothesis, in which the local SGS Reynolds stresses are taken to be proportional to the local rate of strain of the resolved flow:

$$R_{ij} = -2\mu_{\mathrm{SGS}} \overline{S}_{ij} + \frac{1}{3} R_{ij} \delta_{ij} \tag{4.16}$$

In most finite volume method applications (including STAR-CCM+), however, the whole stress-tensor $\mathbf{T}^{\mathrm{SGS}}$ is modelled as a single entity by means of a SGS turbulence model and therefore (VERSTEEG; MALALASEKERA, 2007):

$$\tau_{ij}^{\mathrm{SGS}} = -2\mu_{\mathrm{SGS}} \overline{S}_{ij} + \frac{1}{3} \delta_{ij} \tau_{ii}^{\mathrm{SGS}} \tag{4.17}$$

Generally, as represented in Eq. 4.17, the SGS tensor is split into an isotropic and an anisotropic part (LESIEUR et al., 2005). The isotropic part contains the sum of the SGS normal stresses which is twice the subgrid turbulent kinetic energy $k^{SGS}$, acting like a pressure. Just like in the RANS formulation, this term is added to the filtered pressure term which now becomes:

$$\overline{P} = \overline{p} + \frac{1}{3}\tau_{ii}^{\mathrm{SGS}} - \frac{1}{2}(\omega r)^2 \tag{4.18}$$

where the last term represents the centrifugal force.

Although all quantities are now in terms of the resolved scales, $\mu_{\mathrm{SGS}}$ remains unknown. Its determination procedure is what characterizes the SGS models based on the Boussinesq hypothesis. The models implemented in the present work are detailed in the sequence.

## 4.5 Subgrid-scale models

As mentioned before, the effect of the unresolved small-scale motion on the resolved filtered field is represented by the SGS stresses that arise from the filtered non-linear convective term in the governing equations. This effect may be accounted for with the aid of an explicit SGS model or through the dissipative nature of the numerical scheme used in the solution, read ILES (Implicit Large-Eddy Simulation).

The most popular models for general purpose simulations are the explicit SGS models, most of which are eddy viscosity models (RODI et al., 2013). It is noteworthy that the eddy viscosity is not a fluid property and the Boussinesq hypothesis validity is never completely verified (SCHMITT, 2007).

### 4.5.1 The Smagorinsky model

The Smagorisnky model (SMG) is the most popular SGS model. The kinematic SGS eddy viscosity $\nu_{\mathrm{SGS}} = \mu_{\mathrm{SGS}}/\rho$ is estimated algebraically through a dimensional analysis. This approach is analogous to the Prandtl's mixing length model described in Eq. 2.20. Since the viscosity has dimensions $m^2/s$, it can be obtaind from the product of a length by a velocity scale. The obvious choice for the length scale is to involve the filter width $\Delta$. As in Prandtl's mixing length model, the velocity scale is derived from the product of the length scale by the resolved strain rate resulting in:

$$\nu_{\mathrm{SGS}} = (C_S\Delta)^2 \left|\overline{S}_{ij}\right| \tag{4.19}$$

where $C_S$ is the Smagorinsky constant, determined from theoretical considerations or empirically.

The model adjustable parameter $C_S$ assumes different values for different flows. One major drawback is that, for wall-bounded flows, the eddy viscosity must vanish in the vicinity of the walls which is not allowed by Eq. 4.19. Another characteristic is that as $\nu_{\mathrm{SGS}}$ is zero only if the velocity gradients are also zero and as consequence, the model fails to capture laminar-to-turbulent transitions since for laminar flows $\nu_{\mathrm{SGS}} = 0$. Another one is that as $\nu_{\mathrm{SGS}}$ is always positive, the model does not allow energy transfer from small to large scales or backscattering. Lastly, in complex three-dimensional flows, the optimum

value of $C_S$ varies locally within the flow field. For flows accounting for rotation or stratification effects, $C_S$ also need to be modified (RODI et al., 2013).

The problem of a non-zero viscosity near the walls may be solved with auxiliary dumping functions. In his pioneer work, Deardorff (1970) assumed $C_S = 0.1$. The constant for homogeneous isotropic turbulent flows was derived analytically by Lilly (1992 apud LILLY, 1966, p. 1) as being $C_S = 0.18$ in the inertial subrange. This value was found cause much dissipation and a value of $C_S = 0.065$ was used in the work of Moin and Kim (1982). The differences in the value os $C_S$ gave indication that the constant requires a case-by-case tuning. More sophisticated approaches on the determination of $C_S$ were developed through the years allowing $C_S$ to be calculated rather than estimated.

### 4.5.2 Dynamic Smagorinsky-Lilly model

Germano et al. (1991) utilized the same concept of Smagorinsky but allowed the model coefficient to vary in space and time. He suggested the use of a second filter, a test filter that would get information of the smallest resolved scales to determine the model coefficient. The test filter has a width $\tilde{\Delta}$ which is larger than $\Delta$, usually twice the size of it. The same model is then applied to calculate $\tau_{ij}^{SGS}$ and $T_{ij}^{\mathrm{SGS}}$, where the latter is the SGS-test-filter stress tensor.

The SGS-test-filter stresses $T_{ij}^{\mathrm{SGS}}$ are obtained from double-filtering the governing equations. Filtering Eqs. 4.10 and 4.11 but now with respect to $\tilde{\Delta}$ one gets:

$$T_{ij}^{\mathrm{SGS}} = \tilde{\tau}^{\mathrm{SGS}} + \widetilde{\overline{u}_i\,\overline{u}_j} - \widetilde{\overline{u}}_i\,\widetilde{\overline{u}}_j \tag{4.20}$$

where the tilde ($\tilde{}$) represents the test filter operation. Considering the resolvable part of 4.20 as

$$L_{ij} = \widetilde{\overline{u}_i\,\overline{u}_j} - \widetilde{\overline{u}}_i\,\widetilde{\overline{u}}_j \tag{4.21}$$

and replacing it into Eq. 4.20 yields Germano's identity (GERMANO et al., 1991):

$$T_{ij}^{\mathrm{SGS}} = \widetilde{\tau}_{ij}^{SGS} + L_{ij} \tag{4.22}$$

Equation 4.22 can be rewritten to give the so called test-window stresses:

$$L_{ij} = T_{ij}^{\mathrm{SGS}} - \widetilde{\tau}_{ij}^{SGS} \tag{4.23}$$

The elements of $L_{ij}$ are resolved components of the stress tensor associated with scales of motion between the test scale and the grid scale (LILLY, 1992). A schematic representation of $L_{ij}$ is given in Fig. 4.2 where the cut-off wave number for the filter $\pi\Delta$ and test-filer $\pi\widetilde{\Delta}$ defines the resolved stresses $L_{ij}$.

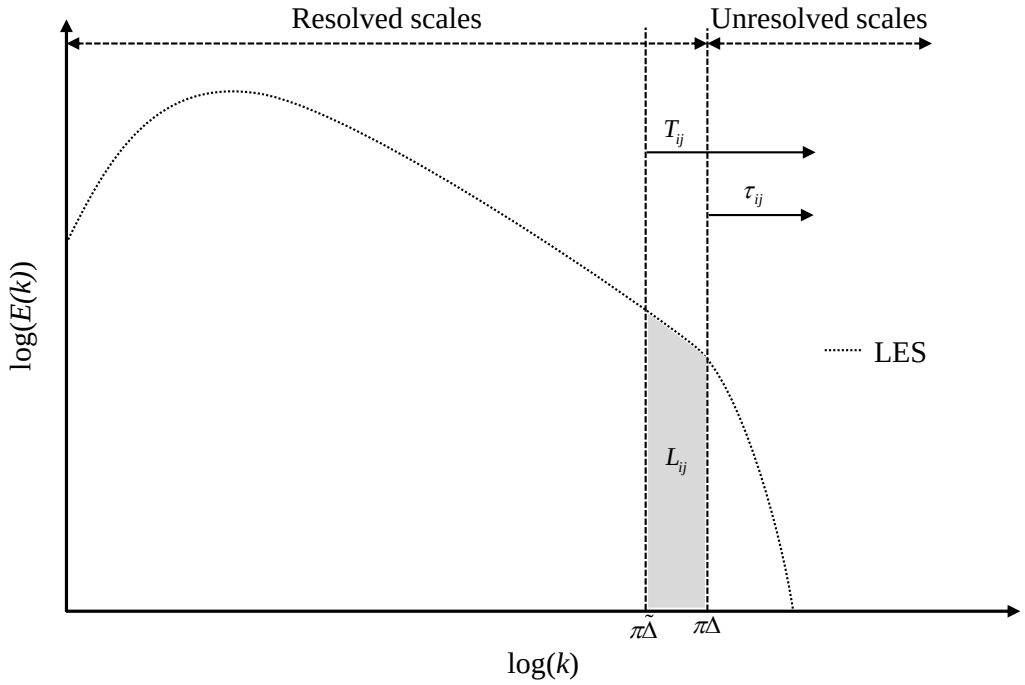


Figure 4.2 – Typical energy spectrum of LES that employs Dynamical procedure SGS model. Adapted from: Rodi et al. (2013)

The right hand side of Eq. 4.21 is explicitly evaluated and compared locally with Eq. 4.23 where every quantities in the right hand side can be modelled with the Smagorinsky approach, i.e.:

$$\begin{aligned} \tau_{ij}^{SGS} - \frac{1}{3}\delta_{ij}\tau_{ii}^{SGS} &= -2C\Delta^2 \left|\overline{S}\right| \overline{S}_{ij} \\ T_{ij}^{SGS} - \frac{1}{3}\delta_{ij}T_{ii}^{SGS} &= -2\widetilde{C}\widetilde{\Delta}^2 \left|\widetilde{\overline{S}}\right| \widetilde{\overline{S}}_{ij} \end{aligned} \tag{4.24}$$

By inserting Eq. 4.24 into 4.23 must result in the unknown coefficient $C_D$ if $C\left(x,y,z,t\right) \approx \widetilde{C}\left(x,y,z,t\right)$. Therefore, Eq. 4.23 becomes:

$$L_{ij} - \frac{1}{3}\delta_{ij}L_{ii} = -2C_D\left(\Delta^2\left|\overline{S}\right|\overline{S}_{ij} - \widetilde{\Delta}^2\left|\widetilde{\overline{S}}\right|\widetilde{\overline{S}}_{ij}\right) \tag{4.25}$$

The only unknown in Eq. 4.25 is $C_D$ which in principle solves the problem of the SMG model, that is, finding the correct value for $C_D$ and applying it to Eq. 4.19. However, Germano et al. (1991) noticed that the quantity within the brackets may become zero resulting in the indetermination or ill-conditioning of $C_D$. To overcome this problem, the authors suggested $C_D = C_D(y,t)$ only. As they tested the model for the turbulent flow within parallel plane plates, they allowed $C_D$ to vary only in the wall-normal direction averaging both sides of Eq. 4.25 over a $xz$-plane in order to obtain an averaged value for $C_D$.

A year later, Lilly (1992) proposed a modification to Germano's closure since it would get complicated to take averages in complex geometries or where no homogeneous direction exists. He realized that since Eq. 4.25 represents five independent equations, no value of $C_D$ can be chosen to make it correct. So instead of obtaining it directly from Eq. 4.25, he defined a quantity $Q$ as the square error associated with

it, i.e.:

$$Q = \left( L_{ij} - \frac{1}{3}\delta_{ij} L_{kk} - 2C_D M_{ij} \right)^2 \tag{4.26}$$

where $M_{ij}$ denotes the quantity between brackets in Eq. 4.25. By minimizing $Q$ with a least squares approach upon setting $\partial Q / \partial C_D = 0$, $C_D$ may then be evaluated from:

$$C_D = \frac{1}{2} \left( \frac{L_{ij} M_{ij}}{M_{ij}^2} \right) \tag{4.27}$$

The numerator in Eq. 4.27 can be null, positive or negative, allowing laminarization or even backscattering. This version of the Smagorinsky model is expected to be a powerful tool on predicting the near-wall region low Reynolds flows without any dumping function needed. On the other hand, when evaluated for individual grid points, $C_D$ can still assume large enough values to become computationally unstable. One way out is to perform some averaging process to avoid excessively large values. Another way out, the usual choice of commercial CFD codes, is to simply truncate isolated values of $C_D$.

## 4.6 Chapter summary

In first place, it is noteworthy that the schematic representation presented in Fig. 2.3 may only be verified if the filter width $\Delta$ is constant throughout the entire domain. The value for $\Delta$, however, depends on the grid resolution which is coarsened away from the walls in order to reduce computational effort. The cut-off wave number, therefore, is instead a range of cut-off wave-numbers.

The set of governing equations to be solved in this study is formed primarily by the filtered continuity and momentum equations:

$$\nabla \cdot \overline{\mathbf{u}} = 0 \tag{4.28}$$

$$\frac{\partial \overline{\mathbf{u}}}{\partial t} + \left( \overline{\mathbf{u}} \cdot \nabla \right) \overline{\mathbf{u}} + 2\boldsymbol{\Omega} \times \overline{\mathbf{u}} = -\frac{1}{\rho} \nabla \overline{P} + \nabla \left( \overline{\mathbf{T}} - \mathbf{T}^{\mathrm{SGS}} \right) \tag{4.29}$$

The SGS stress tensor $\mathbf{T}^{\mathrm{SGS}}$ is modelled by the Dynamic Smagorinsky-Lilly model. Assuming the suffix notation (VERSTEEG; MALALASEKERA, 2007):

$$\tau_{ij}^{\mathrm{SGS}} = -2\mu_{\mathrm{SGS}} \overline{S}_{ij} + \frac{1}{3}\delta_{ij} \tau_{ii}^{\mathrm{SGS}} \tag{4.30}$$

The isotropic part of $\tau_{ij}^{\mathrm{SGS}}$ and the centrifugal force are combined to the filtered pressure to form the modified pressure (see Eq. 4.18). The SGS viscosity $\mu_{\mathrm{SGS}}$ is obtained from the dynamic model proposed Germano et al. (1991) with the modifications proposed by Lilly (1992). The set of equations above is solved numerically using the finite volume method. The details concerning the numerical procedure are presented in the next chapter.

# 5 Numerical Implementation

The numerical calculation of the filtered continuity and momentum equations was conducted by using the commercial CFD code, Siemens STAR-CCM+ R.12.04. The code is based on the Finite Volume Method (FVM) and allows efficient parallelisation.

This chapter presents the numerical formulation as implemented in the software. The information was retrieved from the software's user manual and the reference will be suppressed otherwise strictly necessary.

## 5.1 Discretization of the transport equations

In the FVM, the domain of interest is subdivided into smaller volumes called cells, over which the conservation equations are integrated in space and time. Figure 5.1 illustrates two adjacent cells, denoted by $0$ and $1$.

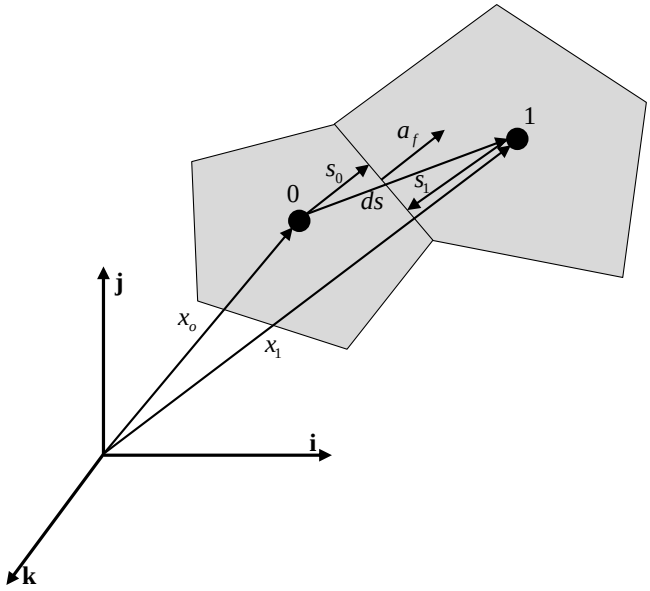


Figure 5.1 – Polyhedral computational cells. Adapted from STAR-CCM+, 2017

In Fig. 5.1, $\mathbf{x}$ is the cell centroid position vector, $\mathbf{s}$ is the distance vector from the cell centroid to the cell face, $\mathbf{ds}$ is the distance vector between both cell centroids such that $\mathbf{ds} = \mathbf{x}_1 - \mathbf{x}_0$ and $\mathbf{a}_f$ is the face area vector.

Considering the transport equation, Eq. 5.1, for a generic scalar quantity $\phi$, integrating over the cell

volume $V$ and applying Gauss's divergence theorem yields:

$$\underbrace{\frac{d}{dt}\int_V \rho\phi dV}_{\text{I-Transient Term}} + \underbrace{\int_A \rho\mathbf{u}\phi \cdot d\mathbf{a}}_{\text{II-Convective Flux}} = \underbrace{\int_A \Gamma\nabla\phi d\mathbf{a}}_{\text{III-Diffusive Flux}} + \underbrace{\int_V S_\phi dV}_{\text{IV-Source Term}} \tag{5.1}$$

where $A$ is the cell surface area, $d\mathbf{a}$ the surface area vector, $\Gamma$ the diffusion coefficient and $S_\phi$ a source term.

Equation 5.1 contains four different terms:

I - Transient Term: time rate of change of the scalar $\phi$ within the cell.

II - Convective Flux: net rate of decrease of $\phi$ across the cell boundaries due to convection.

III - Diffusive Flux: net rate of decrease of $\phi$ across the cell boundaries due to diffusion.

IV - Source Term: generation/destruction of $\phi$ within the cell.

In each one of them, the volume and surface integrals must be converted into discrete sums. For the former, the integral is approximated by the product of the mean value of the quantity at the cell centre and the cell volume:

$$\int_V \rho\phi dV \approx \rho\phi V \tag{5.2}$$

$$\int_V S_\phi dV \approx S_{\phi_0} V \tag{5.3}$$

For the latter, STAR-CCM+ employs the second-order midpoint rule and the integral is evaluated as the product of the value at the cell face centre and the cell face area:

$$\int_A \mathbf{J}^\phi d\mathbf{a} \approx \sum_f \mathbf{J}_f^\phi \mathbf{a}_f \tag{5.4}$$

where $\mathbf{J}^\phi$ is either the convective or diffusive flux of $\phi$, $\mathbf{a}_f$ is the surface area vector of the cell face $f$ and $\sum_f$ the sum over every cell face. Applying the integral approximations gives:

$$\frac{d}{dt}(\rho\phi V) + \sum_f [\rho\phi(\mathbf{v}\cdot\mathbf{a})]_f = \sum_f (\Gamma\nabla\phi\cdot\mathbf{a})_f + (S_\phi V)_0 \tag{5.5}$$

By definition, the value for $\phi$ is known at the cell centre and it is constant along the cell volume. However, in order to evaluate the convective and diffusive fluxes of $\phi$ through the cell faces, it must be interpolated between the cell and face centres. The choice of the interpolation scheme have profound effect in the stability and accuracy of the numerical solution.

### 5.1.1 Diffusive terms

Recalling the diffusive flux in Eq. 5.1,

$$D_f = (\Gamma\nabla\phi\cdot\mathbf{a})_f \tag{5.6}$$

both the diffusion coefficient $\Gamma$ and the gradient of the transported quantity $\nabla\phi$ must be evaluated at the cell faces. The value for $\Gamma_f$ is obtained by averaging the cell values in a harmonic fashion. To obtain an accurate second-order expression for an interior face gradient that implicitly involves the cell values $\phi_0$ and $\phi_1$, the following decomposition is used:

$$\nabla\phi_f = (\phi_1 - \phi_0)\,\vec{\alpha} + \overline{\nabla\phi} - \left(\overline{\nabla\phi}\cdot\mathbf{ds}\right)\vec{\alpha} \tag{5.7}$$

where:

$$\vec{\alpha} = \frac{\mathbf{a}}{\mathbf{a}\cdot\mathbf{ds}} \tag{5.8}$$

$$\overline{\nabla\phi} = \frac{\nabla\phi_0 + \nabla\phi_1}{2} \tag{5.9}$$

The diffusion flux at an interior face can then be written as:

$$D_f = \Gamma_f \nabla\phi_f \cdot \mathbf{a} = \Gamma_f \left[(\phi_1 - \phi_0)\,\vec{\alpha}\cdot\mathbf{a} + \overline{\nabla\phi}\cdot\mathbf{a} - \left(\overline{\nabla\phi}\cdot\mathbf{ds}\right)\vec{\alpha}\cdot\mathbf{a}\right] \tag{5.10}$$

The cell gradients $\nabla\phi_0$ and $\nabla\phi_1$ are evaluated, by default, from the Hybrid Gauss-Least Squares (HGLSQ) method. In the HGLSQ, computing gradients involves two major steps as described below.

**1. Computing the (unlimited) reconstruction gradients**

The term unlimited means that the gradients do not prohibit the reconstructed field variables on the cell faces from exceeding the minimum and maximum values of the neighbouring cells.

The unlimited reconstruction gradients in cell-0, denoted by the superscript $()^u$, are computed using the following hybrid formula:

$$(\nabla\phi)_r^u = \sum_f (\phi_n - \phi_0)\, w_f^0 \tag{5.11}$$

with:

$$w_f^0 = \beta w_f^{\text{lsq}} + (1-\beta)\, w_f^{\text{G}} \tag{5.12}$$

$$w_f^{\text{lsq}} = \left[\sum_f \frac{\mathbf{ds}\otimes\mathbf{ds}}{\mathbf{ds}^2}\right]^{-1} \frac{\mathbf{ds}}{\mathbf{ds}^2} \tag{5.13}$$

$$\mathbf{ds} = \mathbf{x}_n - \mathbf{x}_0 \tag{5.14}$$

$$w_f^{\text{G}} = \frac{A_f}{V_0 - V_n} \tag{5.15}$$

where $\beta$ is the method blending factor. It is used to weight between the two methods in calculating the gradient. The following conditions apply to the blending factor $\beta$:

$$\beta = \begin{cases} 1 & \text{Pure LSQ} \\ 0 & \text{Pure Gauss} \\ 0 < \beta < 1 & \text{Blended} \end{cases} \tag{5.16}$$

Choosing $\beta$ from 0 to 1 equates to:

$$\nabla\phi = (\beta)\,\mathbf{LSQ} + (1-\beta)\,\mathbf{Gauss} \tag{5.17}$$

The value for $\beta$ is not an user input. Instead, it is locally calculated as the minimum of the following:

$\beta = 1$ if the least-squares tensor eigenvalues ratio of the cell is larger than the specified minimum value, which is set to 0.1 by default.

$\beta = 1$ if the tangent of the skewness angle $\theta$ is smaller than the Normalized Flat Cells Curvature Factor (set to 1.0 by default) times the aspect ratio of the cell. It is less than 1, with a rapid decrease to zero otherwise. The skewness angle $\theta$ is the angle between the face area vector $\mathbf{a}$ and the vector connecting the cell centroids $\mathbf{ds}$. If $\theta = 0$, the mesh is perfectly orthogonal.

$\beta = 1$ if the skewness angle is smaller than the maximum safe (Positive) skewness angle (set to 75 degrees by deafult). $\beta = 0$ if the skewness angle is larger than the minimum unsafe (Positive) skewness angle (88 degrees by default). Otherwise, $0 < \beta < 1$ with a linear variation.

$\beta = 0$ if it is a Chevron-cell and $\beta = 1$ otherwise (Chevron-Cell Criterion). Chevron cells are pairs of thin slender cells which meet at a common face at an angle such that the line joining the cell centres does not pass through the common face.

For the grids in the present study, since the cells are mostly orthogonal and when they are not, the skewness angle does not exceed a few degrees, the value for $\beta$ is always unity so that the pure Least Squares method is used at all times.

**2. Limiting the reconstruction gradients**

The limited reconstruction gradients are used to determine scalar values at the cell faces. These scalar values are used in computing flux integrals.

The problem with simply reconstructing face values from the unlimited reconstruction gradients is that the reconstructed face values can fall outside the range of cell values found in neighboring cells (connected through faces). For this reason, STAR-CCM+ finds the minimum and maximum bounds of the neighboring cell values and uses these to limit the reconstruction gradients.

The face value $(\phi_{f,0})$ reconstructed from the cell-0 value at any face centroid is given by:

$$\phi_{f,0} = \phi_0 + \mathbf{s}_0 \cdot (\nabla\phi)_{r,0} \tag{5.18}$$

where $\mathbf{s}_0 = \mathbf{x}_f - \mathbf{x}_0$. $\mathbf{x}_f$ and $\mathbf{x}_0$ are the face and cell centroids, respectively, and $\nabla\phi_{r,0}$ is the reconstructed face value.

For each cell-0, a limited reconstruction gradient is required, such that the reconstructed face value does not exceed the maximum and minimum of the neighbouring cell centroid values, including the value in cell-0. A scale factor $\alpha$ is defined that expresses the ratio of the limited and unlimited values, that is:

$$(\nabla\phi)_{r,0} = \alpha\,(\nabla\phi)^u_{r,0} \tag{5.19}$$

For each cell, the quantities are defined:

$$\phi_0^{\max} = \max\left(\phi_0, \phi_{\text{neighbours}}\right) \tag{5.20}$$

$$\phi_0^{\min} = \min\left(\phi_0, \phi_{\text{neighbours}}\right) \tag{5.21}$$

where $\phi_{\text{neighbours}}$ represents the cell value in each neighbour that has a common face with cell-0. These quantities can also be defined as:

$$\Delta_{\max} = \phi_0^{\max} - \phi_0 \tag{5.22}$$

$$\Delta_{\min} = \phi_0^{\min} - \phi_0 \tag{5.23}$$

where $\Delta$ must not be mistaken with the filter width of the LES formulation. For each face of the cell-0, $\Delta_f$ is defined as:

$$\Delta_f = \phi_{f,0} - \phi_0 = \mathbf{s}_0 \cdot (\nabla\phi)^u_{r,0} \tag{5.24}$$

Now, defining:

$$r_f = \begin{cases} \frac{\Delta_f}{\Delta_{\max}} & \text{for } \Delta_f > 0 \\ \frac{\Delta_f}{\Delta_{\min}} & \text{for } \Delta_f \leq 0 \end{cases} \tag{5.25}$$

In the present computations, the Venkatakrishnan limiter was used (VENKATAKRISHNAN, 1993). For the face it gives:

$$\alpha_f = \frac{2r_f + 1}{r_f\,(2r_f + 1) + 1} \tag{5.26}$$

### 5.1.2 Convective terms

The discretized convective term in Eq. 5.5 can be rearranged as follows:

$$(\phi\rho\mathbf{u}\cdot\mathbf{a})_f = (\dot{m}\phi)_f = \dot{m}_f\phi_f \tag{5.27}$$

where $\dot{m}_f$ is the mass flow rate at the face. Equation 5.27 requires the value of $\phi$ evaluated at the face. Since the value for $\phi$ is known at the cell centre, it must be somehow interpolated to the cell face. The manner in which this process is done has profound effect on the stability and accuracy of numerical scheme.

**The Normalized Variable Diagram**

The normalized variable diagram (NVD) is useful for analyzing boundedness properties of convective discretization schemes. Figure 5.2a shows three cells in the vicinity of a cell face $f$, across which the velocity $\mathbf{v}_f$ is known. The nodal variable values are labelled $\alpha_D$, $\alpha_C$ and $\alpha_U$, representing the downwind, central, and upwind positions relative to each other. The convection boundedness criterion is shown in Fig. 5.2b.

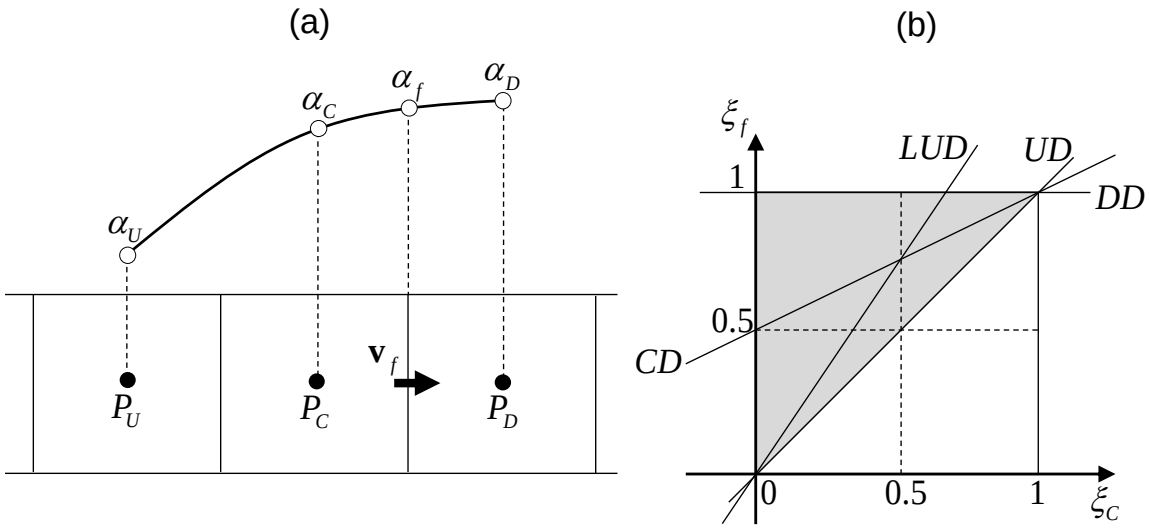


Figure 5.2 – Normalized Variable Diagram. Adapted from STAR-CCM+, 2017

The normalized variable $\xi(\mathbf{r},t)$ in the vicinity of the face is defined as:

$$\xi(\mathbf{r},t) = \frac{\alpha(\mathbf{r},t) - \alpha_U}{\alpha_D - \alpha_U} \tag{5.28}$$

The normalized face value:

$$\xi_f = \frac{\alpha_f - \alpha_U}{\alpha_D - \alpha_U} \tag{5.29}$$

calculated by any differencing scheme that uses only nodal value of $\alpha$ at points $U$, $C$ and $D$, can be written in the form:

$$\xi_f = \xi_f(\xi_C) \tag{5.30}$$

where:

$$\xi_C = \frac{\alpha_C - \alpha_U}{\alpha_D - \alpha_U} \tag{5.31}$$

To avoid non-physical oscillations in the solution, $\alpha_C$ (and consequently $\alpha_f$) has to be locally bounded between $\alpha_U$ and $\alpha_D$, meaning:

$$\alpha_U \leq \alpha_C \leq \alpha_D \tag{5.32}$$

or

$$\alpha_D \leq \alpha_C \leq \alpha_U \tag{5.33}$$

depending on the orientation of the velocity field. If this criterion is satisfied at every point in the domain, the entire solution is free of non-physical oscillations. The boundedness criterion for convection differencing schemes can be presented in the NVD diagram, showing $\xi_f$ as a function of $\xi_C$, as the shaded region in Fig. 5.2b (including the line $\xi_f = \xi_C$). It can also be expressed through the following conditions:

For $0 \leq \xi_C \leq 1$ the bounded region lies above the line $\xi_f = \xi_C$ and below $\xi_f = 1$.

For $\xi_C < 0$ and $\xi_C > 1$, $\xi_f$ is equal to $\xi_C$.

NVD is concerned with convective transport alone. If sources or sinks are present, the conditions that are given in Eq. 5.32 and Eq. 5.33 can be violated. The importance of the boundedness criterion is especially clear in the case of variables which have physical bounds.

**Central-Differencing**

The central-differencing scheme (CDS) approximates the cell face centre value by linear interpolation between the two nearest neighbouring cell centre values. The convective flux is computed as (PATANKAR, 1980):

$$(\dot{m}\phi)_f = \dot{m}_f \left[ f\phi_0 + (1-f)\,\phi_1 \right] \tag{5.34}$$

where the linear interpolation factor $f$ is related to the mesh stretching. For a uniform mesh, $f$ has a value of 0.5 so that Eq. 5.34 may be rewritten as:

$$(\dot{m}\phi)_f = \dot{m}_f \frac{\phi_0 + \phi_1}{2} \tag{5.35}$$

Central-differencing is formally second-order accurate. However it is prone to dispersive error and is beset with stability problems for most steady-state situations. The dispersive errors make it problematic for discretizing positive-definite quantities (such as temperature or turbulent kinetic energy) where overshoots cannot be tolerated. A significant advantage of central-differencing over second-order upwind is that, when used to discretize velocity it preserves turbulent kinetic energy. Therefore, it is a useful scheme in large eddy simulation (LES), where upwind schemes cause turbulent kinetic energy to decay unnaturally fast.

**Bounded Central-Differencing**

For a bounded central-differencing scheme, the convective flux is computed as (DARWISH; MOUKALLED, 1994; LEONARD, 1991):

$$(\dot{m}\phi)_f = \begin{cases} \dot{m}\phi_{\text{FOU}} & \text{for } \xi < 0 \text{ or } \xi > 1 \\ \dot{m}\left(\sigma\phi_{\text{CD}} + (1-\sigma)\,\phi_{\text{SOU}}\right) & \text{for } 0 \leq \xi \leq 1 \end{cases} \tag{5.36}$$

where FOU stands for the cell-face centre value obtained through first-order upwind interpolation, SOU for second-order upwind interpolation and CD for central-differencing interpolation.

A smooth and monotone function of $\xi$ is:

$$\sigma = \sigma\left(\xi\right) \tag{5.37}$$

which satisfies $\sigma(0) = 0$ and $\sigma(\xi) = 1$ for $\xi_{\text{ubf}} \leq \xi$. $\xi_{\text{ubf}}$ is called the upwind blending factor whose value ensures a proper balance between the accuracy and robustness of the scheme. Thus, smaller values of $\xi_{\text{ubf}}$ provide more accuracy, while larger values increase the robustness of the scheme.

To maintain boundedness, the bounded central-differencing scheme turns into a first-order upwind scheme when the convection boundedness criterion is not satisfied, for example when $\xi < 0$ or $\xi > 1$. The central-differencing scheme on the contrary, which is formally a second-order accurate scheme, does not do that. Thus, the bounded central-differencing scheme can be more dissipative than the central-differencing scheme, especially on coarser meshes.

**Hybrid MUSCL 3rd-Order/Central-Differencing**

The scheme is valid for both steady and unsteady simulations, and has one model parameter $\sigma$, which is used to control the numerical dissipation in the scheme. As with the bounded central-differencing scheme, this scheme uses a Normalized-Variable Diagram (NVD) value to ensure the boundedness of the scheme by switching to FOU in regions of non-smooth flows.

When smooth local flow conditions are detected, the scheme is constructed as a blend between a MUSCL 3rd-order upwind and a 3rd-order central-differencing reconstruction scheme. The convective flux is computed as:

$$(\dot{m}\phi)_f = \begin{cases} \dot{m}\phi_{\text{FOU}} & \text{for } \xi < 0 \text{ or } \xi > 1 \\ \dot{m}\left(\sigma\phi_{\text{MUSCL3}} + (1-\sigma)\,\phi_{\text{CD3}}\right) & \text{for } 0 \leq \xi \leq 1 \end{cases} \tag{5.38}$$

The blending factor $\sigma$ is user-controlled and must be decided based on the physical problem or model. Overall, the method causes less dissipation compared with the BCD scheme. At the same time, it is robust (due to its boundedness) and capable of simulating steady and unsteady flows from incompressible to high-speed compressible regimes.

### 5.1.3 Temporal discretization

To obtain the solution for a time-dependent problem, the time itself must also be subdivided into time-steps. In STAR-CCM+, by default for LES problems, the discretization of the transient term must be fully implicit. Although it has the advantage for being unconditionally stable allowing larger time-steps, the physical link between space and time in LES avoids such time-steps of being chosen. The robustness of the method is obfuscated by the need for internal iterations between time-steps, increasing the total time of the computation.

The Euler implicit scheme, a first-order temporal scheme, solves the transient term by approximating the solution based on the current field, that is (PATANKAR, 1980):

$$\frac{\partial}{\partial t}\left(\rho\phi V\right)_0 = \frac{\left(\rho\phi V\right)_0^{n+1} - \left(\rho\phi V\right)_0^{n}}{\Delta t} \tag{5.39}$$

where $n+1$ represents the current time-step and $n$ the previous one. The dependence on the current field imposes the necessity for an iterative process.

Equation 5.39 may also be discretized with second-order accuracy becoming:

$$\frac{\partial}{\partial t}\left(\rho\phi V\right)_0 = \frac{\left(\alpha^2-1\right)\left[\left(\rho\phi V\right)_0^{n+1} - \left(\rho\phi V\right)_0^{n}\right] + \left[\left(\rho\phi V\right)_0^{n-1} - \left(\rho\phi V\right)_0^{n}\right]}{\alpha\left(\alpha-1\right)\Delta t^{n+1}} \tag{5.40}$$

with:

$$\alpha = 1 + \frac{\Delta t^{n+1}}{\Delta t^{n}} \tag{5.41}$$

$$\Delta t^{n+1} = t^{n+1} - t^{n} \tag{5.42}$$

$$\Delta t^{n} = t^{n} - t^{n-1} \tag{5.43}$$

The second-order scheme requires the solution at the current time-step $n+1$ as well as the solution at the previous two time-steps $n$ and $n-1$.

## 5.2 Solver algorithm

The solution procedure starts by discretizing the momentum and continuity equations in a similar way to the generic scalar transport equation shown in the last section. By setting $\phi$ and $S_\phi$ accordingly one gets:

$$\frac{\partial}{\partial t}\left(\rho\mathbf{u}V\right)_0 + \sum_f \left[\rho\mathbf{u}\mathbf{u}\cdot\mathbf{a}\right]_f = -\sum_f \left(p\mathbf{I}\cdot\mathbf{a}\right)_f + \sum_f \mathbf{T}\cdot\mathbf{a} \tag{5.44}$$

where $\mathbf{v}$ is the velocity vector, $\mathbf{I}$ is the unity tensor and $\mathbf{T}$ is the viscous stress tensor.

In order to solve a fluid flow problem, one needs to find a velocity field that satisfies the continuity and momentum equations simultaneously. The problem is that the main momentum source is pressure, for which there is no transport equation. If the fluid is compressible, the continuity equation may be used to obtain the density and the pressure may be then obtained from an equation of state. For incompressible fluids, the link between density and pressure is broken by definition. In this case, the coupling between pressure and velocity is constrained by the continuity equation, that is, if the pressure field is correct, the velocity field must be divergence-free (VERSTEEG; MALALASEKERA, 2007).

In STAR-CCM+, this problem is approached by a guess-and-correct procedure. The SIMPLE algorithm, which means Semi-Implicit Method for Pressure-Linked Equations, is based on guessing a pressure field to obtain the corresponding velocity field. The details of the method can be found in relevant CFD literature.

In Eq. 5.44, the convective and diffusive fluxes are discretized as described in the last section. The discretization of the pressure gradient requires special attention. Pressure appears as pressure gradient in the momentum equations. In order to compute the pressure gradient term, the pressure must be evaluated at each face.

$$p_f = \frac{\overline{a}_0 p_{f0} + \overline{a}_1 p_{f1}}{\overline{a}_0 + \overline{a}_1} \tag{5.45}$$

where $\overline{a}_0$ and $\overline{a}_1$ are the average of the momentum coefficients for all components of momentum for cells 0 and 1, respectively. $p_{f0}$ and $p_{f1}$ are interpolated from cell values and reconstruction gradients according to Eq. 5.18.

At boundaries, the cell 1 contribution comes from a fictitious "ghost cell" in which the velocity has been reflected about the boundary face. Therefore Eq. 5.45 becomes:

$$p_f = p_{f0} \tag{5.46}$$

The algebraic system of equations if solved iteratively using the AMG method (Algebraic Multigrid).

## 5.3 LES formulation

The filtering operation is perfomed implicity by the finite-volume discretization itself. A filtered quantity is then defined as:

$$\overline{f}(\mathbf{r}, t) = \frac{1}{V} \int_V G(\mathbf{r}, \mathbf{r}') f(\mathbf{r}', t) dV \tag{5.47}$$

where $V$ is the volume of a computational cell. The adopted filter function $G$ is the top-hat or box-filter

where:

$$G\left(\mathbf{r},\mathbf{r}'\right)=\begin{cases}\dfrac{1}{V}, & \mathbf{r}'\in V\\ 0, & \text{otherwise}\end{cases} \tag{5.48}$$

The filter width $\Delta$ takes full advantage of the grid resolution. It is taken to be the cubic root of the cell volume $V$ determining the scales that will be filtered out such that:

$$\Delta^2=C_s^2V^{2/3} \tag{5.49}$$

The model constant $C_s$ is computed from:

$$C_s^2=\frac{\langle L_{ij}M_{ij}\rangle}{\langle M_{ij}M_{ij}\rangle} \tag{5.50}$$

where the brackets $\langle\ \rangle$ represent the averaging process over homogeneous directions as proposed by Lilly (1992). In STAR-CCM+, taking averages is optional and deactivated by default since most of industrial flows do not possess a homogeneous direction on which averages may be taken. $L_{ij}$ and $M_{ij}$ are defined as:

$$L_{ij}=\tilde{u}_i\hat{\tilde{u}}_j-\hat{\tilde{u}}_i\hat{\tilde{u}}_j \tag{5.51}$$

$$M_{ij}=2\Delta^2\left(\left|\tilde{S}\right|\hat{\tilde{S}}_{ij}-\left(\frac{\hat{\Delta}}{\Delta}\right)^2\left|\hat{\tilde{S}}\right|\hat{\tilde{S}}_{ij}\right) \tag{5.52}$$

where $\hat{\Delta}/\Delta$ is the test-to-grid filter ratio. Germano et al. (1991) made a battery of tests founding the optimal value to this ratio as being 2. Any test-filter quantity is evaluated as:

$$\hat{\tilde{\phi}}=\frac{1}{\sum\limits_{n=0}^{N}V_n}\sum_{n=1}^{N}\tilde{\phi}_nV_n \tag{5.53}$$

with $n$ representing the cell number. The current cell is represented by $n=0$ and its neighbours all the way from $n=1$ up to $n=N$.

The calculation of the turbulent viscosity in the Dynamic Smagorinsky model is then obtained from:

$$\nu_t=\Delta^2\tilde{S}=C_s^2V^{2/3}\tilde{S} \tag{5.54}$$

where the constant $C_s^2$ is clipped to lie between $0<C_s^2<10^6$ for stability purposes. By doing that, no backscatter is allowed.

## 5.4 Boundary conditions formulation

For the solid boundaries, no-slip condition is applied. The physical implication is that the relative fluid velocity tangential to the wall is set to zero. The velocity of the boundary $f$ computed as:

$$\mathbf{u}_f = \mathbf{u}_{\text{spec}}^{\text{lab}} - \left(\mathbf{u}_{\text{spec}}^{\text{lab}} \cdot \mathbf{a} - G_f\right) \frac{\mathbf{a}}{a^2} \tag{5.55}$$

where $\mathbf{a}$ is the face area vector and $\mathbf{u}_{\text{spec}}^{\text{lab}}$ is the velocity in the laboratory frame (the default inertial Cartesian coordinate system). $G_f = \mathbf{u}_g \cdot \mathbf{a}_f$ is the grid flux, where $\mathbf{u}_g$ is the grid velocity and $\mathbf{a}_f$ the face area. The velocity $\mathbf{u}_{\text{spec}}^{\text{lab}}$ is calculated as:

$$\mathbf{u}_{\text{spec}}^{\text{lab}} = \mathbf{u}_{\text{spec}}^{\text{mesh}} + \mathbf{u}_{\text{mesh}}^{\text{ref}} + \mathbf{u}_{\text{ref}}^{\text{lab}} \tag{5.56}$$

where $\mathbf{u}_{\text{spec}}^{\text{mesh}}$ is the specified velocity, measured relative to the mesh, $\mathbf{u}_{\text{mesh}}^{\text{ref}}$ is the velocity of the mesh relative to the cylindrical reference frame and $\mathbf{u}_{\text{ref}}^{\text{lab}}$ is the velocity of the reference frame relative to the laboratory frame.

The convective fluxes at the boundaries are then obtained by replacing $\phi_f$, in Eq. 5.27, by the boundary values $\phi_b$. The diffusive fluxes are obtained by replacing $\phi_1$ by the boundary value $\phi_b$ and $\overline{\nabla\phi}$ by $\nabla\phi_0$ in Eq. 5.10.

For the periodic interfaces, as mentioned in section 4.2, the velocity components are transported between interfaces (PATANKAR et al., 1977):

$$\mathbf{u}(r, \theta, z) = \mathbf{u}(r, \theta, z + H). \tag{5.57}$$

The pressure, however, cannot obey the same condition since in this scenario there would be no mass flow across the duct. The pressure drop, on the other hand, is periodic, that is:

$$\Delta p = p(r, \theta, z + H) - p(r, \theta, z) = p(r, \theta, z + 2H) - p(r, \theta, z + H). \tag{5.58}$$

Therefore, Patankar et al. (1977) defined the pressure field based on two components:

$$p(r, \theta, z) = -\beta z + P(r, \theta, z) \tag{5.59}$$

where $\beta$ is a constant related to the global mass flow and $P(r, \theta, z)$ is related to the detailed local motions. The expression for $\beta$ is such that:

$$\beta = \frac{p(r, \theta, z) - p(r, \theta, z + H)}{H}. \tag{5.60}$$

From Eq. 5.59, it is evident that $P(r, \theta, z) = P(r, \theta, z+H)$ completing the description of the periodic flow. In pressure-based solvers, such as SIMPLE, because the value for $\beta$ is not known a priori, it must be iterated until the specified mass flow rate for the duct is achieved. The correction of $\beta$ is performed in the

pressure-correction step, where the value of $\beta$ is updated based on the difference between the desired and calculated mass flow rates.

## 5.5 Wall treatment

As seen from the literature review, walls are the source of vorticity and the correct prediction of the flow field in its vicinities is essential. Although solving the flow field that close to the wall is much more expensive (computationally speaking) than modelling it, in the present work, wall functions are not used. The computational expense that is associated with this approach can be significant, particularly for large Reynolds number flows where the viscous sublayer can be very thin.

The transport equations are solved all the way to the wall cell. The wall shear stress is computed as:

$$\mathbf{T}_w = (\mu + \mu_t) \left[ \nabla \mathbf{u} + (\nabla \mathbf{u})^T \right]_w \tag{5.61}$$

To resolve the viscous sublayer, a sufficiently fine mesh with near-wall cells located at $y^+ < 1$ is required.

## 5.6 Initial conditions

For flows that are statistically steady, initial conditions are unimportant (CELIK, 2001). On the other hand, initiating the flow field with adequate values help to reach steadiness faster and save some CPU time.

In the present work, a steady state flow simulation using a RANS model is conducted to serve as initial field. The results are used to estimate the wall stresses from which the space and time resolution requirements may be achieved. A divergence-free perturbation field is then superimposed to the velocity field with the aid of the Synthetic Eddy Method (SEM) of Jarrin et al. (2006). For the base solution, the SST-$k\omega$ model of Menter (1992) is used.

The method requires the turbulent intensity and length scale as parameters. According to the software user manual, these informations must be retrieved from experimental data or from a previous LES or Reynolds Stress Model simulation. However, these exigencies regard the usage of the method as generating synthetic turbulence for an inflow boundary condition. For the present study, the method is used only to trigger turbulence as an initial condition. Since the flow statistics are collected after statistical steadiness, these parameter are somewhat unimportant. Therefore, for every simulation, including the test cases, the turbulence intensity was set to 10% and the length scale to the characteristic scale of the flow.

## 5.7 Resolution requirements

In implicit LES, the scale separation depends on the discretization of the flow field, which will characterize the filter width $\Delta$ and so the SGS model. Since the time-step may accompany $\Delta$, the

simulation is never grid/time-step independent. Usually, the filter width $\Delta$ and some correspondent time-step are chosen in accordance to the CPU time one is wiling to spend.

Ideally, the energy containing eddies must be resolved in all directions which implies that the cut-off wave number must lie within the inertial subrange. In terms of non-dimensional wall units, it is recommended to have $50 \leq \Delta x^+ \leq 150$, $\Delta y^+ \leq 2$ and $15 \leq \Delta z^+ \leq 40$ (Eq. 5.62), where $x$, $y$ and $z$ are the streamwise, wall-normal and spanwise directions, respectively (**??**).

$$\begin{aligned} \Delta x^+ &= \frac{u_\tau \Delta x}{\nu} \\ \Delta y^+ &= \frac{u_\tau \Delta y}{\nu} \\ \Delta z^+ &= \frac{u_\tau \Delta z}{\nu} \end{aligned} \tag{5.62}$$

where $u_\tau$ is the friction velocity defined as $u_\tau = (\tau_w/\rho)^{0.5}$. These constraints are necessary to resolve near-wall events such as bursting and sweeping and coherent structures such as hairpin vortices and slow-speed streaks.

The time-step requirement may be estimated from the Courant-Friedrichs-Lewy (CFL) number described in Eq. 5.63. For explicit marching schemes, it is recommended to stay below 1. Although implicit schemes are unconditionally stable for any size of time step (VERSTEEG; MALALASEKERA, 2007), the CFL can still be used to relate $\Delta t$ to $\Delta$.

$$\mathrm{CFL} = \frac{U\Delta t}{\Delta x} + \frac{V\Delta t}{\Delta y} + \frac{W\Delta t}{\Delta z} \tag{5.63}$$

Since the time and space discretizations are physically bounded in the case of LES, the CFL must be kept, ideally, with an unity order of magnitude along the entire domain.

## 5.8 Grid generation

The grid is orthogonal, non-uniform and structured. The meshing algorithm in STAR-CCM+ allows to work in a Cartesian coordinate system only. A representation of a grid is given in Fig. 5.3. Every element is hexahedral. The elements are stretched towards the duct centre in a hyperbolic fashion.

The hyperbolic stretching function follows the relation below:

$$s(n_i) = 1 + \frac{\tanh\left[F_s(n_i/N\ -1)\right]}{\tanh\left(F_s\right)},\ \forall\ F_s \neq 0 \tag{5.64}$$

where $N$ is the total number of layers, $n_i$ is the current node, $F_s$ the overall stretching factor and $s(n_i)$ the distribution value for the current node $n_i$. This function was chosen because this is the only option that allows a two-side stretching, that is, clustering elements in both opposite walls.

When a two-side stretching is used, the size distribution is given by two separate functions, which must converge at some point. The user must specify the value for the total number of elements $N$ and

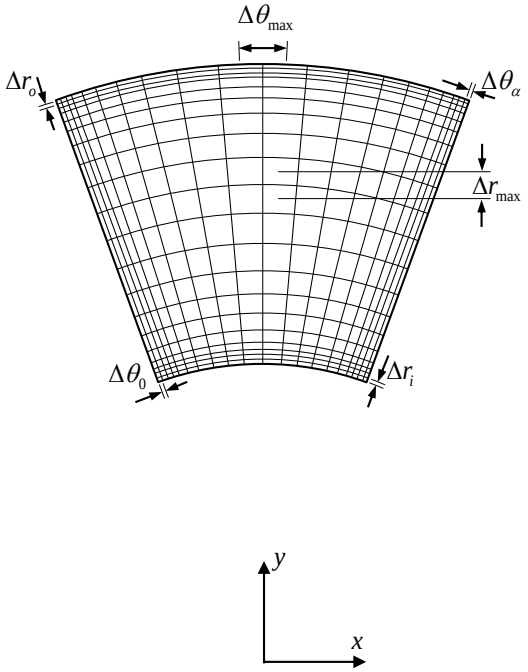


Figure 5.3 – Grid configuration

the value for $s(1)$ of both series. The value for $s(1)$ is calculated from the $\Delta r^+$ and $\Delta\theta^+$ constraints. However, the chosen value for $N$ implies $\Delta r^+_{\text{max}}$ and $\Delta\theta^+_{\text{max}}$, representing the maximum element sizes measured in wall-units. To estimate an appropriate value for $N$, the steps below were followed:

1. Evaluate each wall-average shear stress magnitude from the RANS-based solution.
2. Calculate the friction velocities from:

$$V_\tau = \sqrt{\frac{\tau_w}{\rho}} \tag{5.65}$$

3. Calculate the $s(1)$ requirements, assuming $\Delta r^+, \Delta\theta^+ = 1$, for each wall from:

$$s(1) = 2\frac{\nu}{V_\tau} \tag{5.66}$$

   From Eq. 5.66, the values for $\Delta r_i$, $\Delta r_o$, $\Delta\theta_0$ and $\Delta\theta_\alpha$ are obtained. To facilitate step 4, the smallest spacing is taken as default for every wall.

4. Estimate the number of elements $N$ for $O(\Delta^+_{\text{max}}) = 10$.

   a) Guess a value for $N$;

   b) Calculate $F_s$ from Eq. 5.64;

   c) Calculate $s(N)$;

   d) Calculate $\Delta^+_{\text{max}}$

e) Repeat until $O(\Delta^+_{\text{max}}) = 10$

5. Calculate the number of elements in the streamwise direction by:

   a) Evaluate the wall-average axial shear stress for each wall and take the greater.

   b) Calculate the number of elements assuming $\Delta z^+_{\text{max}} = 50$:

$$N_z = \frac{H}{\Delta z} = \frac{H}{\nu \Delta z^+_{\text{max}}} \sqrt{\frac{\tau_{w_z}}{\rho}} \tag{5.67}$$

   where $H$ is the unknown duct height. Some tests have revealed that using $H^* = H/D_h = 5$ is a good guess and usually respects the two-point correlation constraint. For the highest $Re_\omega$, however, smaller values for $H$ were used to reduce the computation time.

# 6 Test Cases and Grid Dependency

In this chapter, the results for the selected test cases are presented in first place and the capabilities and limitations of the method are discussed. The selected numerical schemes are then used to run a grid-independence study for the proposed problem.

## 6.1 Test case 1: Turbulent periodic channel flow

The periodic channel flow study of Moser and Moin (1987) is still a reference DNS solution in the present days. In this study, the incompressible turbulent flow within infinite parallel plane plates is solved for $Re_\tau = 180$ (based on the shear velocity and channel half-width $\delta$). The problem is known to be the simplest case from which insights on the structural and statistical characteristics of wall-bounded turbulence can be derived. Besides, the simplicity found in the geometry and boundary conditions makes it very suitable for numerical verification.

The channel geometry is presented in Fig. 6.1 along with the adopted coordinate system. The channel is characterized by the half-width $\delta$ and the periodic lengths in the streamwise $x$ and spanwise $z$ directions are $4\pi\delta$ and $2\pi\delta$ respectively.

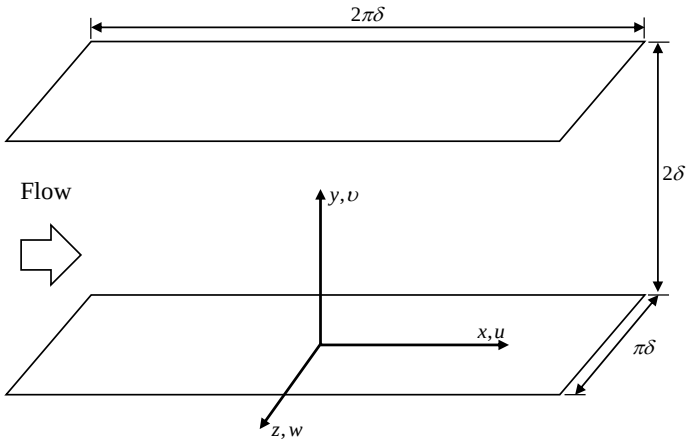


Figure 6.1 – Channel geometry and coordinate system of Moser and Moin (1987)

### 6.1.1 Grid generation

The domain dimensions are calculated for $\delta = 0.5\ \mathrm{m}$. The complete grid description is given in Table 6.1. The elements distribution in the wall-normal direction follows a hyperbolic progression adjusted to guarantee $y^+ < 1$. The total number of elements for the present study is 262,144 ($64 \times 64 \times 64$, in $x, y, z$) against 3,962,880 ($192 \times 129 \times 160$, in $x, y, z$) of Moser and Moin (1987).

Table 6.1 – Grid characteristics for Test Case 1

| **Description** | **Value** |
|---|---|
| Channel half-width $\delta$ | $0.5\ \mathrm{m}$ |
| Channel streamwise dimension $6.4\delta$ | $3.2\ \mathrm{m}$ |
| Channel spanwise dimension $3.2\delta$ | $1.6\ \mathrm{m}$ |
| $N_x$ - uniformly spaced | $64 \rightarrow \Delta_x^+ \approx 18$ |
| $N_y$ - hyperbolically distributed | $64 \rightarrow y^+ \approx 1$ |
| Maximum spacing (channel centreline) | $\Delta y^+_{\mathrm{max}} \approx 16$ |
| $N_z$ - uniformly spaced | $64 \rightarrow \Delta_z^+ \approx 9$ |

### 6.1.2 Boundary conditions and initial field

Periodicity is imposed in both spanwise and streamwise directions. The flow is driven by a constant mass flow rate which is calculated from the provided $Re_b = 5600$, based on the bulk velocity and $2\delta$. For top and bottom walls, no-slip condition is applied.

The initial flow field is taken to be the steady state solution obtained from a SST-$k\omega$ RANS-based model simulation. A random perturbation field, based on the SEM (Synthetic Eddy Method) of Jarrin et al. (2006), is then superimposed to the velocity field with 10% of turbulent intensity.

### 6.1.3 Solution method

The solution was obtained with a time-step size of $\Delta t = 0.05\ \mathrm{s}$ (CFL $\approx 0.2$). For time integration, a second-order implicit scheme was used with inner iteration convergence being assumed when all equations absolute residual reached an order of magnitude of $10^{-5}$. The flow statistics were collected for 30 flow times.

### 6.1.4 Results

The results were obtained by space averaging the time-averaged variables along the $x$- and $z$-coordinates. Table 6.2 describes the comparison of mean flow variables of the present simulation with those of Moser and Moin (1987). It is seen from 6.2 that regardless of the method employed on discretizing the convective terms, the results depart little from those of DNS. This is an expected outcome for such a simple case, considering the geometry and Reynolds number at which the flow takes place.

Table 6.2 – Mean flow variables

| **Description** | **DNS** | **BCD15 (%)** | **BCD10 (%)** | **MUSCL10 (%)** | **CDS (%)** |
|---|---|---|---|---|---|
| $U_{\mathrm{c}}/U_{\mathrm{m}}$ | 1.16 | 1.15 ($-0.86$) | 1.15 ($-0.86$) | 1.16 ($\sim$) | 1.17 (0.86) |
| $U_{\mathrm{c}}/u_\tau$ | 18.30 | 17.97 ($-1.80$) | 18.50 (1.09) | 18.29 ($-0.05$) | 17.55 ($-4.10$) |
| $U_{\mathrm{m}}/u_\tau$ | 15.68 | 16.77 ($-6.95$) | 16.03 (2.23) | 15.81 (0.83) | 15.04 ($-4.08$) |
| $Re_\tau$ | 178.12 | 167.01 ($-6.24$) | 174.73 ($-1.90$) | 177.07 ($-0.59$) | 186.15 (4.5) |

The centreline streamwise velocity was well predicted by every method, as seen from the ratio $U_c/U_m$. For the MUSCL method, the predicted value was exactly that of MMK with oscillations of less than $1\%$

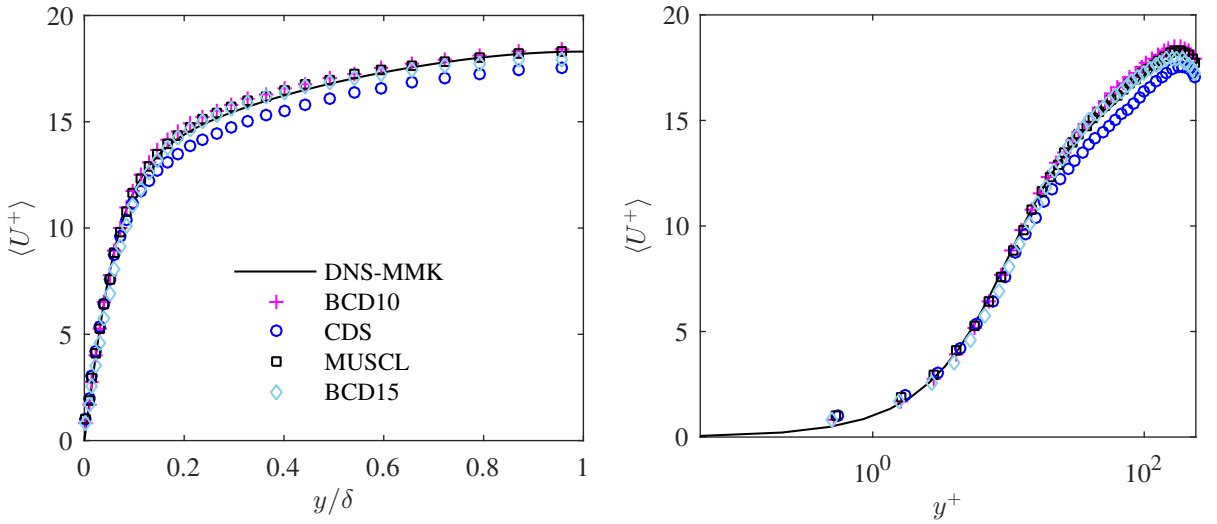


(a) Average streamwise velocity normalised by the shear velocity

(b) Average streamwise velocity normalised by the shear velocity plotted in wall units

Figure 6.2 – Mean streamwise velocity profiles

for the remaining methods. The streamwise velocity profile is given in Fig. 6.2. In Fig. 6.2a, the velocity is normalised by the shear velocity $u_\tau = \sqrt{\tau_w/\rho}$ and plotted across the channel half width. The wall normal coordinate $y$ is normalised by the channel half-width. Although both LES and DNS profiles show good agreement, a slight difference can be noticed with respect to the results obtained with the CDS method for which an overprediction in the wall-shear shifted the $U^+$ profile downwards. After the buffer layer, as seen in Fig. 6.2b as $y^+ > 10$, the upwind-dependent methods had their profiles almost collapsing over the DNS curves.

In the vicinity of the walls, every method underpredicted the velocity gradient as illustrated in Fig. 6.3. For $y^+ < 5$, known as the viscous sub-layer region, it is expected that the velocity profile assumes the form $U^+ = y^+$. Even in the DNS results, however, the curve departures from this tendency as $y^+ > 3$. Nonetheless, the discrepancy encountered for the LES results could be attributed to grid resolution within the sub-layer.

The second-order statistics are presented in Fig. 6.4. The profiles were all normalised with respect to the wall-shear velocity $u_\tau$ and are plotted across the channel half-width $0 \leq y/\delta \leq 1$.

Every quantity shown in Fig. 6.4 is expected to drop to zero at the walls. Since this is the most grid-requiring region, the upwind blending present in the methods BCD15 and BCD10 seems to provide the best results for the first few points. On the other hand, away from the walls, the less the upwinding the better the agreement with DNS data. The position and intensity of the profile peaks were better predicted by the MUSCL10 method with an excellent agreement for the $u'_{RMS}$ profile as shown in Fig. 6.4a.

## 6.2 Teste case 2: Taylor-Couette-Poiseuille flow

In order to test the code for rapidly rotating flows in the presence of curvature, the study of Poncet et al. (2014) was chosen, in which the Taylor-Couette-Poiseuille problem is numerically solved by an

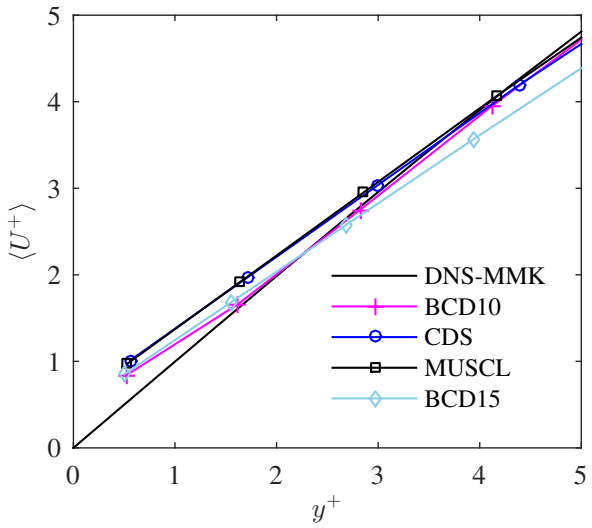


Figure 6.3 – Viscous sub-layer velocity profile

in-house spectral LES code and the results are provided with great level of detail.

The problem geometry is presented in Fig. 6.5. The values for the aspect ratio $\Gamma$, the radius ratio $\eta$, the axial Reynolds number $Re_b$ and the rotational Reynolds number $Re_\omega$ are discriminated in Table 6.3.

Table 6.3 – Geometric details for the narrow-gap cavity

| **Description** | **Value** |
|---|---|
| Aspect ratio $\Gamma = H/\Delta r$ | 10 |
| Radius ratio $\eta = r_i/r_o$ | 8/9 |
| Angular gap $\alpha$ | $\frac{3}{4}\pi$ |
| Axial Reynolds number $Re_b = W_b \Delta r/\nu$ | 3745 |
| Rotational Reynolds number $Re_\omega = \omega \Delta r r_i/\nu$ | 16755 |
| Swirl parameter $N = Re_\omega/Re_b$ | 4.47 |

## 6.2.1 Grid generation

The grid elements were distributed in order to guarantee $\Delta r^+ < 1$ in both inner and outer walls. For the streamwise and spanwise directions, the elements spacing was chosen so that $(\Delta\theta^+, \Delta z^+) \approx 50$. In the $r$-direction, the grid elements were distributed in a hyperbolic fashion while in the streamwise and spanwise directions, the element distribution was uniform. The information regarding the numerical details are shown in Table 6.4. The quantities expressed in wall-units were calculated based on the values obtained from the MUSCL10 case.

Table 6.4 – Numerical details for the narrow-gap cavity

| $\Delta r_i^+$ | $\Delta r_o^+$ | $(r_i \Delta\theta)^+$ | $(r_o \Delta\theta)^+$ | $\Delta z_i^+$ | $\Delta z_o^+$ | $N_r, N_\theta, N_z$ | $\delta t$ (CFL) |
|---|---|---|---|---|---|---|---|
| 0.20 | 0.24 | 77.83 | 78.48 | 48.82 | 45.43 | 51,131,71 | 0.05 s (0.13) |

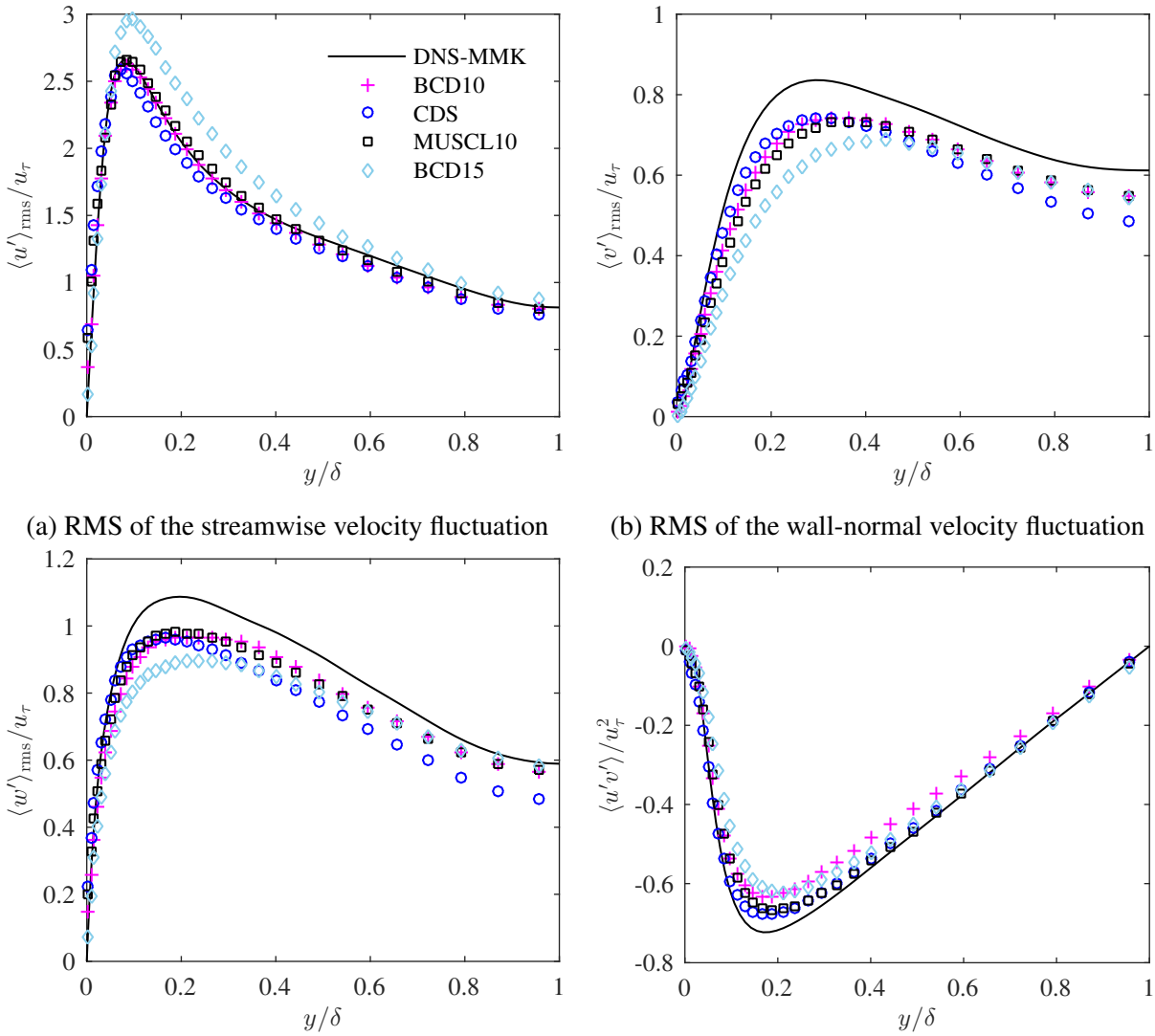


(a) RMS of the streamwise velocity fluctuation

(b) RMS of the wall-normal velocity fluctuation

(c) RMS of the spanwise velocity fluctuation

(d) Reynolds $u'v'$ shear-stress component

Figure 6.4 – Second order-statistics

### 6.2.2 Boundary conditions and initial field

For the boundaries contained in the $r\theta$-plane, translational periodicity was applied, that is $\phi(r, \theta, z) = \phi(r, \theta, z + H)$, with $\phi$ representing any flow quantity. For the boundaries contained in the $rz$-plane, rotational periodicity was applied with $\phi(r, \theta, z) = \phi(r, \theta + \alpha, z)$. The inner wall ($r = r_i$) is configured to rotate at a constant speed, obtained from $Re_\omega$, while the outer wall ($r = r_o$) remains stationary. The axial flow is driven by a constant mass flow rate obtained from $Re_Q$.

As for the channel flow case, the initial flow field was obtained from a converged steady state RANS-based solution, on which a 10% intensity turbulent field was superimposed.

### 6.2.3 Results

The results were obtained by time-averaging the flow quantities during 10 FTT's. The presented quantities were also space-averaged in the stream and spanwise directions along the entire domain.

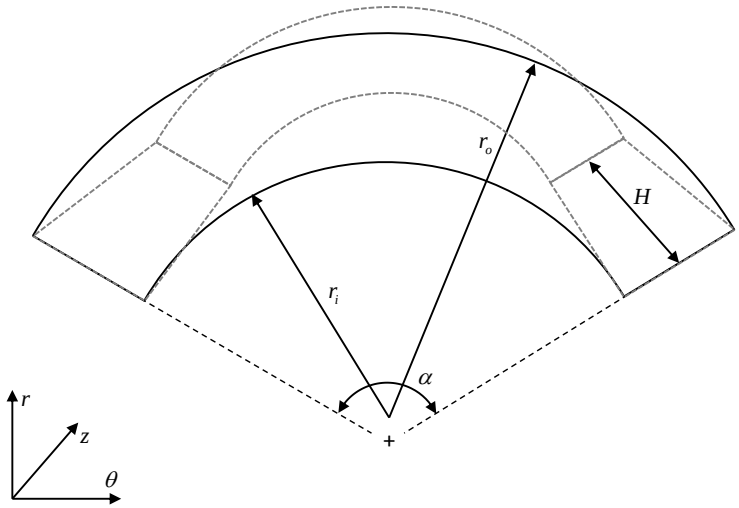


Figure 6.5 – Geometry description and coordinate system of Poncet et al. (2014)

The axial and tangential velocity profiles are presented in Fig. 6.6, both in good agreement with the reference results. From Figs. 6.6a and 6.6b, the CDS method seems to overestimate the velocity gradients near the walls. The BCD10 and MUSCL10 methods provided excellent predictions for both profiles.

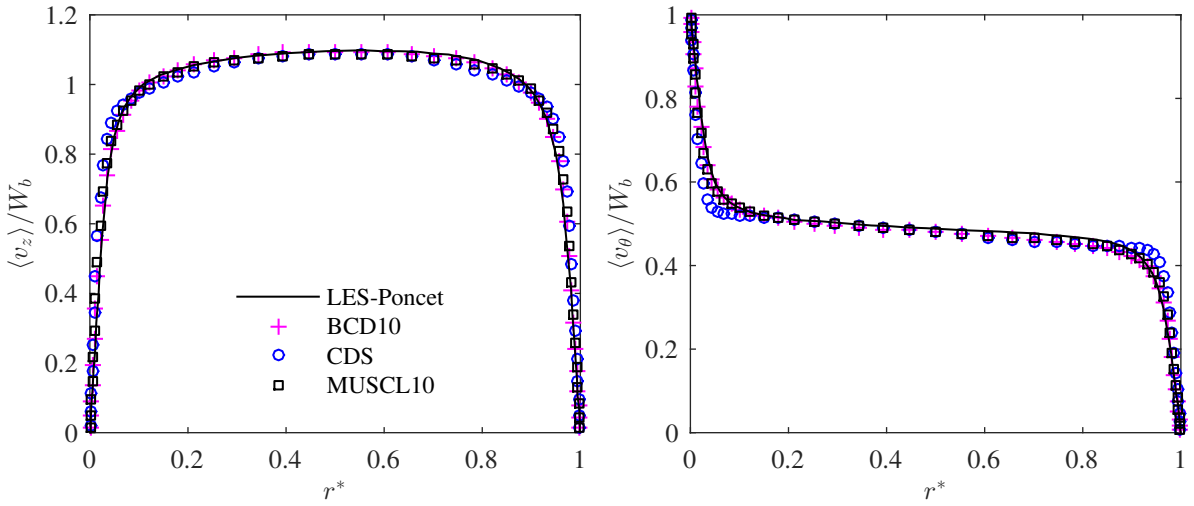


(a) Mean axial velocity profile normalised by the bulk velocity

(b) Mean tangential velocity profile normalised by the inner wall rotation speed

Figure 6.6 – Mean velocity profiles

Figure 6.7 covers the comparison of second-order quantities with the reference data. Every method provided shape-preserved profiles with qualitatively good results. Except for the axial velocity fluctuation, shown in Fig. 6.7a, the overpredictions of the CDS method for every other quantity exceeded those of the other methods. The BCD10 method provided the best predictions with a deserved highlight for the $v'_{rms}$ and $R_{r\theta}$ profiles, shown in Figs. 6.7c and 6.7d respectively.

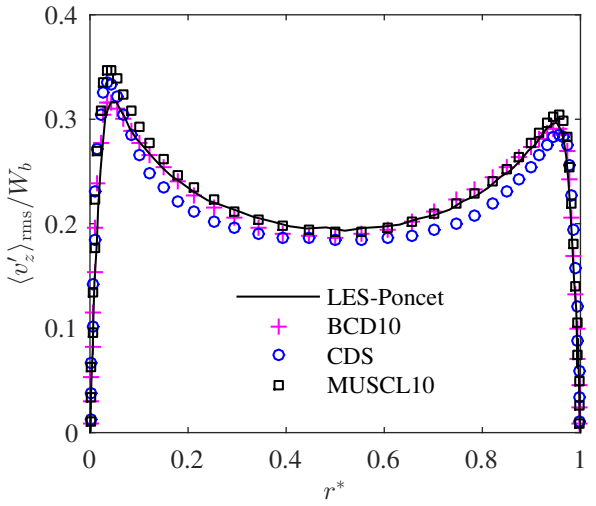


(a) RMS of axial velocity fluctuation

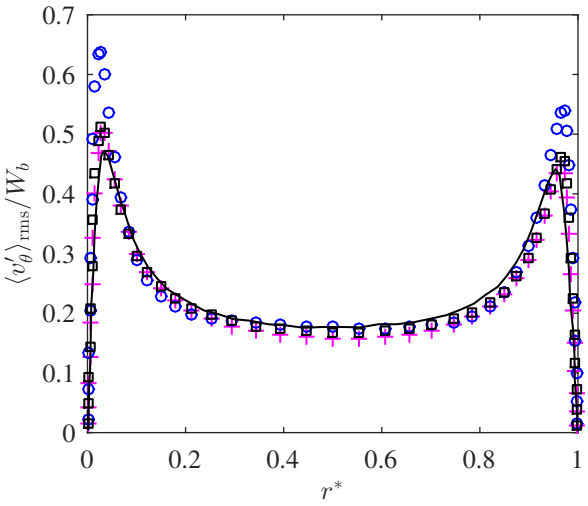


(b) RMS of tangential velocity fluctuation

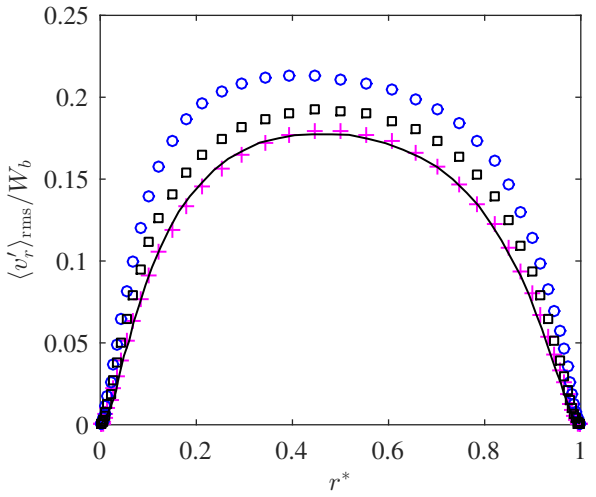


(c) RMS of radial velocity fluctuation

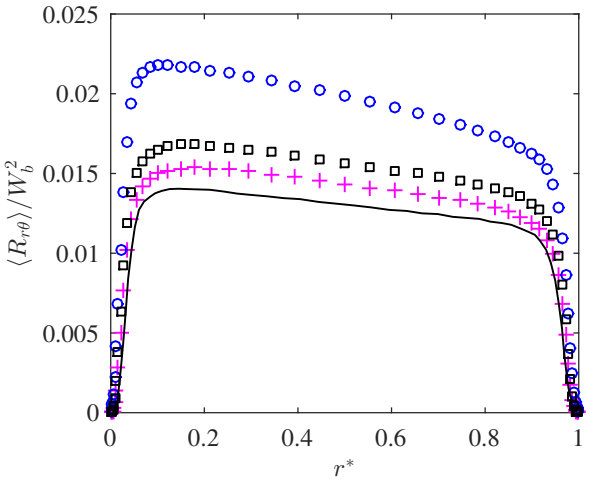


(d) Reynolds $r\theta$ stress component

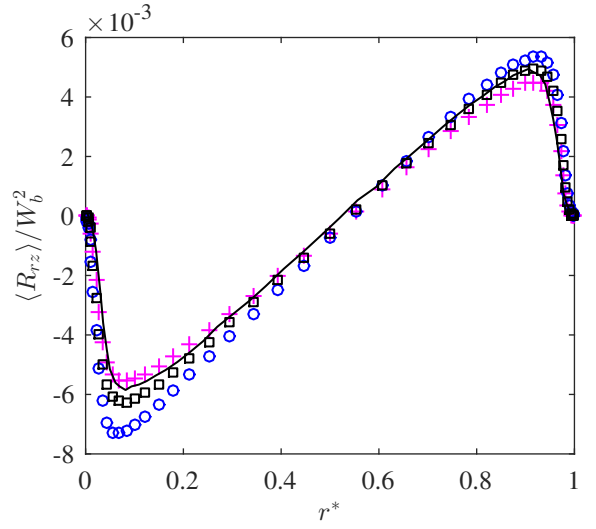


(e) Reynolds $rz$ stress component

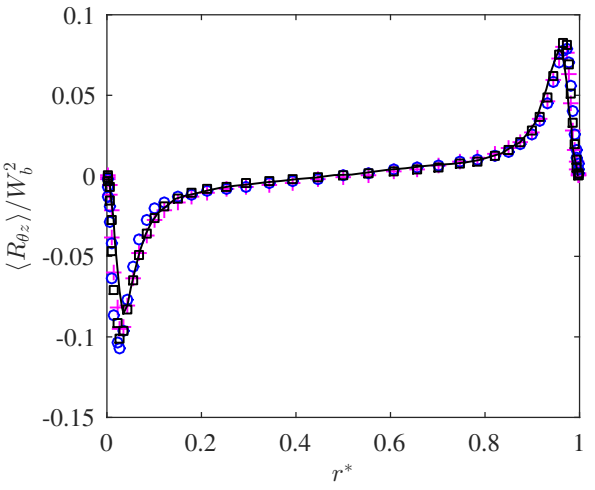


(f) Reynolds $\theta z$ stress component

Figure 6.7 – Radial distribution of second-order quantities

## 6.3 Test case 3: Square duct turbulent flow

In order to investigate the capabilities of the SGS model on dealing with anisotropic flows, the turbulent flow in a square-sectioned duct was implemented in accordance with the DNS study of Pinelli et al. (2010). It is expected that the model will be able to capture one of the distinguishable features of this flow configuration, the Prandtl's secondary motion of the second kind, which arises from the imbalance of Reynolds stresses in the duct corners.

The problem geometry is illustrated in Fig. 6.8. The duct is characterized by the half width $\delta$ and streamwise period $L = 4\pi\delta$. The coordinate system is locate at the duct centre line. The Reynolds number based on the bulk velocity and channel half width is $Re_b = 3500$.

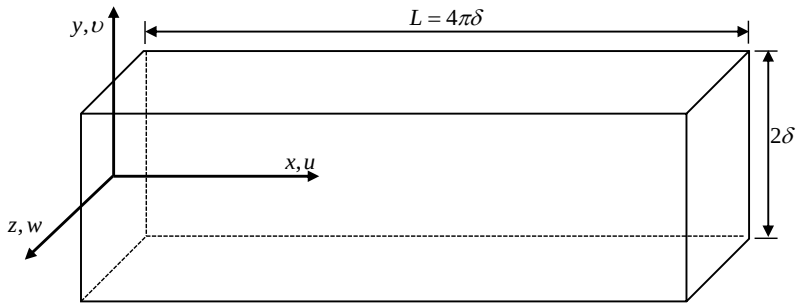


Figure 6.8 – Square duct geometry and coordinate system of Pinelli et al. (2010)

### 6.3.1 Grid generation

The duct was conceived for $\delta = 0.05$, from which any other dimension can be obtained. The grid spacing in the wall-normal directions was chosen in order to guarantee $y^+ = z^+ < 1$ with maximum spacing of $\Delta y^+_{max} = \Delta z^+_{max} \approx 20$. In the streamwise direction, the elements were uniformly distributed with $\Delta x^+ < 50$. The complete geometry and grid descriptions are found in Table 6.5.

Table 6.5 – Grid characteristics for Test Case 2

| **Description** | **Value** |
|---|---|
| Duct half-width $\delta$ | $0.05$ m |
| Duct streamwise dimension $L = 12\delta$ | $0.6$ m |
| Duct width | $0.1$ m |
| $N_x$ - uniformly spaced | $64 \rightarrow \Delta^+_x \approx 47$ |
| $N_y$ - hyperbolically spaced | $64 \rightarrow y^+ \approx 1$ |
| $N_z$ - hyperbolically spaced | $64 \rightarrow z^+ \approx 1$ |

### 6.3.2 Boundary conditions and initial field

For the duct walls, no-slip condition was applied. In the streamwise direction, fully developed flow was guaranteed by periodic boundary conditions, that is, $\phi(x, y, z) = \phi(x + L, y, z)$, with $\phi$ representing

any flow quantity. The flow was driven by a constant mass flow rate, obtained from $Re_b$.

The initial field was obtained from a converged steady-state RANS-based solution, on which a 10% intensity turbulent field was superimposed.

### 6.3.3 Results

The results were obtained by integrating the flow field for 100 FTT's after statistically steady state was achieved. The strong anisotropy requires long integration periods if one seeks to obtain symmetrical profiles as reported by Pinelli et al. (2010), who integrated for 1000 FTT's.

Figure 6.9 compares both streamwise and cross-stream velocity profiles with the reference data, obtained by $x$-averaging over a plane located at $z/\delta = -0.7$ and normalizing by the bulk velocity $U_b$. Averaging over both coordinates helps to decrease the required integration time to obtain quasi-symmetrical profiles. As seen from Fig. 6.9b, only the CDS method delivered a quasi-symmetrical profile for the cross-stream velocity. Specifically for this quantity, the experimental results of Kawahara et al. (2000) retrieved from Pinnelis's paper are shown to illustrate that perfect symmetry was not obtained. Nonetheless, comparing the streamwise and cross-stream velocity magnitudes, it can be said that the results obtained from the LES computations compare favourably to the reference data.

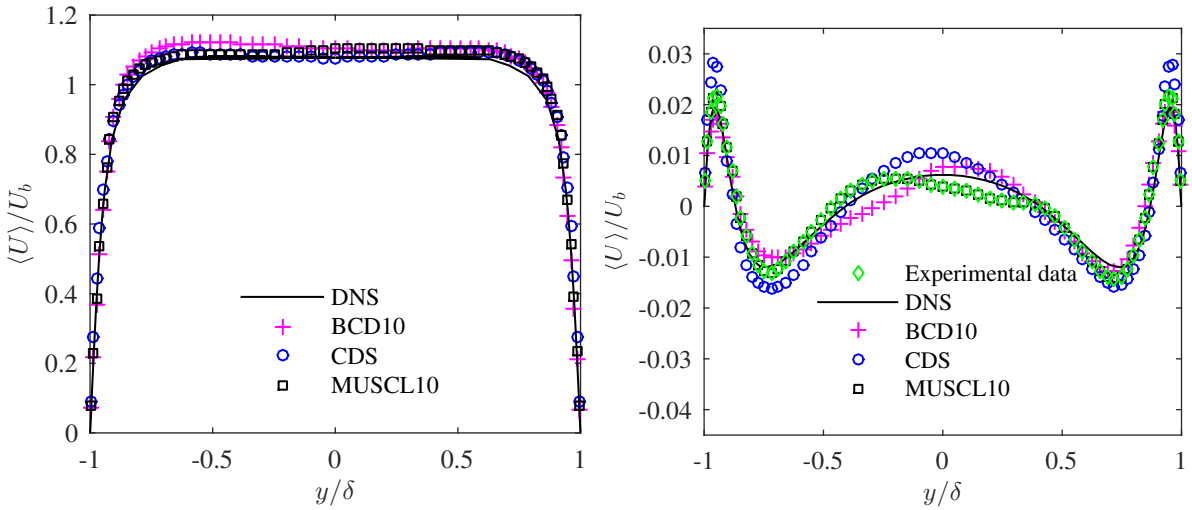


(a) Mean streamwise velocity profile

(b) Mean cross-stream velocity profile

Figure 6.9 – Mean streamwise and cross-stream velocity profiles evaluated at $z/h = -0.7$

The root-mean-square of the streamwise and cross-stream velocities are shown in Fig. 6.10. The profiles were obtained by $x$-averaging over planes located at $z/h = -0.7$ and normalised by the flow bulk velocity. No significant difference can be noticed for the streamwise velocity profile, shown in Fig. 6.10a. Regardless of the utilized method, the LES profiles agree well with the reference solution. For the cross-stream velocity fluctuation, however, the CDS method overpredicted the peaks in more than 20%, misrepresenting the profile shape. The upwind-dependent methods, in the other hand, provided qualitatively good results with and average underprediction of about 10% for the MUSCL10.

Figure 6.11 illustrates the shear-stress distribution along the duct walls. The profile was normalised by the wall mean shear-stress and plotted in wall units. The MUSCL10 method delivered the best qualitative

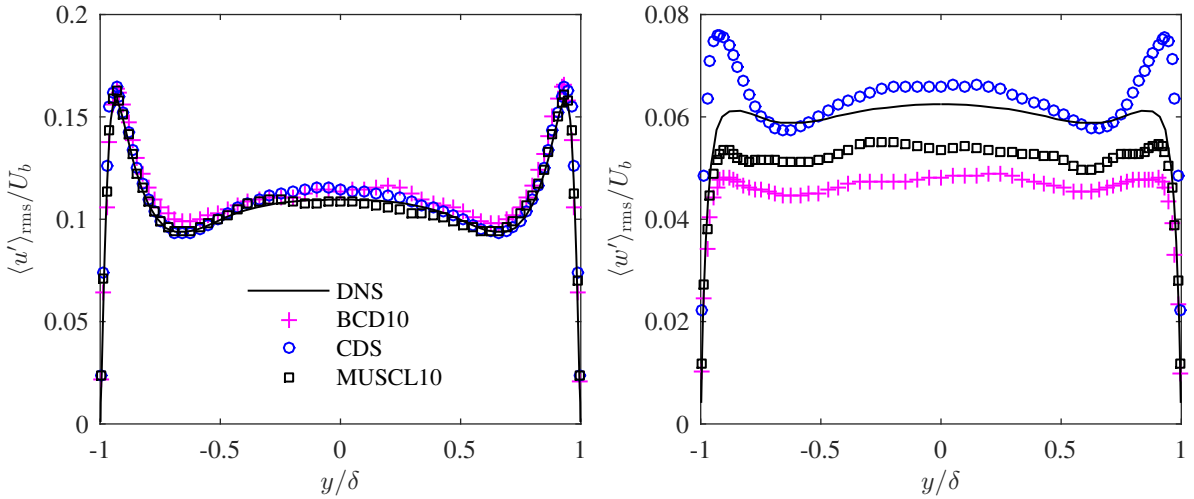


(a) RMS of streamwise velocity fluctuation (b) RMS of cross-stream velocity fluctuation

Figure 6.10 – Root mean square of streamwise and cross-stream velocity fluctuations evaluated at $z/h = -0.7$

and quantitative results, predicting both profile shape and wall shear magnitude more accurately than the other methods. Preserving the shear-stress profile is a desirable feature since the maxima and minima represent the position of high and low velocity streaks, respectively (PINELLI et al., 2010).

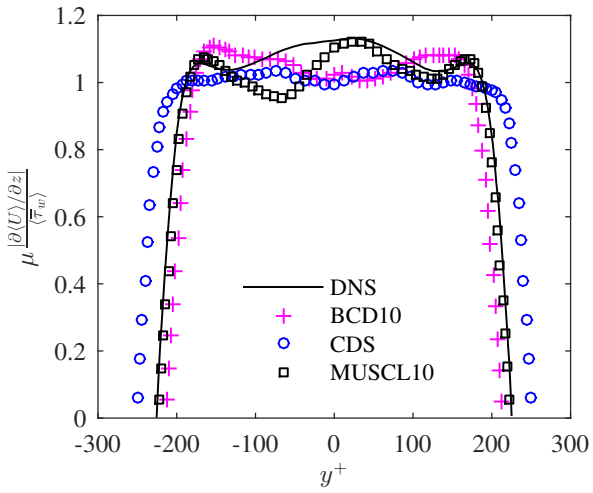


Figure 6.11 – Shear stress distribution along the wall

Finally, Fig. 6.12 shows the line integral convolution (CABRAL; LEEDOM, 1993) of the the secondary motion averaged over 100 FTT's. As mentioned before, the best method on providing symmetrical results was the CDS, which can now be confirmed by comparing Fig. 6.12c with 6.12d. However, the other methods were also able to deliver qualitatively good results. It is noteworthy to say that the statistics were collected for only a tenth of the reference results and maybe, it wasn't enough to achieve the desired symmetry. The maximum intensity of the secondary motion is also displayed in Fig. 6.12. Madabhushi and Vanka (1991) reported a maximum intensity of 2.5% of the bulk flow. In that sense, the best agreement was achieved with the MUSCL10 method and the highest deviation was attributed to the CDS method.

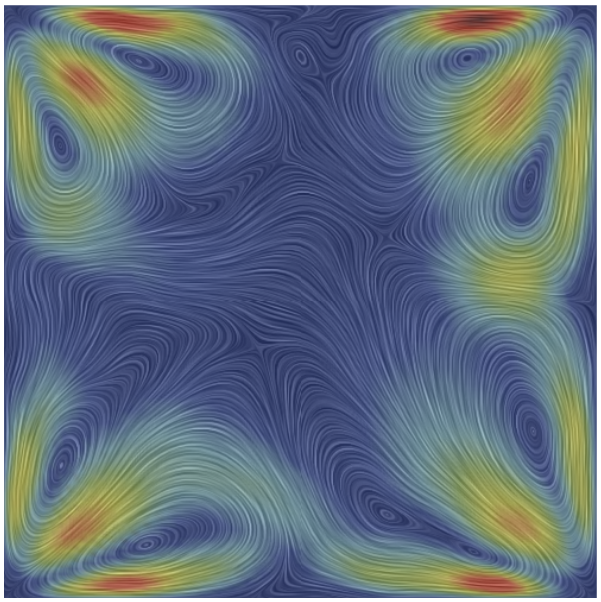

(a) BCD10 - 3.21% intensity

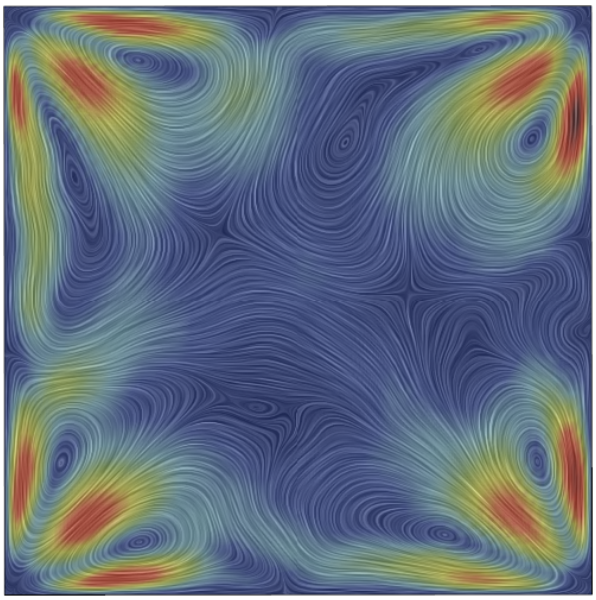

(b) MUSCL10 - 2.52% intensity

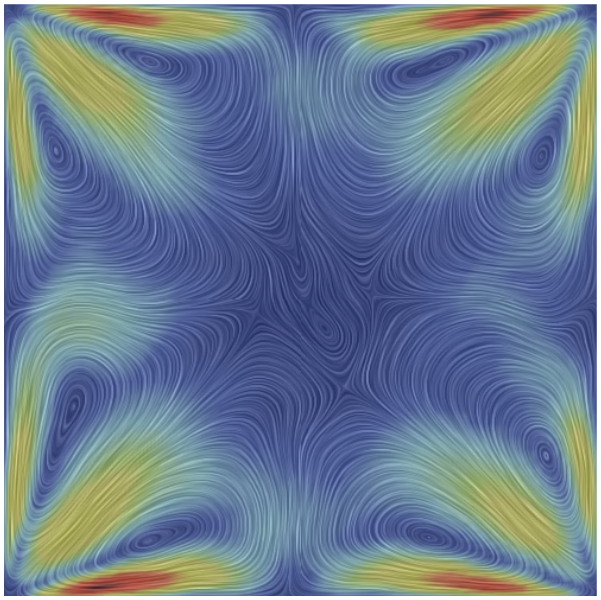

(c) CDS - 4.43% intensity

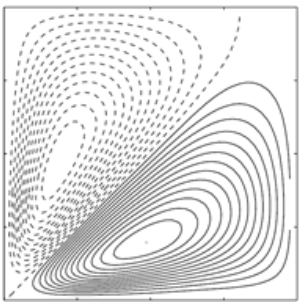

(d) DNS

Figure 6.12 – Line integral convolution of the mean secondary motion obtained with (a) BCD10, (b) MUSCL10, (c) CDS methods. (d) DNS solution of Pinelli et al. (2010)

## 6.4 Grid dependency test

From the test cases presented above, the MUSCL method with 10% of upwinding was selected as the default scheme for the discretization of convective terms. In order to investigate the adequate spacial discretization for the annular-sector problem, a grid dependence test was conducted as presented in Tab. 6.6 with the main purpose of investigating the maximum element spacing influence and the appropriate duct height. The geometry of the annular-sector is defined by the angular gap $\alpha = 40°$, a radius ratio $\eta = 0.5$, outer radius $R = 2m$ and height $H = 10D_h$ (10 times the hydraulic diameter). The axial and rotational Reynolds numbers are $Re_\omega = Re_b = 5800$. The number of elements in the wall-normal directions was increased in a factor of 1.5. In the streamwise direction, 117 elements ($\Delta z^+_{\text{max}} \approx 50$)

elements were used. The size of the wall-adjacent elements for both $r$- and $\theta$-directions were set the same for every case.

Table 6.6 – Numerical details of the grid-independence test

| **Case** | **A** | **B** | **C** |
|---|---|---|---|
| $N_r$, $N_\theta$, $N_z$ | 31, 31, 117 | 45, 45, 117 | 69, 69, 117 |
| $\Delta r_i^+$,$\Delta r_o^+$, $\Delta r_{\max}^+$ | 0.49, 1.04, 92.19 | 0.49, 1.04, 55.92 | 0.50, 1.04, 32.22 |
| $\Delta\theta_0^+$,$\Delta\theta_\alpha^+$, $\Delta\theta_{\max}^+$ | 0.84, 0.53, 129.90 | 0.83, 0.53, 72.56 | 0.83, 0.53, 49.10 |
| $\Delta z_{\max}^+$ | 52.87 | 51.72 | 51.69 |
| $\Delta t$ [s] | 0.01 | 0.01 | 0.01 |
| $\mathrm{CFL}_{\max}$ | 0.67 | 0.65 | 0.65 |
| CPU time [hr] | 225.40 | 551.59 | 668.69 |
| FTT | 13.65 | 18.58 | 15.78 |

As mentioned before, the duct height must be such that will cause no interference in the results due to the periodic boundary condition. In order to verify that, two-point correlation functions were used. As shown in Fig. 6.13, the correlation function $R_{ii}$ for each velocity component falls to zero before the maximum streamwise separation, which is located at $\approx 5D_h$ due to the symmetry imposed by the periodic condition. Since the grid dependency was conducted with the lowest $Re_\omega$, a duct height of about $5D_h$ may fit the other cases.

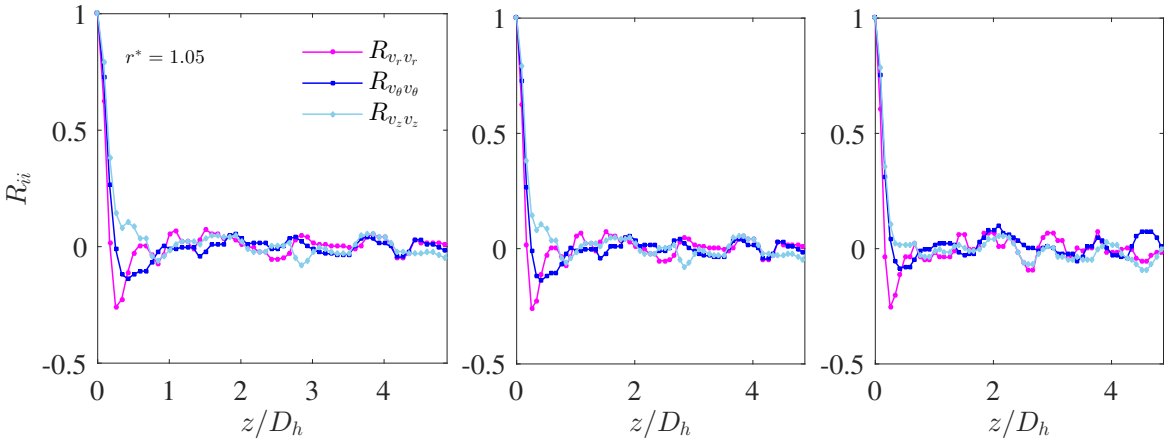


(a) CASE-A (b) CASE-B (c) CASE-C

Figure 6.13 – Two-point correlation functions evaluated at $r^* = 1.05$

Table 6.7 compares the resulting surface-averaged wall shear stress magnitude for each solid boundary of each case. The percentage difference from Case-A to B does not exceed 6% and falls to less than 2% when Cases B and C are compared. This is an expected outcome due to the nature of the hyperbolic stretching function as shown in Fig. 6.14. It is seen that, for the amount of elements that was used, the size of the first 5 elements is almost indistinguishable among the grids.

The friction factor $f$ is compared in Tab. 6.8. Since it is obtained from an integral force balance across the duct, the percentage difference range found in the results are similar to that of the stresses. The friction

Table 6.7 – Surface average of the time-averaged wall shear stress magnitude

| **Case** | **A** | **B** | $[\%]_{BA}$ | **C** | $[\%]_{CB}$ |
|---|---|---|---|---|---|
| $\langle\tau_w\rangle\|_{r=\eta R}$ | 0.0142 | 0.0150 | 5.76 | 0.0153 | 1.57 |
| $\langle\tau_w\rangle\|_{r=R}$ | 0.0662 | 0.0671 | 1.40 | 0.0673 | 0.22 |
| $\langle\tau_w\rangle\|_{\theta=0}$ | 0.0447 | 0.0430 | -3.68 | 0.0431 | 0.09 |
| $\langle\tau_w\rangle\|_{\theta=\alpha}$ | 0.0170 | 0.0175 | 3.03 | 0.0177 | 0.69 |

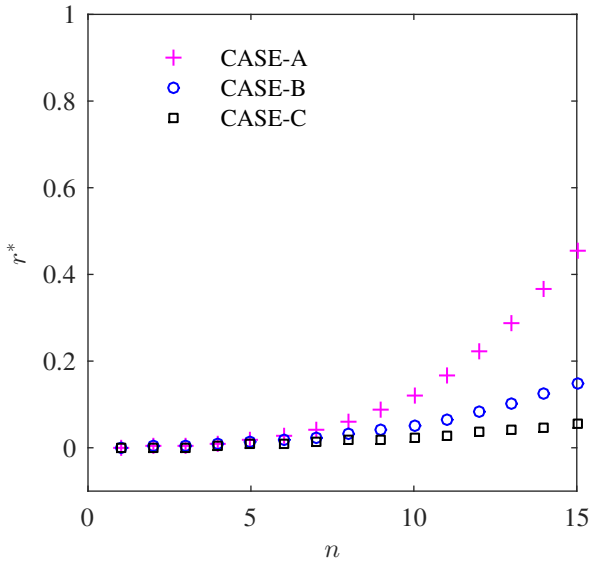


Figure 6.14 – Radial distribution of the first 15 grid elements

factor is obtained as described in Eq. 6.1.

$$f = \frac{-d\overline{P}/dz}{0.5\rho W_b^2} D_h \tag{6.1}$$

Table 6.8 – Friction factor dependence on the grid resoltuion

| **Case** | **A** | **B** | $[\%]_{BA}$ | **C** | $[\%]_{CB}$ |
|---|---|---|---|---|---|
| $f$ | 0.1603 | 0.1610 | 0.45 | 0.1615 | 0.32 |

First and second order quantities profiles were compared at three different plane sections as illustrated in Fig. 6.15. The $r$-$z$ planes are located at 20%, 50% and 80% of $\alpha$. The quantities were averaged in the streamwise direction.

Figure 6.16 shows the mean velocity profiles at $\theta = 0.2\alpha$. As mentioned before, in the near-wall region, the profiles behave similarly such that the curves overlap one another. In the bulk flow region, however, Case-A departs from the others. The local maximum for $\langle v_z\rangle$ is anticipated in Case-A, as shown in Fig. 6.16a. In Fig. 6.16b, the local minimum for $\langle v_\theta\rangle$ is underpredicted in Case-A which also fails to capture the profile inflexions. For Case-B and C, the profiles agree.

At the centre plane, as shown in Fig. 6.17, the three tested grids delivered similar results. The exception is for Case-A in Fig. 6.17b, in which the local maximum for the $\langle v_\theta\rangle$ profile is underpredicted.

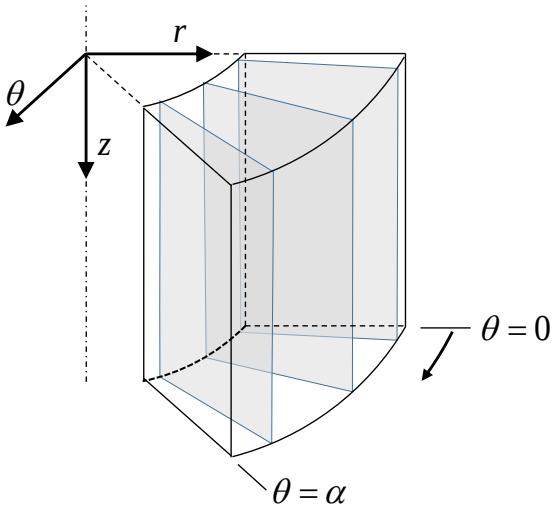


Figure 6.15 – Section planes for the flow quantities evaluation

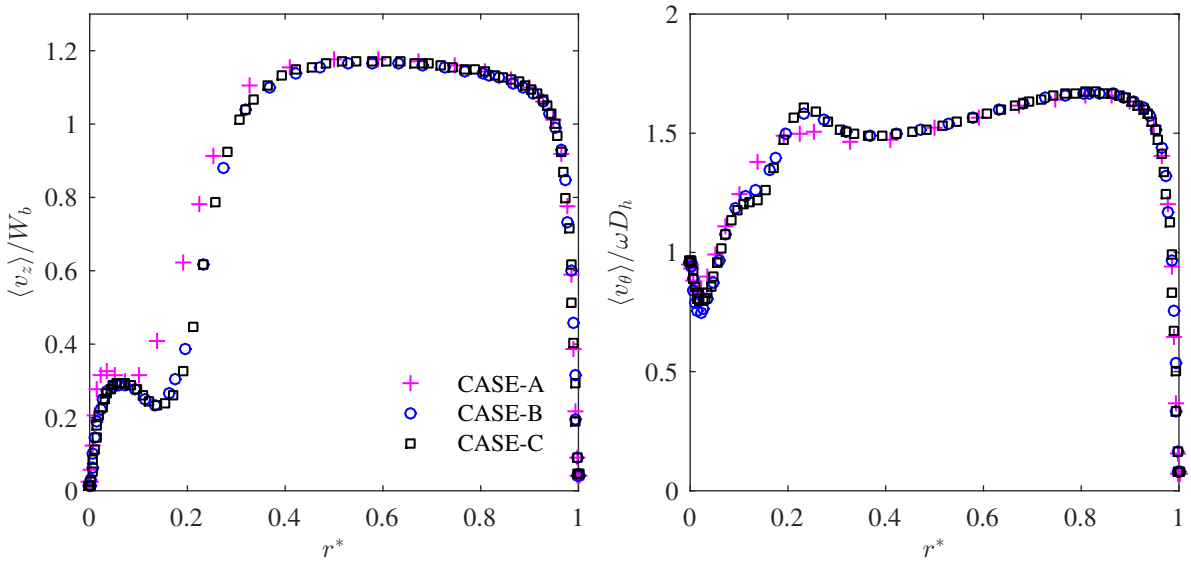


(a) Mean streamwise velocity $< v_z >$ (b) Mean tangential velocity $< v_\theta >$

Figure 6.16 – Mean velocity field evaluated at $\theta = 0.2\alpha$

For the plane located at $\theta = 0.8\alpha$, cases B and C show excellent agreement for both $\langle v_z \rangle$ and $\langle v_\theta \rangle$ profiles, as seen in Fig. 6.18.

Lastly, the profiles for the axial and tangential fluctuations are presented in Fig. 6.19. For the Case-A profiles, the fluctuation intensities are overpredicted towards the inner wall and underpredicted in outer wall region.

One last test, in the absence of experimental or DNS data to compare with, is to use the ratio of the SGS viscosity to molecular viscosity $\mu_{SGS}/\mu$. When this ratio is not more than the order of 10, the LES solution is considered to be very accurate. When it reaches 100, the simulation is found to be somewhat inaccurate (DURBIN; REIF, 2011). Since $\mu_{SGS}$ depends on the grid refinement, it decreases as the number

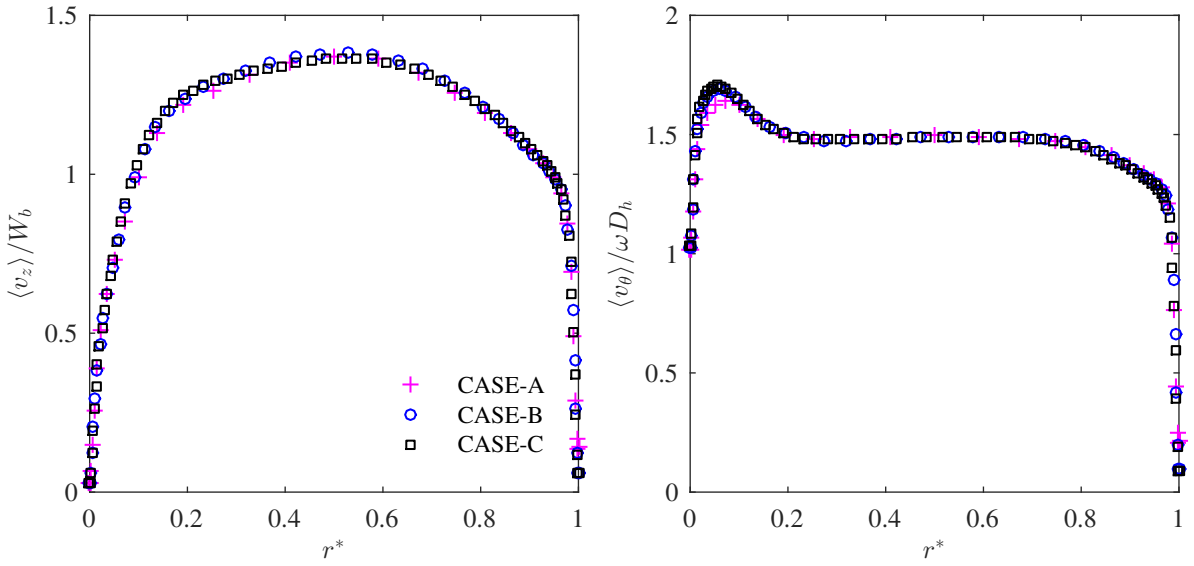


(a) Mean streamwise velocity $< v_z >$ (b) Mean tangential velocity $< v_\theta >$

Figure 6.17 – Mean velocity field evaluated at the duct centre plane $\theta = 0.5\alpha$

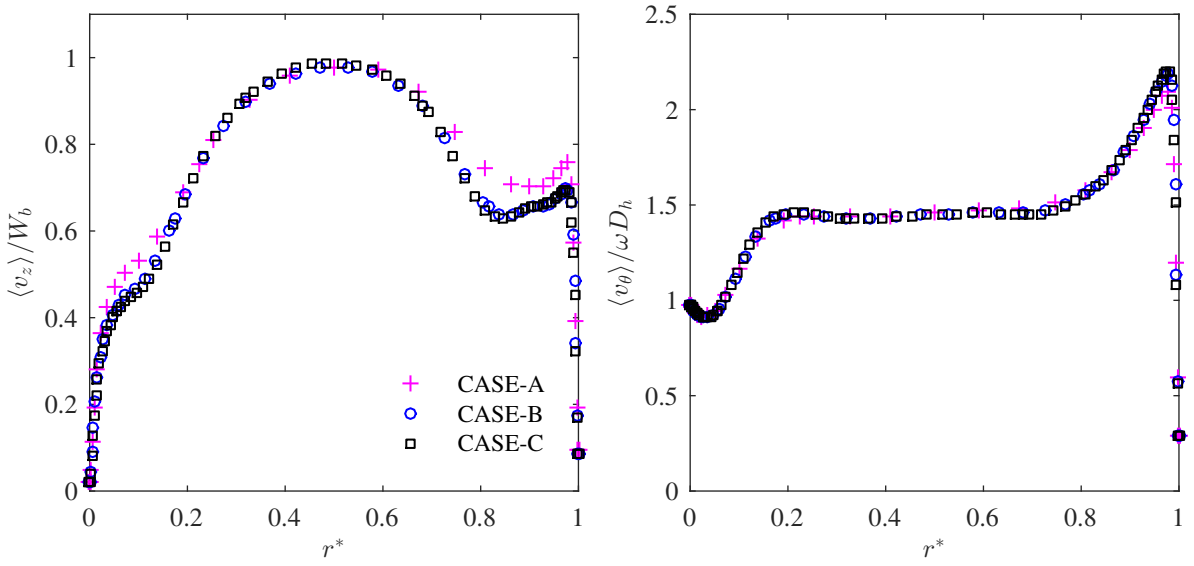


(a) Mean streamwise velocity $< v_z >$ (b) Mean tangential velocity $< v_\theta >$

Figure 6.18 – Mean velocity field evaluated at $\theta = 0.8\alpha$

of elements increases. A SGS model activity parameter is then defined as:

$$s = \frac{\mu_{\text{SGS}}}{\mu_{\text{SGS}} + \mu} \tag{6.2}$$

which ranges between zero and unity, with zero corresponding to DNS and unity to a very coarse-grid LES. Unfortunately, STAR-CCM+ does not export $\mu_{\text{SGS}}$ as a field variable. An alternative is to consider the ratio of the SGS kinetic energy $k_{\text{SGS}}$ to the total kinetic energy ($k_{\text{SGS}} + k$, with $k$ representing the

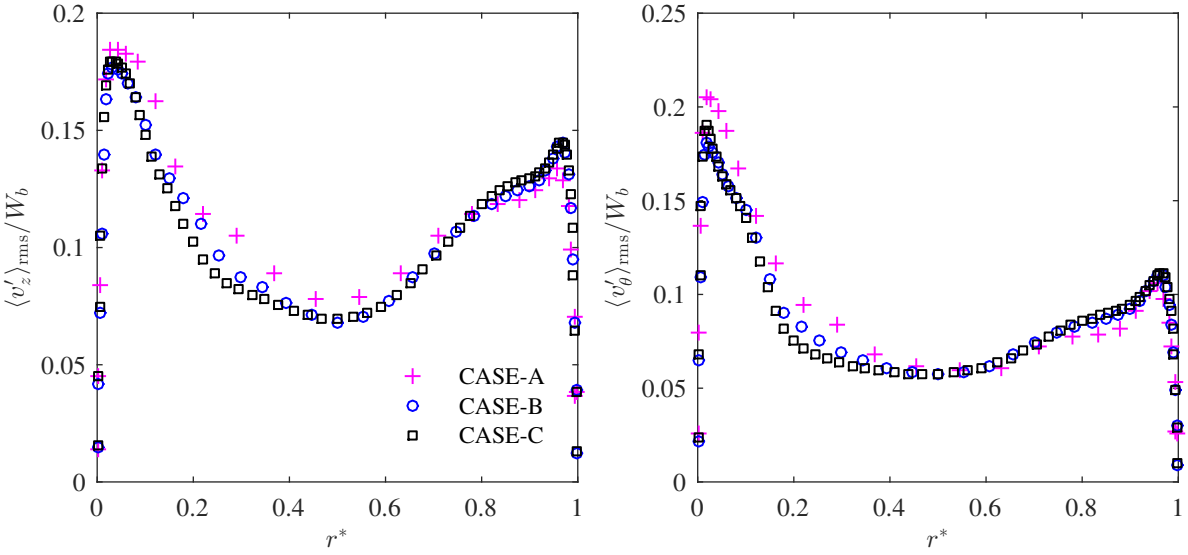


(a) RMS of the streamwise velocity fluctuation

(b) RMS of the tangential velocity fluctuation

Figure 6.19 – Root mean square of the axial and tangential velocity fluctuation components evaluated at $\theta = 0.5\alpha$

resolved turbulent kinetic energy). Therefore, $s$ may be redefined as:

$$s = \frac{k_{\mathrm{SGS}}}{k_{\mathrm{SGS}} + k} \tag{6.3}$$

which also ranges from zero to one, with $s = 0$ representing a DNS solution and $s = 1$ a RANS solution. The software manual recommends to stay within $0.05 < s < 0.10$ but does not stablish any criterion to calculate it, that is, it does not mention if the reference value for $s$ must be taken as the domain average or maximum. The criterion used in this study is to compare the maximum value of $s$ among 90% of the grid cells.

Figure 6.20 shows the relative frequency distribution of $s$ divided in 50 bins. The vertical lines represent the thresholds for 90% of the grid cells. As mentioned before, refining the grid diminishes the influence of the SGS model. For Case-C, the maximum value for $s$ is lower than 0.1 for 90% of the grid cells. On the other hand, the comparisons with Case-B have shown very good agreements, even with the threshold extended to 0.30.

From Tab. 6.6, the CPU time demand for each case can be adjusted, for the sake of comparison, to 10 FTT. This would leave Case-A, B and C, with around 165, 297 and 424 hours, respectively. The results have shown that the Case-A grid is too coarse to capture some details such as profile inflexions. Case-C, in the other extreme, demands too much CPU time while its results agree well with Case-B grid, which saves about 30% of CPU time. Therefore, for the continuation of the study, grids with characteristics as in Case-B will be taken as default.

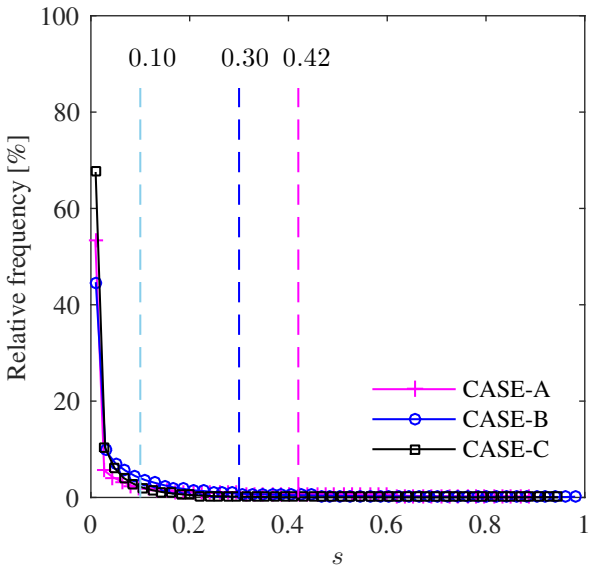


Figure 6.20 – Relative frequency distribution of $s$

# 7 Results

In this chapter, results for the turbulent flow in the annular-sector duct are presented. Firstly, the solution is obtained for a non-rotating duct with stationary walls so that it can be qualitatively compared to the square duct case of Pinelli et al. (2010). Secondly, the duct is put to rotate in order to investigate the influence of rotation. Lastly, the combined shear-induced and rotation effects are investigated and the influence of the governing parameters is presented.

## 7.1 Cases summary

The problem investigation was carried out as presented in Tab. 7.1. Case **A** is a non-rotating case with stationary outer wall (relative to the RRF). In Case **B**, the duct is put to rotate but the outer wall remains stationary (relative to the RRF), that is, $\mathbf{u}(r = R, \theta, z) = 0$. The **C** group investigates the rotational speed influence by means of the swirl parameter $\Gamma$. Henceforward, the boundary conditions are as described in section 4.2. Group **D** simulations vary the duct apex angle $\alpha$ and finally, group **E** brings the effect of the radius ratio $\eta$.

Table 7.1 – Numerical details of the parametric investigation

| | **Parameters** | | | |
|---|---|---|---|---|
| **Case** | $Re_b = \frac{W_b D_h}{\nu}$ | $\Gamma = \frac{\omega D_h}{W_b}$ | $\alpha$ [°] | $\eta = \frac{r_i}{r_o}$ |
| **A** | 5800 | 0 | 40 | 0.5 |
| **B** | 5800 | 1 | 40 | 0.5 |
| **C1** | | 1 | | |
| **C2** | 5800 | 5 | 40 | 0.5 |
| **C3** | | 10 | | |
| **D1** | | | 15 | |
| **D2** | 5800 | 1 | 40 | 0.5 |
| **D3** | | | 75 | |
| **E1** | | | | 0.3 |
| **E2** | 5800 | 1 | 40 | 0.5 |
| **E3** | | | | 0.7 |

Although cases C1, D2 and E2 represent the same simulation, they were renamed according to the parameter group that is being analysed during the results discussion.

For every case, the flow field was calculated until two-point correlation functions $R_{uu}$ stopped varying in time, which took approximately 3 flow-through time periods (FTT $= h/W_b$). At this stage, the flow is said to be statistically steady (DAVIDSON, 2004). The statistics were then collected for at least 10 FTT but the precise time can be found in the details table presented for each case along with the required CPU time. The simulations were all performed in Intel Core i7-6700K (4.00 GHz) 16GB RAM desktops running Windows 10.

## 7.2 Stationary duct

The stationary duct case, referred as Case A in Tab. 7.1, was investigated to seek some similarity with the turbulent square duct case of Pinelli et al. (2010), presented in Chaper 6, as well as to serve as a base for comparison with the other cases. The grid characteristics are given in Tab. 7.2 along with the flow integration time.

Table 7.2 – Numerical details of Case A

| $H^*$ | $R[m]$ | $N_r$,$N_\theta$,$N_z$ | $\Delta r_i^+(\Delta r_o^+)$ | $\Delta\theta_0^+(\Delta\theta_\alpha^+)$ | $\delta t[s]$ | $\text{CFL}_{\text{max}}$ | FTT | CPU [hr] |
|---|---|---|---|---|---|---|---|---|
| 4 | 2 | 45, 45, 47 | 0.357 (0.3309) | 0.3550 (0.3529) | 0.020 | 0.038 | 103 | 423.28 |

Figure 7.1 shows both instantaneous and time-averaged secondary velocity field for Case A, obtained from Eqs. 7.1 and 7.2, respectively.

$$\mathbf{u}_s = v_r\hat{e}_r + v_\theta\hat{e}_\theta \tag{7.1}$$

$$\langle\mathbf{u}_s\rangle = \langle v_r\rangle\hat{e}_r + \langle v_\theta\rangle\hat{e}_\theta \tag{7.2}$$

The vector magnitudes are normalised by the bulk velocity $W_b$. The secondary velocity field in Fig. 7.1b presents the same pattern seen for the square duct (Fig. 6.12), that is, the Prandtl's secondary motion of second kind (MADABHUSHI; VANKA, 1991). The flow splits up in an octant fashion with counter-rotating vortices that reach 2.6% of the bulk flow intensity, which agrees well with the study of Madabhushi and Vanka (1991), that reported a 2.5% intensity for the square duct case at $Re_b = 3500$. The absence of rotation allows symmetry to take place in the $\theta$-direction with the symmetry plane located at $\theta = \alpha/2$. However, as in the square duct case presented in Section 6.2, the flow was not integrated long enough ir order to a perfect symmetric secondary field to be verified.

In Fig. 7.1a, the line integral convolution (CABRAL; LEEDOM, 1993) of the instantaneous secondary velocity field is displayed. Vortical structures on a wide range of scales can be perceived. The velocity magnitude for the instantaneous motion can be as large as 5 times its mean counterpart, reaching up to 14% of the bulk flow intensity as illustrated by the dark red shades, highlighting the effect of turbulence on mean flow momentum.

Figure 7.2 shows the mean streamwise velocity contours normalised by $W_b$. The secondary velocity field convect mean-flow momentum from the central region to the corner region along the corner bisectors (MADABHUSHI; VANKA, 1991). This is evidenced by the associated distortion of the profile towards the duct corners.

The mean streamwise velocity and the RMS of its fluctuating quantity are shown in Fig. 7.3. The profiles were evaluated at $z = 0.7\delta$ and $\theta = 0.7(\alpha/2)$, for the square duct and Case A, respectively. The wall-normal coordinate for the square duct was translated to lie between $0 \leq y/\delta \leq 1$. In Fig. 7.3a, the effect of the shear stress difference between inner and outer walls appears as the velocity profile peaks closer to the outer wall, where shear stresses are smaller. Nevertheless, the resemblance found for the geometries is notable, both in shape and intensity.

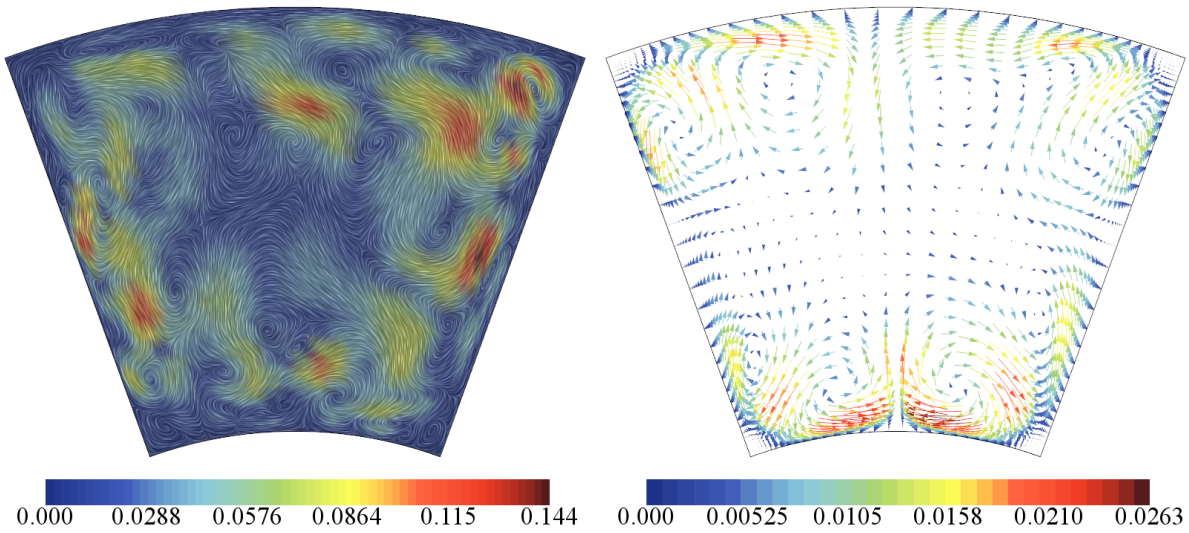


(a) Line integral convolution of the instantaneous secondary field

(b) Mean secondary field

Figure 7.1 – Secondary velocity field normalised by the bulk velocity

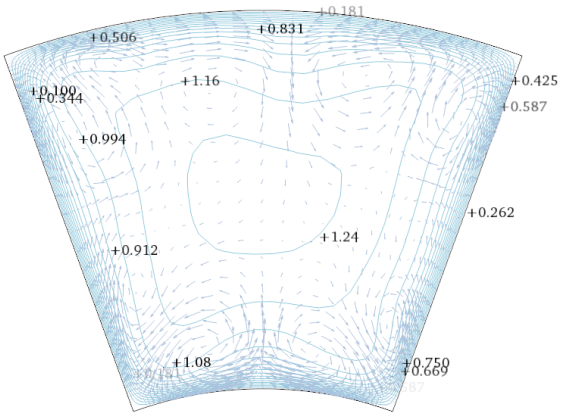


Figure 7.2 – Contours of the mean streamwise velocity normalised by $W_b$ superposed on the secondary velocity field. The isolines are distorted towards the corners as a result of the secondary motion effect

In Fig. 7.3b, the mean streamwise velocity fluctuation profiles overlap close to the walls. The Case A profile does not present symmetry as in the square duct case as turbulence intensity decreases towards $r^* = 0$. The smaller turbulent kinetic energy in the inner wall may be attributed to the transverse curvature effect. Since the surface area of the inner wall is smaller than that of the outer wall, it supplies relatively less turbulent kinetic energy than the outer wall to the same volume of flow (CHUNG et al., 2002).

Intriguingly, at the duct symmetry plane ($\theta = 0.5\alpha$), the profiles for $\langle v_z \rangle$ and $\langle v_z' \rangle_{\mathrm{rms}}$ do not show the same trend, as represented in Fig. 7.4. The streamwise velocity is compared with that of the square duct case, evaluated at the symmetry plane, and the DNS study of Chung et al. (2002) for the concentric cylinders problem. Although the DNS results were obtained for the same radius ratio and $Re_{Dh} = 8900$,

both $\langle v_z \rangle$ and $\langle v_z' \rangle_{\text{rms}}$ profiles are strikingly symmetric along the $r$-direction and similar to those of the square duct case.

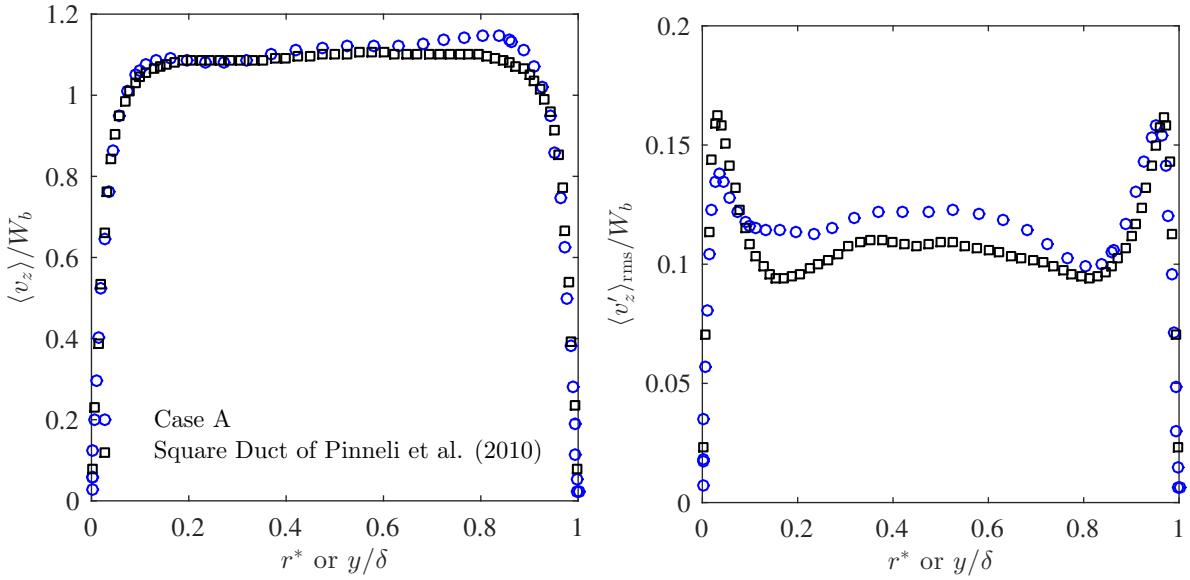


(a) Mean streamwise velocity (b) RMS of streamwise velocity fluctuation

Figure 7.3 – Mean streamwise velocity and RMS of streamwise velocity fluctuation evaluated at $\theta = 0.7(\alpha/2)$ for Case **A** and $z = -0.7\delta$ for the square duct

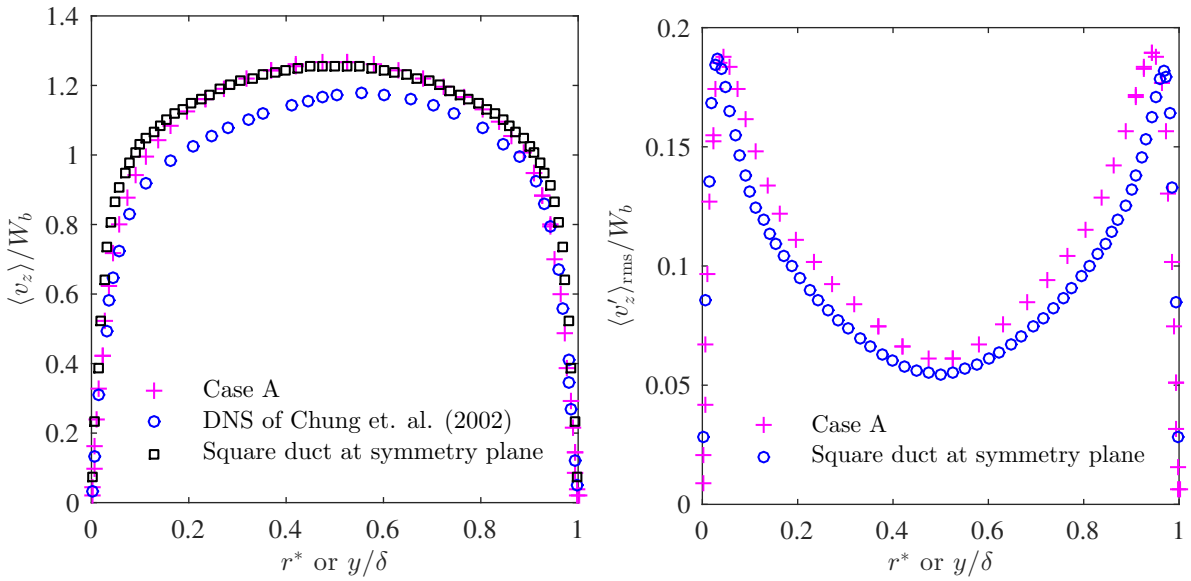


(a) Mean streamwise velocity (b) RMS of streamwise velocity fluctuation

Figure 7.4 – Mean streamwise velocity and RMS of streamwise velocity fluctuation evaluated at $\theta = 0.5$ for Case **A** and $z = 0$ for the square duct

The shear stress distributions along the inner and outer walls are represented in Fig. 7.5. The profiles were normalised by the wall-averaged shear stress magnitude $\langle \overline{\tau}_w \rangle$, which is taken to be the arithmetic average of $\langle \tau_w \rangle$ for each of the four duct walls. The effect of curvature becomes more evident as the inner wall shear stress is, in general, greater than the outer wall shear stress. The shear stress magnitude is almost entirely due to the axial component. The inner wall profile exhibits two maxima while three

are noticed for the outer wall. However, the lack of symmetry in the outer wall profile may be another indication that the flow was not integrated long enough. As discussed in the work of Pinelli et al. (2010), the peaks represent the probable position of high velocity streaks. At the duct centre, the stress magnitudes are very similar, what may explain the symmetry found in the $\langle v_z \rangle$ and $\langle v_z' \rangle_{\mathrm{rms}}$ profiles of Fig. 7.4.

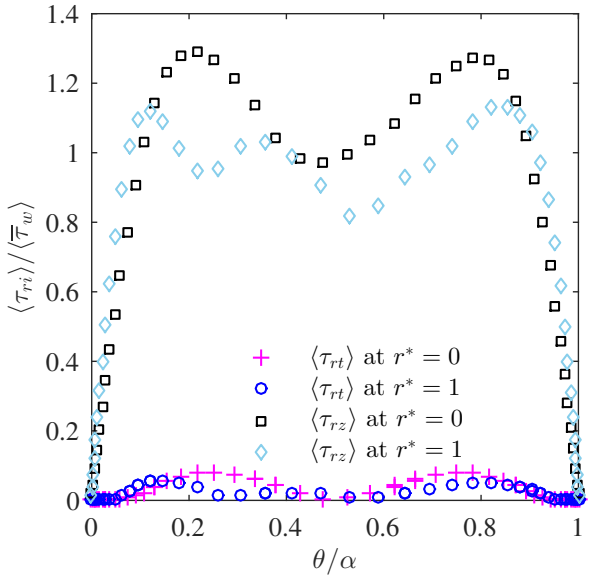


Figure 7.5 – Shear stress distribution along the inner and outer walls normalised by the wall shear stress magnitude.

## 7.3 Rotating duct

The rotation of the reference frame introduces in the governing equations two fictitious entities: the centrifugal and Coriolis forces. The effect of the Coriolis force is to deflect a fluid particle in a direction perpendicular to its instantaneous velocity vector and to the axis of rotation. When viewed from an inertial frame of reference this behaviour is a direct result of the conservation of angular momentum, since a particle moving radially outward tends to spin down, while one moving inward will spin up (DAVIDSON, 2013). The centrifugal force always points radially outward with magnitude (per unit volume) $\rho\omega^2 r$ and unlike the Coriolis force, it is independent of the particle motion.

In order to investigate the effect of rotation in comparison with the stationary case, the duct was put to rotate at a constant speed $\omega$. The grid characteristics and numerical details are given in Tab. 7.3.

Table 7.3 – Numerical details of Case B

| $H^*$ | $R[m]$ | $N_r$,$N_\theta$,$N_z$ | $\Delta r_i^+ (\Delta r_o^+)$ | $\Delta\theta_0^+ (\Delta\theta_\alpha^+)$ | $\delta t[s]$ | $\mathrm{CFL}_{\mathrm{max}}$ | FTT | CPU [hr] |
|---|---|---|---|---|---|---|---|---|
| 4 | 2 | 45, 45, 45 | 0.8187 (0.7511) | 0.7877 (0.8106) | 0.050 | 0.160 | 128 | 63.03 |

Figure 7.6 shows the mean secondary velocity field for cases A and B. The vector magnitudes were normalised by the bulk velocity. The axial axis points inward the page so that rotation direction is clockwise. By comparing Figs. 7.6a and 7.6b, it is seen that the presence of rotation completely alters the flow pattern and increases its strength. While the duct rotates in the clockwise direction, the core vortex

assumes a counterclockwise rotating motion. The octant-organized counter-circulating vortices seen in Fig. 7.6a give place to a Coriolis-induced swirling motion, with a core vortex centred between small and less intense vortices placed near the duct corners. For the present $Re_\omega$, magnitude goes from 2.6% to 10% of the bulk flow.

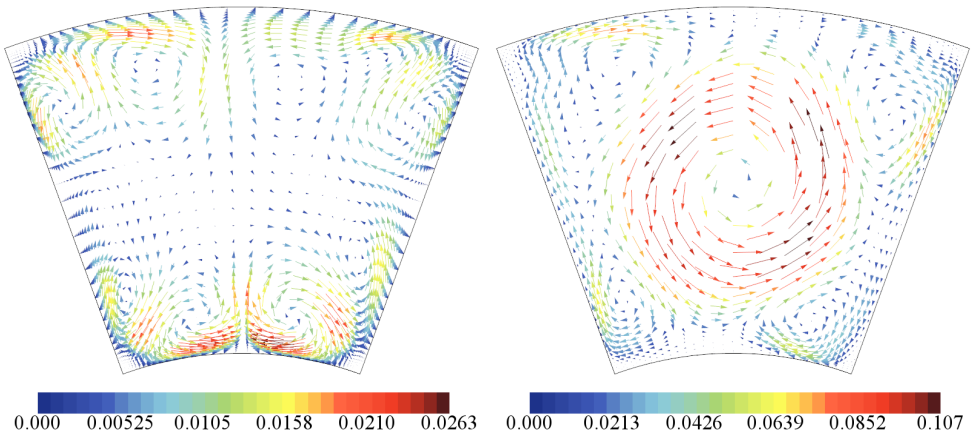


(a) Case A (b) Case B

Figure 7.6 – Mean secondary velocity field normalised by the bulk velocity. (a) Stationary duct case with $Re_b = 5800$ and $\Gamma = 0$. (b) Rotating duct case with $Re_b = 5800$ and $\Gamma = 1$. Rotation direction is clockwise.

The mean streamwise velocity field is compared in Fig. 7.7. The contours are linearly spaced in 16 levels ranging from $0.1 \leq \langle v_z \rangle \leq 1.4$. By comparing both rotating and non-rotating ducts, it is seen that rotation weakens the effect of mean flow momentum convection towards the corners, increasing the velocity magnitude at the duct centre. This can be evidenced by the isolines distribution across the duct cross-section and the value for centre-most isoline. For Case A, the isolines are more concentrated near the walls, flattening the profile at the centre.

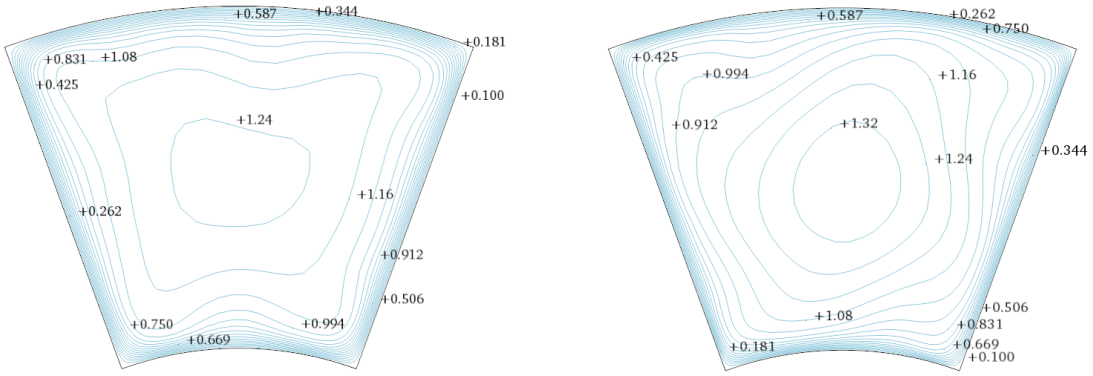


(a) Case A (b) Case B

Figure 7.7 – Mean streamwise velocity field normalised by the bulk velocity. Sixteen contour levels linearly spaced between 0.1-1.4 are shown

The rotation contribution to the wall shear stress magnitude is represented in Tab. 7.4. For Case A, the shear stress magnitude is higher at the inner wall, lower at the outer wall and equivalent at the lateral walls, which agrees with the flow pattern shown in Fig. 7.6a. The introduction of rotation distributes the stress more evenly as seen for Case B. On the other hand, it contributes to an increase of 25% in the friction factor due to the secondary motion effect. The value for $f$ (Eq.6.1) in Case A agrees well with the prediction of Tao et al. (2000) where $f = 0.2685\ Re_b^{-0.25} = 3.078 \times 10^{-2}$.

Table 7.4 – Normalised wall-averaged shear stress magnitude

| | | | $\langle\tau\rangle_w \times 10^3$ | | | | | |
|---|---|---|---|---|---|---|---|---|
| **Case** | $Re_b$ | $\Gamma$ | $r = \eta R$ | $r = R$ | $\theta = 0$ | $\theta = \alpha$ | $\overline{\langle\tau\rangle}_w \times 10^3$ | $f \times 10^2$ |
| **A** | 5800 | 0 | 8.145 | 7.372 | 7.876 | 7.916 | 7.760 | 3.104 |
| **B** | 5800 | 1 | 9.787 | 9.562 | 9.839 | 9.699 | 9.702 | 3.881 |
| **[%]** | | | 20.16 | 29.71 | 24.92 | 22.52 | 25.03 | 25.03 |

The mean radial and tangential velocities for Case B are compared in Fig. 7.8. The profiles were evaluated at $\theta = 0.5\alpha$ and $r^* = 0.5$. As seen in the secondary motion vector field shown in Fig. 7.6b, for $\theta = 0.5\alpha$, the flow is mostly oriented in the $\theta$-direction. The same happens for $r^* = 0.5$ with the flow being mostly oriented in the $r$-direction. The combination of both velocity components creates the circulatory pattern. The inflexions near the walls are confirmations of the presence of counter-rotating vortices. The contribution of the centrifugal force is seen in Fig. 7.8a. The radial velocity is higher in the peaks oriented outwards while no substantial difference is seen for the peaks magnitude on the tangential velocity profile.

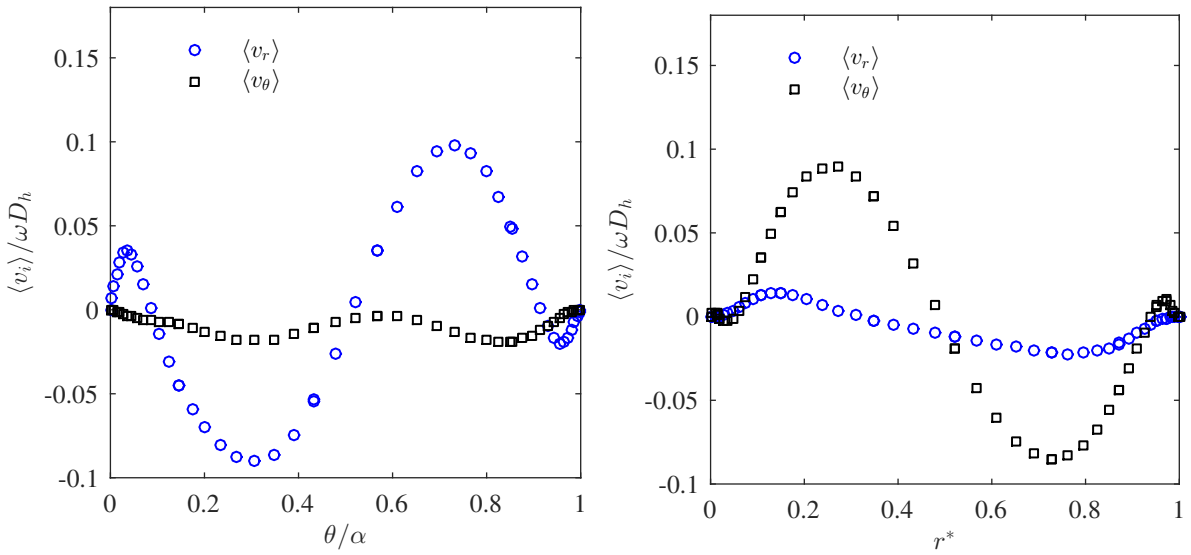


(a) Evaluated at $r^* = 0.5$

(b) Evaluated at $\theta = 0.5\alpha$

Figure 7.8 – Mean radial and tangential velocity distributions along the $r$- and $\theta$- directions evaluated at $\theta = 0.5\alpha$ and $r^* = 0.5$.

The effect of rotation on the time-averaged turbulent kinetic energy is shown in Fig. 7.9. The contour values were normalised by the bulk velocity. For Case A, the turbulent kinetic energy is mainly convected by the axial flow as seen in Fig. 7.9a. When rotating, the volume-average $\langle k\rangle/W_b^2$ goes from $0.888 \times 10^{-2}$

to $1.326 \times 10^{-2}$, representing an increase of almost 50%. The Coriolis-induced vortex possibly contributes to convect turbulent momentum along the duct cross-section as seen in Fig. 7.9b, although it would be necessary to check the turbulent kinetic energy budgets in order to be sure.

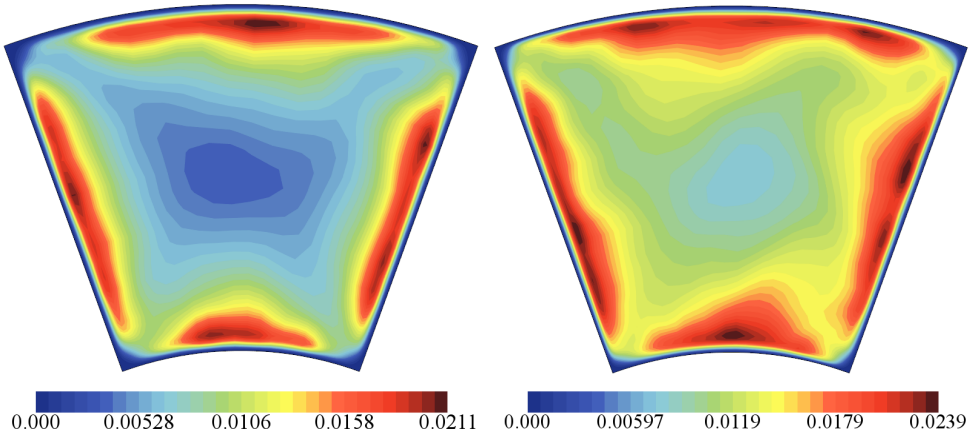


(a) Case A (b) Case B

Figure 7.9 – Contours of the mean turbulent kinetic energy normalised by the bulk velocity $\langle k \rangle / W_b^2$. (a) Stationary duct case. (b) Rotating duct case.

Figure 7.10 confirms the aforementioned effect of rotation on the turbulent quantities. Radial distributions of the Reynolds stress tensor normal components for cases A and B are compared. Every component is increased in the presence of rotation. The effect of curvature seen on $\langle v_r' \rangle_{\mathrm{rms}}$ and $\langle v_\theta' \rangle_{\mathrm{rms}}$ is diminished and $\langle v_z' \rangle_{\mathrm{rms}}$ increases at the centre as a result of the secondary motion.

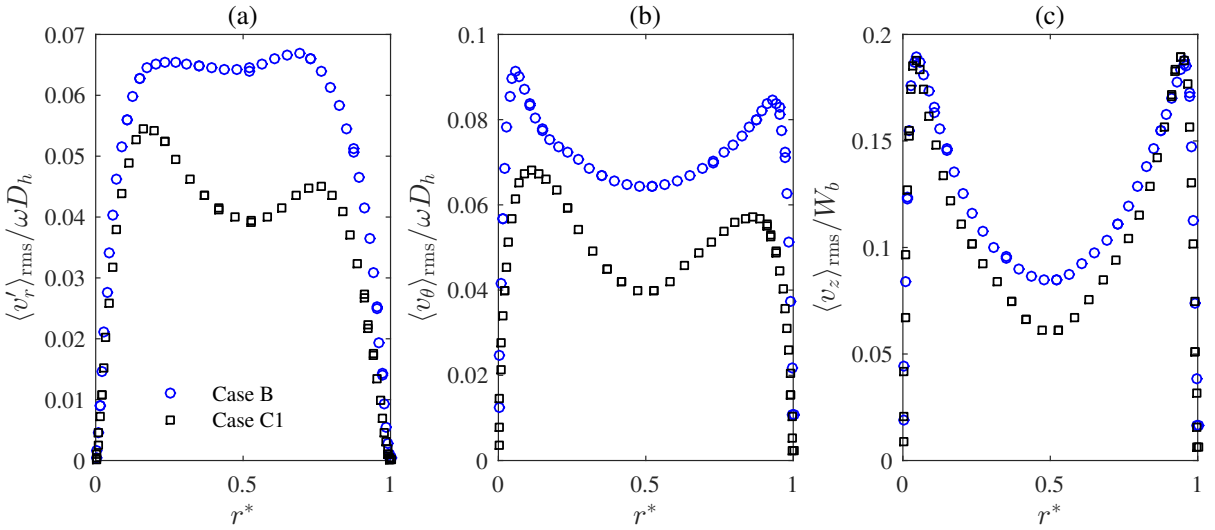


Figure 7.10 – Root mean square of the radial, tangential and axial velocity fluctuations evaluated at $\theta = 0.5\alpha$. Comparison between cases B and A. (a) RMS of radial velocity fluctuation. (b) RMS of tangential velocity fluctuation. (c) RMS of axial velocity fluctuation.

## 7.4 Effect of the stationary outer wall

To analyse the effect of the stationary wall, Case C1 was compared with Case B. The difference between them lies in the boundary condition for the outer wall. Whilst the outer wall rotates with the duct angular speed in Case B, it remains stationary in Case C1.

Considering the duct cross-section, a boundary condition set such as in Case C1 resembles the lid-driven cavity problem. A schematic representation of the flow dynamics is given in Fig. 7.11. The motion within the cavity is maintained by the continuous diffusion of kinetic energy from the moving lid. Besides the centred primary vortex, three secondary recirculating structures form due to the presence of the bounding walls: the downstream, upstream and upper secondary eddies.

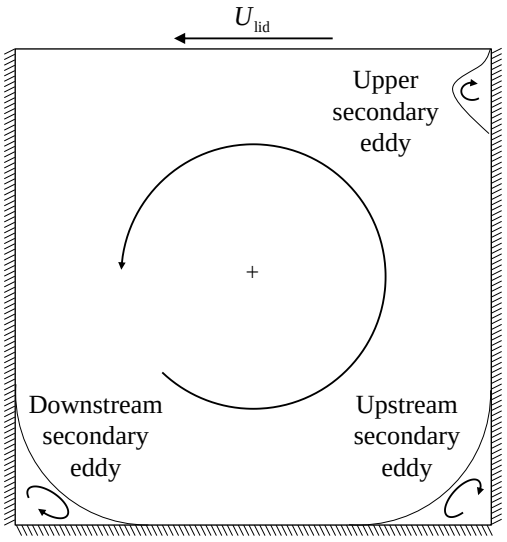


Figure 7.11 – Lid-driven cavity flow schematics. Adapted from Koseff and Street (1984b).

In the present scenario, the secondary motion is driven by rotation, with or without the contribution of the outer wall, and the lid (outer-wall) remains stationary.

The mean secondary field normalised by the bulk velocity is shown in Fig. 7.12. In Fig. 7.12a, the flow in the vicinities of the walls is preferably oriented clockwise, in opposition to the Coriolis-induced swirl. The shear-induced motion from the stationary wall, however, contributes to the swirling motion as shown in Fig. 7.12b. The mean secondary motion maximum intensity is increased from 10% to almost twice that of the bulk flow, as seen in the colour bar in Fig. 7.12b.

The centred primary vortex grows to the size of the duct cross-section as the same pattern found for the lid-driven cavity problem forms (KOSEFF; STREET, 1984a). In Fig. 7.12b, the three recirculation structures known as downstream, upstream and upper secondary eddies are clearly noticed. The shear stress magnitude at the outer ($r = R$) and $\theta = \alpha$ walls is substantially increased, driving the friction factor from $f = 3.881 \times 10^{-2}$ to $f = 16.101 \times 10^{-2}$.

The mean velocity profiles for both cases are shown in Fig. 7.13. The $\langle v_r \rangle$ profile was evaluated at $r^* = 0.5$. The remaining profiles were evaluated at $\theta = 0.5\alpha$. Every curve was averaged along the

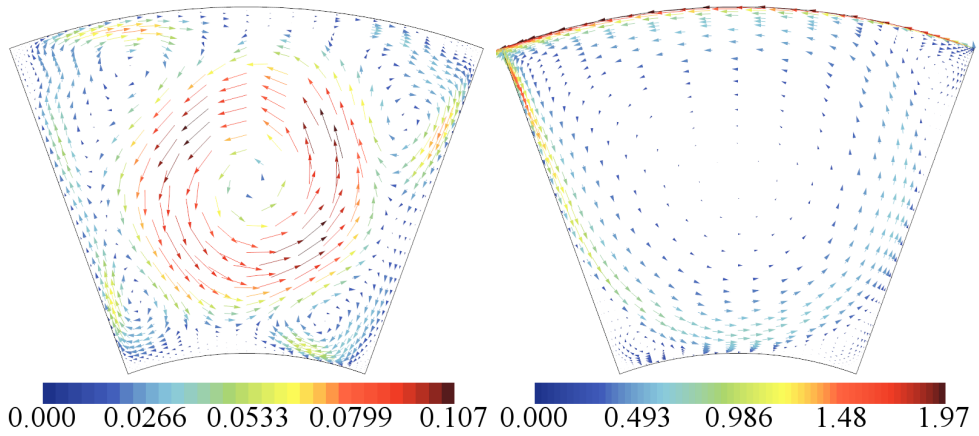


(a) Case B (b) Case C1

Figure 7.12 – Mean secondary velocity field normalised by the bulk velocity.

streamwise direction. The $\langle v_r \rangle$ and $\langle v_\theta \rangle$ profiles for Case C1 are the typical profiles found for the square cavity at the symmetry planes. The radial velocity peak at the downstream wall corresponds to the downstream jet. Both downstream and upstream velocity peaks mark the viscous boundary layer. The secondary motion is completely altered both in shape and magnitude due to the new boundary condition. The mean axial velocity profile is slightly tilted towards the outer wall and the gradient in this region becomes steeper. The maximum axial velocity magnitude is not affected.

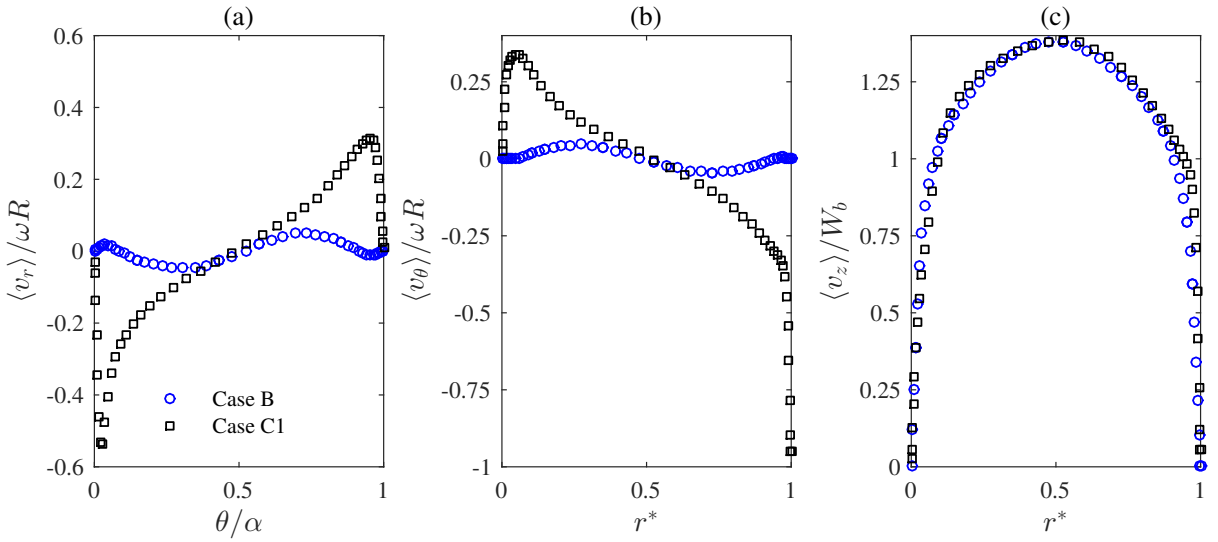


Figure 7.13 – Effect of the stationary wall on the mean velocity profiles. (a) Mean radial velocity evaluated at $r^* = 0.5$. (b) Mean tangential velocity and (c) mean axial velocity evaluated at $\theta = 0.5\alpha$.

The counter-rotating wall effect on the normal components of the Reynolds stress tensor is shown in Fig. 7.14. The double peaks are evident for every profile suggesting that stronger velocity fluctuations are concentrated near the walls. Both radial and tangential components are dramatically changed. The radial distribution for the three components becomes qualitatively similar, with higher intensities near the inner wall. The symmetry for the axial velocity fluctuation is lost as the outer wall peak is lessened. The inner

peak is substantially higher than the outer one, indicating that the most energetic turbulence occurs near the inner wall.

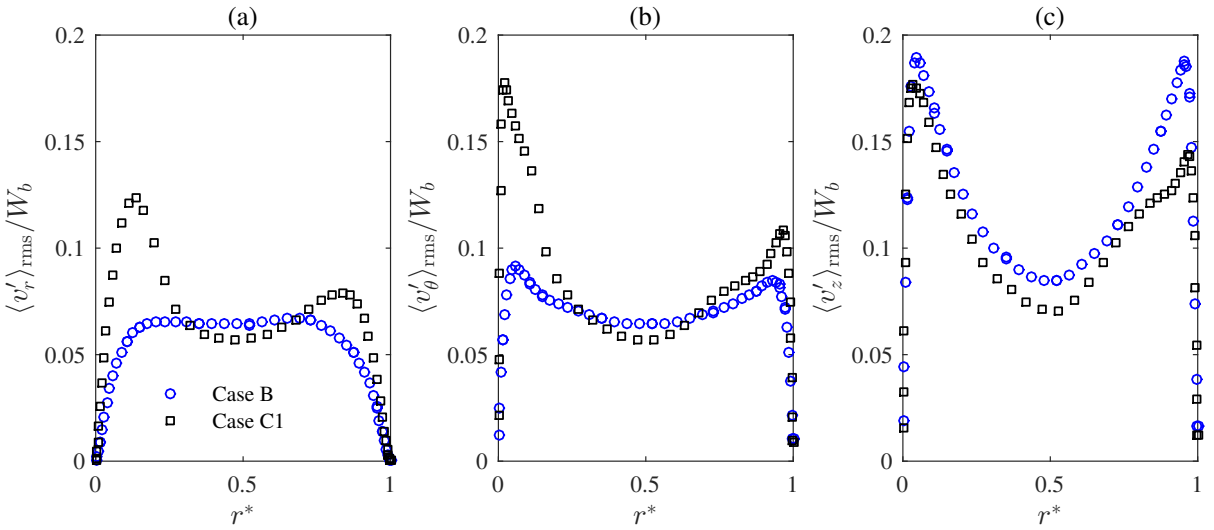


Figure 7.14 – Root mean square of the (a) radial, (b) tangential and (c) axial velocity fluctuations evaluated at $\theta = 0.5\alpha$. Comparison between cases C1 and B.

## 7.5 Effect of the swirl parameter $\Gamma$

This section presents the effect of $Re_\omega$ magnitude on the mean flow dynamics and turbulent quantities. The axial Reynolds number $Re_b$ is kept constant and the magnitude of $Re_\omega$ is dictated by the value of the swirl parameter $\Gamma$, for which details are found in Tab. 7.1. The cases related to this section are referred to as C1, C2 and C3.

It is usual, when dealing with the lid-driven problem, to normalise quantities by the lid speed. Therefore, although the $Re_\omega$ has been defined in terms of the hydraulic diameter, the normalisation of the $r$- and $\theta$-oriented quantities was conducted in terms of $\omega R$. For the $z$-oriented quantities, the flow bulk velocity $W_b$ was used as normalisation parameter.

The details concerning the geometric and grid characteristics are summarised in Tab. 7.5.

Table 7.5 – Numerical details of Group C

| | $\Gamma$ | $H^*$ | $R[m]$ | $N_r$,$N_\theta$,$N_z$ | $\Delta r_i^+(\Delta r_o^+)$ | $\Delta\theta_0^+(\Delta\theta_\alpha^+)$ | $\delta t[s]$ | $\text{CFL}_{\text{max}}$ | FTT | CPU [hr] |
|---|---|---|---|---|---|---|---|---|---|---|
| **C1** | 1 | 10 | 2 | 45, 45, 117 | 0.4464 (0.9696) | 0.6644 (0.4828) | 0.010 | 0.6456 | 18.6 | 330.52 |
| **C2** | 5 | 4 | 2 | 101, 101, 64 | 0.3115 (0.7777) | 0.5721 (0.2527) | 0.005 | 6.434 | 11.40 | 290.29 |
| **C3** | 10 | 2 | 2 | 121, 121, 41 | 0.4434 (0.9659) | 0.6714 (0.4828) | 0.010 | 0.652 | 16 | 785.56 |

Increasing $\Gamma$ allows the duct height $H = h/D_h$ to be reduced as described in Tab. 7.5, saving a great amount of CPU time. For security, two-point correlation functions were evaluated for every case and as illustrated in Fig. 7.15, $\langle R_{uu} \rangle$ falls to zero before the maximum streamwise separation. Here, $R$ refers to the correlation function, not to be mistaken with the Reynolds stress-tensor components.

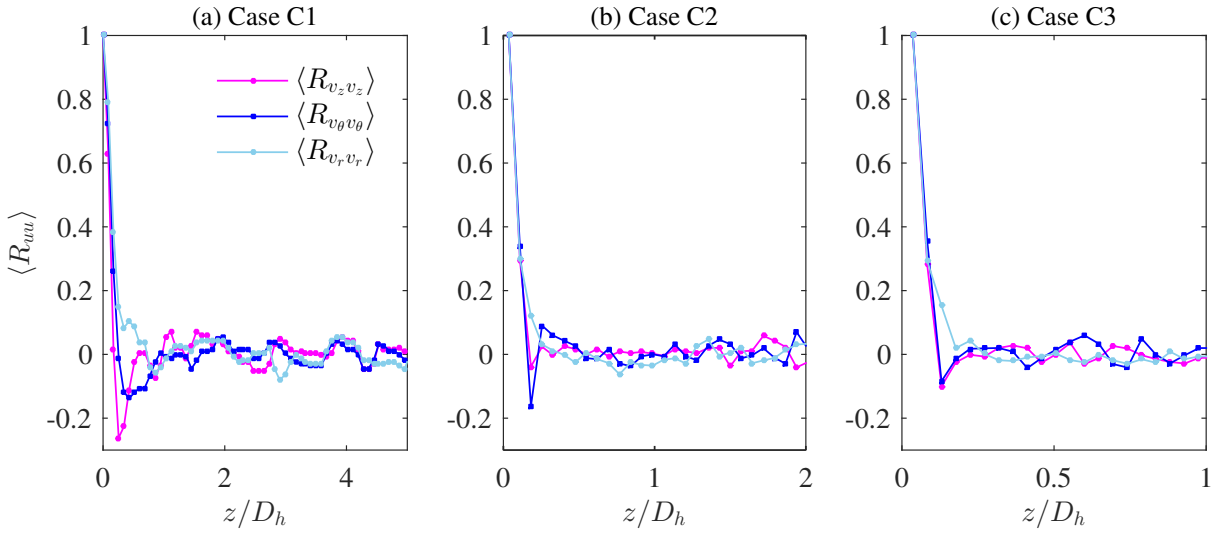


Figure 7.15 – Two-points correlation functions evaluated at $r^* = 0.05$. (a) Case C1. (b) Case C2. (c) Case C3.

### 7.5.1 Mean flow

The effect of $\Gamma$ on the radial and tangential distributions of the mean axial velocity $\langle v_z \rangle$ is shown in Fig. 7.16a and 7.16b, respectively. As $\Gamma$ increases, the axial velocity profiles tend to a laminar shape in the bulk region.

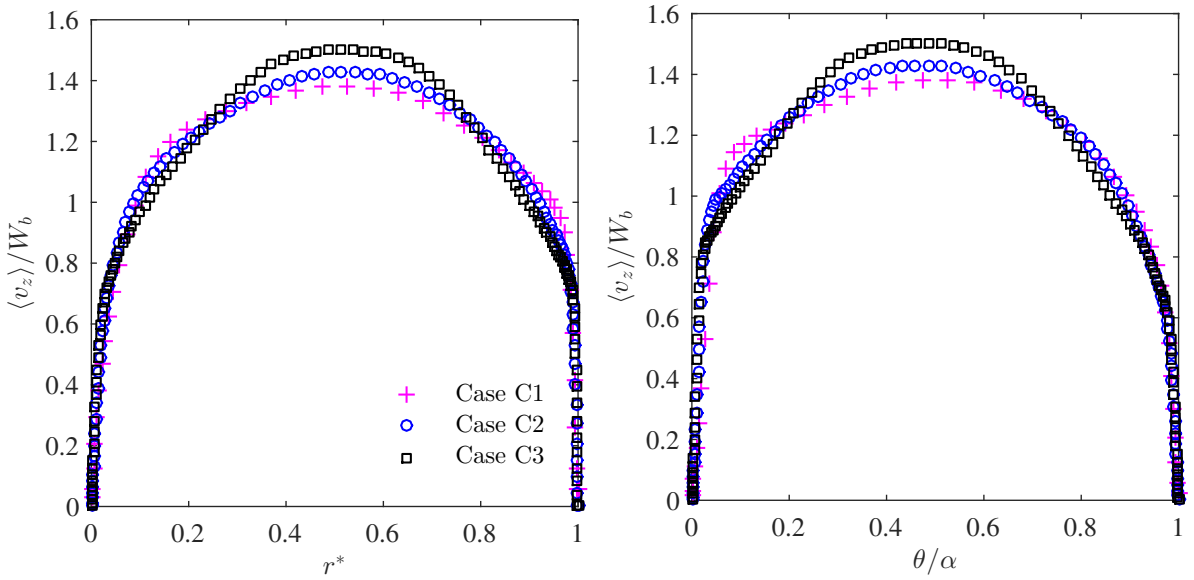


(a) Mean axial velocity profile evaluated at $\theta = 0.5\alpha$

(b) Mean axial velocity profile evaluated at $r^* = 0.5$

Figure 7.16 – Radial and tangential distributions of the mean axial velocity normalised by the bulk velocity.

This effect is better visualised in Fig. 7.17, in which the contours of the mean axial velocity are shown for cases C1, C2 and C3. The streamwise and spanwise motions are highly coupled as it can be seen by the substantial change in the axial velocity distribution. For Case C1, in Fig. 7.17a, the axial velocity profile is skewed towards the outer-left corner. As $\Gamma$ is increased, the axial profile skewness is reduced

as it tends to a more symmetrical arrangement with smoother gradients. The increase in the maximum axial velocity is also evidenced in the colour bars. The maximum velocity position, however, seems to be independent of $\Gamma$ as schematically illustrated in Fig. 7.18. The maximum coordinates were obtained by solving $\partial\langle v_z\rangle/\partial r = \partial\langle v_z\rangle/\partial\theta = 0$.

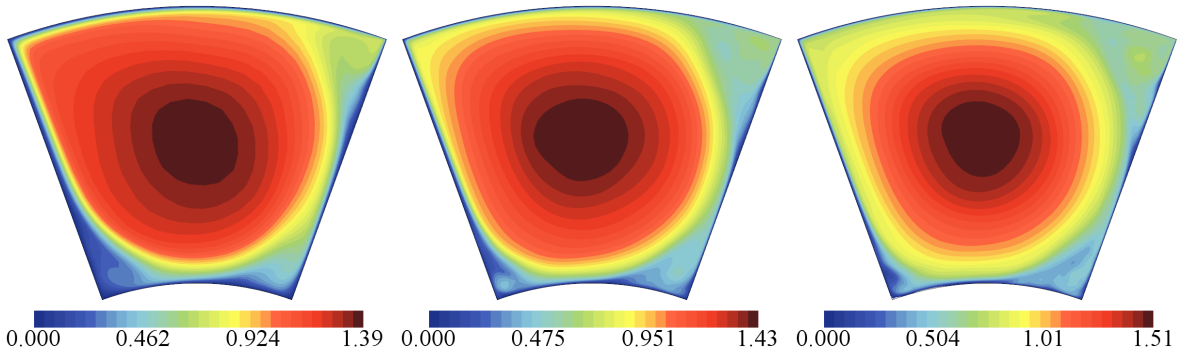


(a) Case C1 (b) Case C2 (c) Case C3

Figure 7.17 – Contours of the mean axial velocity normalised by the bulk velocity. 32 levels are shown.

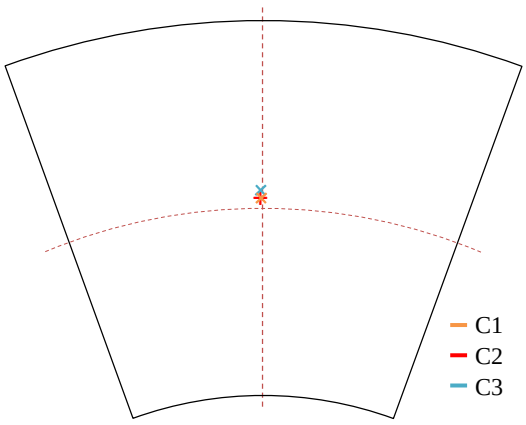


Figure 7.18 – Schematic representation of the maximum axial velocity position as a function of $\Gamma$. The dashed lines represent $r^* = 0.5$ and $\theta = 0.5\alpha$.

The mean azimuthal velocity components distribution along the $r$- and $\theta$-direction is shown in Fig. 7.19. The profiles for the tangential and radial components were evaluated at $\theta = 0.5\alpha$ and $r^* = 0.5$, respectively. The curves were normalised by $\omega R$. The experimental results of Prasad and Koseff (1989) for a square lid-driven cavity at $Re = 10000$ (based on the lid speed and cavity length) are also displayed. The resemblance of the profiles indicates that both configurations exhibit some similarities. The difference found for the gradients at the bulk region may be a manifestation of the curvature and/or rotation effects. Increasing $\Gamma$ makes the boundary layers thinner which can be verified as the velocity profiles are shifted toward the walls in Fig. 7.19a and b.

Figure 7.20 displays the line integral convolution of the secondary velocity field as a function of $Re_\omega$. The fluid in contact with the outer wall is accelerated along the downstream wall. The flow then separates from the wall creating the so-called downstream secondary eddy (DSE). On its way toward the

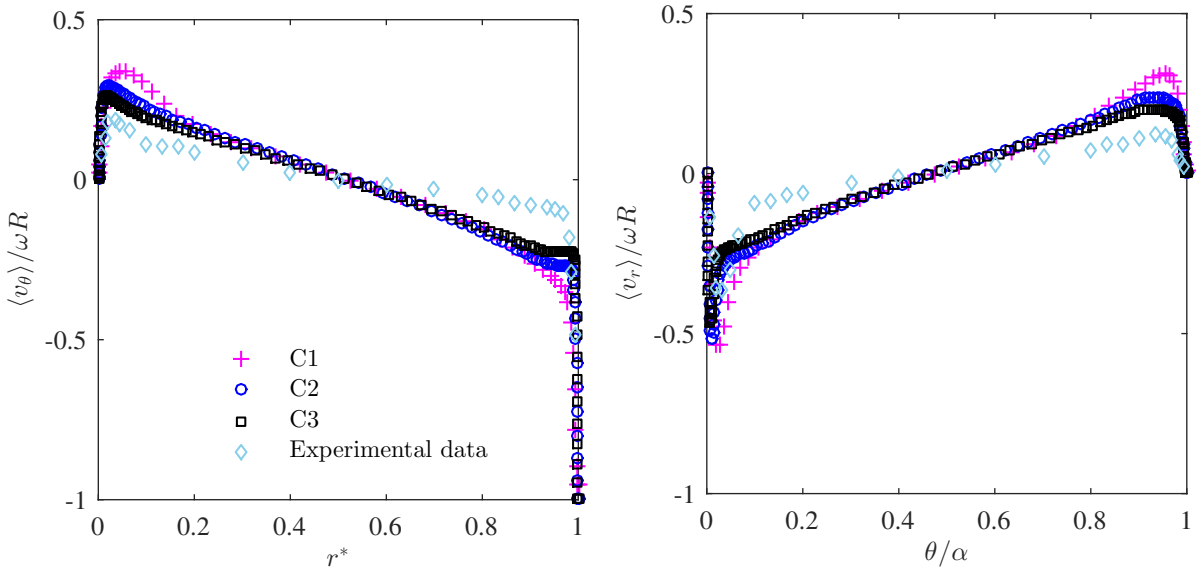


(a) Mean tangential velocity profile evaluated at $\theta = 0.5\alpha$

(b) Mean radial velocity profile evaluated at $r^* = 0.5$

Figure 7.19 – Radial distribution of the mean tangential velocity and tangential distribution of the mean radial velocity. Both profiles were normalised by $\omega R$. The square markers represent the experimental data of Prasad and Koseff (1989) for a square lid-driven cavity flow at $Re = 10000$.

upstream wall, the core circulating structure creates another structure called upstream secondary eddy (USE). Before reaching the outer wall it separates again and the upper eddy (UE) is also formed.

The influence of $Re_\omega$ on this configuration of the secondary motion happens in the same manner as found for square cavities. In the study of Koseff and Street (1984b), for a cavity with 1:1 aspect ratio, the DSE size is reduced as the lid speed is increased. The same tendency is seen in Fig. 7.20. As $Re_\omega$ is increased, the point of separation is shifted inwards, reducing the size of the DSE. This happens as a direct result of the jet velocity along the downstream wall. The more the velocity the more inertia, making it difficult to accelerate the fluid in the $\theta$-direction. The size of the USE, on the other hand, is apparently independent of $Re_\omega$, within the tested range.

The swirl parameter effect on the friction factor is represented in Fig. 7.21. The value found in the absence of rotation is represented by the dashed line. Since $f$ is normalised by the streamwise dynamic pressure, its value is expected to depart from the the dashed line as $\Gamma$ increases. Assuming that the friction factor may be represented as the sum of the streamwise and secondary motion contributions, that is:

$$f = C_1 Re_b^{-0.25} + C_2 \Gamma^n \tag{7.3}$$

and making use of the correlation proposed by Tao et al. (2000), a power-law expression for $f$ that fits the results for cases C1, C2 and C3 may be written as:

$$f = 0.2685 Re_b^{-0.25} + 0.13 \Gamma^{1.52}. \tag{7.4}$$

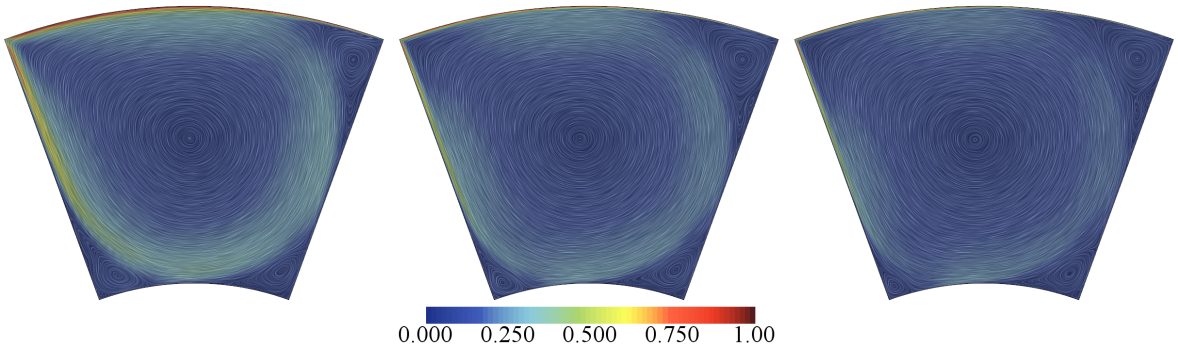


(a) Case C1 (b) Case C2 (c) Case C3

Figure 7.20 – Effect of $\Gamma$ on the secondary motion. Line integral convolution of the secondary field is shown. Colour bands represent the field magnitude normalised by $\omega R$. 32 levels are shown. (a) Case C1 with $\Gamma = 1$. (b) Case C2 with $\Gamma = 5$. (c) Case C3 with $\Gamma = 10$.

When $\Gamma = 0$, Eq. 7.4 returns the value found for Case A. The average deviation for the proposed correlation is 1.65%.

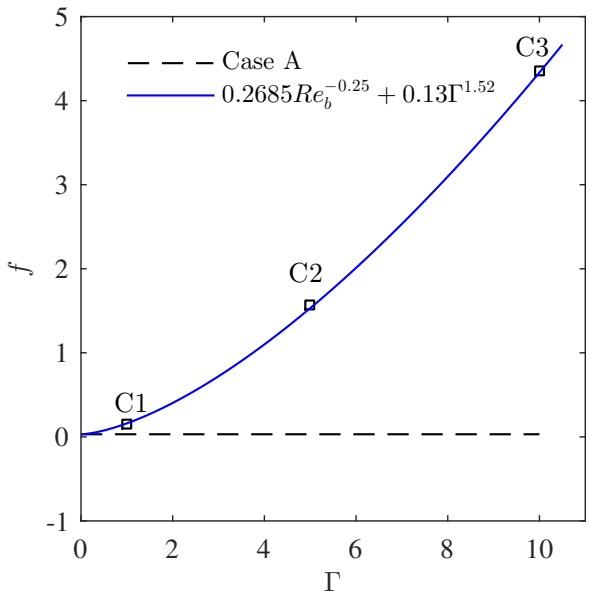


Figure 7.21 – Effect of the swirl parameter $\Gamma$ on the friction factor $f$. The dashed line represents the friction factor obtained for Case A.

For case C3, an interesting feature develops as the flow is curved as it passes along the DSE. The flow over concave surfaces may cause transverse vortices to form, the so called Taylor-Göertler-like (TGL) vortices. In Fig. 7.22, the line integral convolution of the instantaneous velocity field is shown on a plane located at $\theta = 0.05\alpha$. The curvature experienced by the flow when passing over the DSE results in the formation of TGL structures.

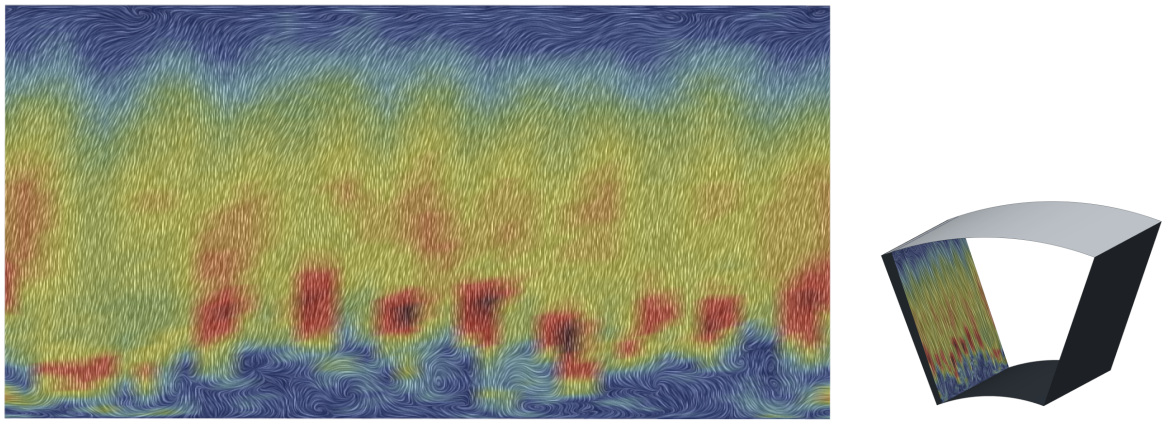

Figure 7.22 – Line integral convolution of the instantaneous velocity field of Case C3 evaluated at $\theta = 0.05\alpha$. Taylor-Göertler-like vortices form close to the downstream wall.

### 7.5.2 Turbulent statistics

The root mean square of the streamwise velocity fluctuations for cases C1, C2 and C3, evaluated at $\theta = 0.5\alpha$ and $r^* = 0.5$ are shown in Fig. 7.23. The profiles were normalised by the flow bulk velocity. The peaks magnitudes are substantially increased but at the bulk region, little influence is perceived. It is possible that, in one way, increasing $\Gamma$ leads to a more turbulent state near the walls but in the other way, the resulting swirling motion stabilises the flow in the bulk region.

In the $r^*$ distribution in Fig. 7.23a, the inner to outer peak difference increases with $\Gamma$, suggesting that the more energetic structures are localised near the inner wall. Although in less pronounced manner, the same trend can be seen for the $\theta$ distribution in Fig. 7.23b. The profiles peak near the walls with higher intensities at the upstream wall.

In Fig. 7.24, the radial distributions of $\langle v'_\theta \rangle_{\mathrm{rms}}$ and $\langle v'_r \rangle_{\mathrm{rms}}$ along $\theta = 0.5\alpha$ are compared with the experimental results of Prasad and Koseff (1989) for the lid-driven square cavity flow. The results for the annular-sector are in qualitative agreement with those of the square cavity. The higher intensities for $\langle v'_\theta \rangle_{\mathrm{rms}}$ and $\langle v'_r \rangle_{\mathrm{rms}}$ are localised near the inner wall. It is intriguing that for cases C2 and C3, the profiles seem to scale with $\omega R$ while they do not for Case C1. Another characteristic that manifests only for cases C2 and C3, in the $\langle v'_\theta \rangle_{\mathrm{rms}}$ profile, is a double peak close to the outer wall.

The contribution of $\Gamma$ for the mean turbulent kinetic energy is displayed in Fig. 7.25. In order to confirm the tendency to laminarisation as $\Gamma$ increases, the contours of $\langle k \rangle$ were normalised by the bulk velocity. In the first place, a very different pattern is seen for Case C1, which may explain the difference in the $\langle v'_\theta \rangle_{\mathrm{rms}}$ and $\langle v'_r \rangle_{\mathrm{rms}}$ profiles in Fig. 7.24. $\langle k \rangle$ increases at the region of the descending jet with inner wall collision but the maximum $\langle k \rangle$ is localised in the USE region. For cases C2 and C3, a very similar pattern develops. As the descending fluid takes longer to separate from the downstream wall, it collides directly on the inner wall. This region then concentrates higher values for $\langle k \rangle$ while the bulk remains mostly laminar. Although the maximum $\langle k \rangle$ for Case C3 is almost two orders of magnitude higher than for Case C1, the $\langle k \rangle$ in the very centre was found to increase by a factor of 2 for Case C2 and a factor of 3.4 for case C3. Therefore, the combined effects of the rotation and stationary wall seems to, somehow, contribute to stabilise the flow within the primary vortex as $\Gamma$ increases.

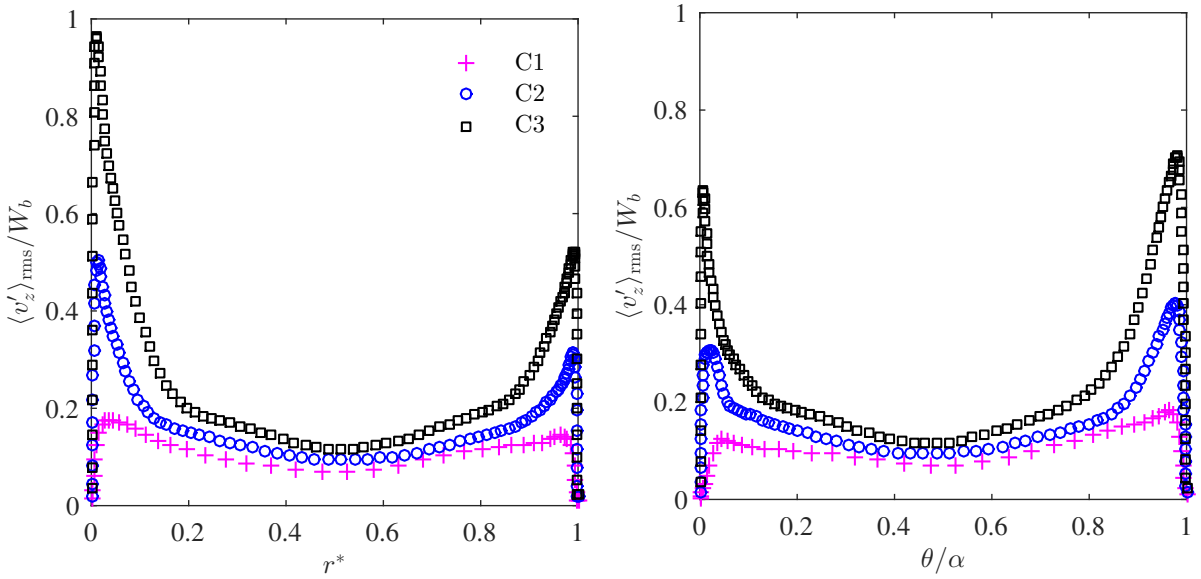


(a) RMS of the axial velocity fluctuation evaluated at $\theta = 0.5\alpha$

(b) RMS of the axial velocity fluctuation evaluated at $r^* = 0.5$

Figure 7.23 – Root mean square of the axial velocity fluctuation as a function of $\Gamma$. The profiles were normalised by $W_b$.

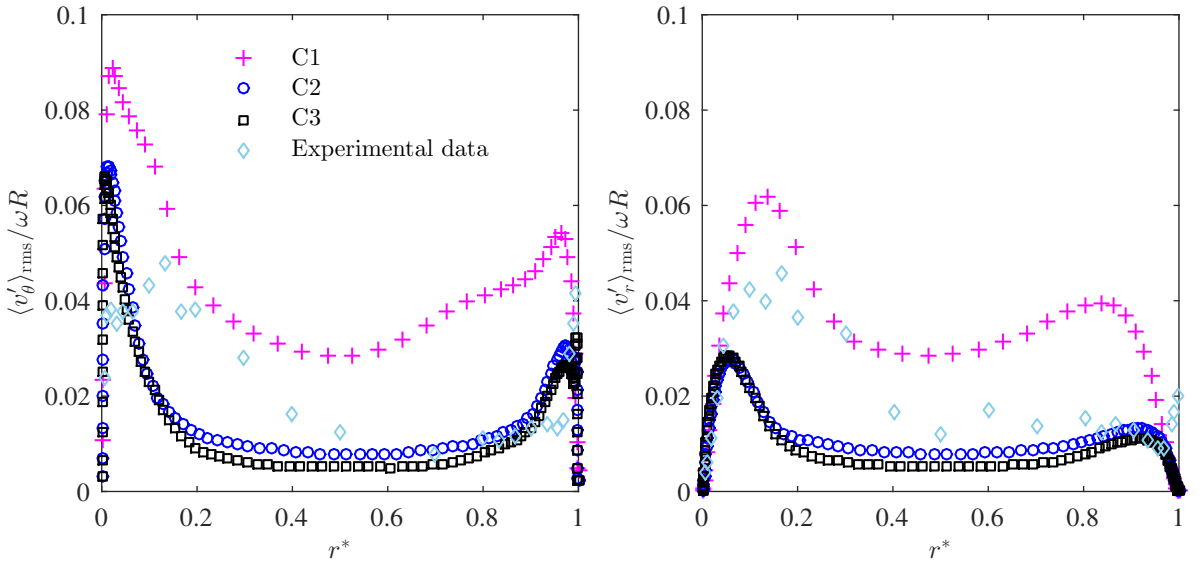


(a) RMS of the tangential velocity fluctuation

(b) RMS of the radial velocity fluctuation

Figure 7.24 – Root mean square of the radial and tangential velocity fluctuations evaluated at $\theta = 0.5\alpha$. Both profiles were normalised by $\omega R$. The square markers represent the experimental data of Prasad and Koseff (1989) for a square lid-driven cavity flow at $Re = 10000$.

The contribution of the Reynolds stress tensor shear components to the total shear is represented in Figs. 7.26 and 7.27, for cases C1 and C3, respectively. The total shear stress tensor, which is defined as:

$$\mathbf{T}^T = \mathbf{T} + \mathbf{R} \tag{7.5}$$

the sum of viscous and turbulent shear stresses. For the present study, the Reynolds stress tensor $\mathbf{R}$ is still

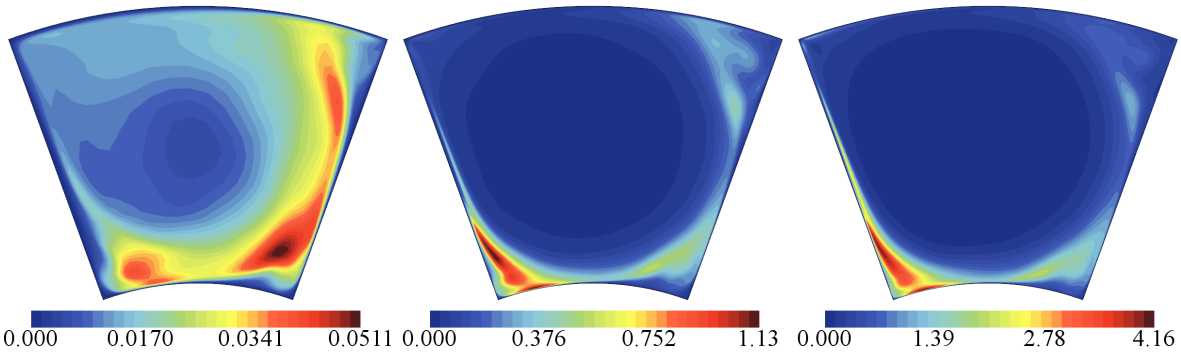


(a) Case C1 (b) Case C2 (c) Case C3

Figure 7.25 – Mean turbulent kinetic energy $\langle k \rangle$ as a function of $\Gamma$. Contours were normalised by $W_b^2$. (a) Case C1 with $\Gamma = 1$. (b) Case C2 with $\Gamma = 5$. (c) Case C3 with $\Gamma = 10$.

subdivided into a resolved and a modelled part, that is:

$$\mathbf{R} = \mathbf{R}^{\text{res}} + \mathbf{T}^{\text{SGS}}. \tag{7.6}$$

The resolved part is obtained directly from Eq. A.37. The unresolved part, modelled according to Eq. 4.17, depends on $\mu_{\text{SGS}}$, which STAR-CCM+ does not provide as a field variable. Therefore, it is worth mentioning that the complete analysis of the turbulent stresses contribution to the total shear stresses would require $\mathbf{T}^{\text{SGS}}$. Nevertheless, great insight can be drawn of the profiles obtained from the resolved part of $\mathbf{R}$.

In Fig. 7.26, the contributions of $\mathbf{R}$ to $\mathbf{T}^T$ for Case C1 are presented. The profiles were normalised by the wall-averaged shear stress magnitude $\langle \overline{\tau}_w \rangle$. In general, the viscous shear dominates within a very slender space, the viscous boundary layers. Beyond this region, the flow may be considered inviscid as the total shear stresses become exclusively related to turbulent phenomena. The higher the $\Gamma$, the more the viscous stresses dominance is confined to the vicinities of the walls. In Fig. 7.27, the viscous part of $\mathbf{T}^T$ is almost indistinguishable.

Figures 7.26a and 7.27a show that in the bulk, shear stress is two-component as $T^T_{r\theta} = 0$. The stabilizing effect of $\Gamma$ through the counter-rotating wall is again evidenced. By comparing Figs. 7.26a and 7.27a, the total shear for Case C3 becomes mostly related to viscous effects. The $T^T_{r\theta}$ component is also responsible for most of the wall shear stress magnitude. From Figs. 7.26b and 7.27b, the turbulent stresses contributions to the total shear stress fall by one order of magnitude. The $\theta z$ distribution, in Figs. 7.26c and 7.27c is completely modified by increasing $\Gamma$. As for the turbulent kinetic energy, which accounts for the normal component of $\mathbf{R}$, the influence of the downstream jet on the way that turbulent stresses are convected by the mean flow, seems to be more significant on the $T^T_{\theta z}$ component of $\mathbf{T}$.

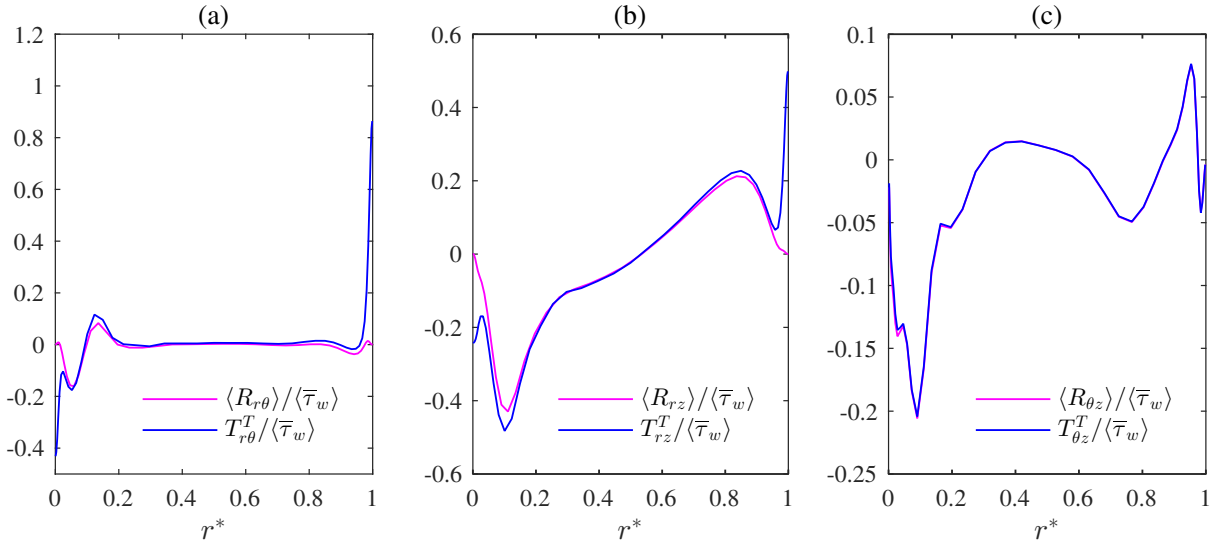


Figure 7.26 – Reynolds shear stress contribution to the total shear stress for C1 evaluated at $\theta = 0.5\alpha$. (a) $R_{r\theta}$-component. (b) $R_{rz}$-component. (c) $R_{\theta z}$-component. The profiles were normalised by the wall-averaged shear stress magnitude.

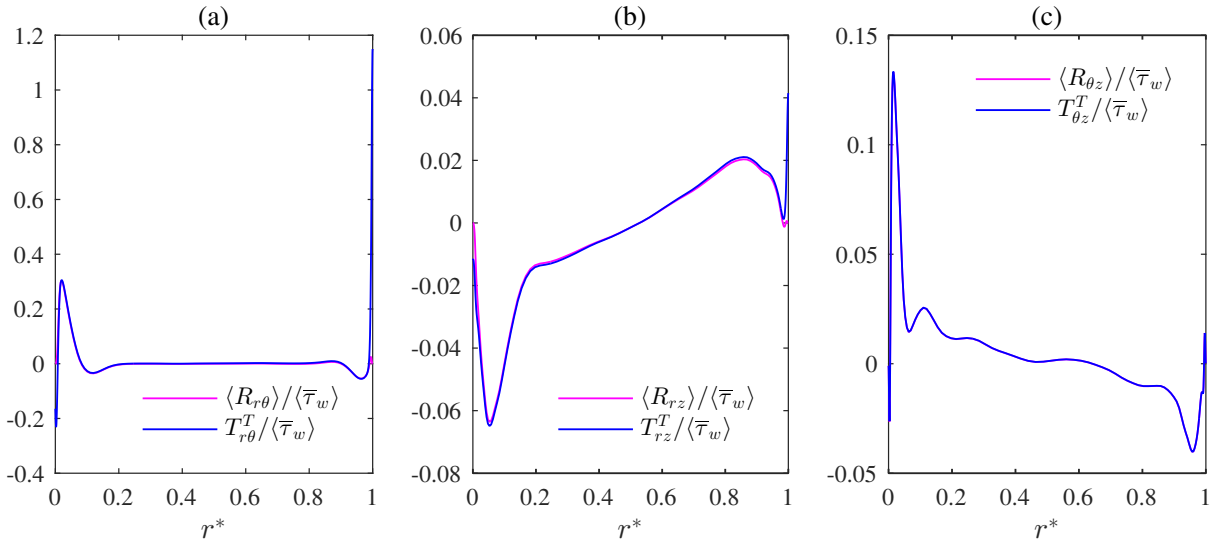


Figure 7.27 – Reynolds shear stress contribution to the total shear stress for C3 evaluated at $\theta = 0.5\alpha$. (a) $R_{r\theta}$-component. (b) $R_{rz}$-component. (c) $R_{\theta z}$-component. The profiles were normalised by the wall-averaged shear stress magnitude.

## 7.6 Effect of the duct apex angle $\alpha$

This section presents the effect of the duct apex angle $\alpha$ on the mean flow dynamics and turbulent quantities. The swirl parameter is kept constant and the value of $\alpha$ is varied according to Tab. 7.1. The cases related to this section are referred to as **D1**, **D2** and **D3**.

The details concerning the geometric and grid characteristics are summarised in Tab. 7.6.

Table 7.6 – Numerical details of Group D

| | $\alpha$ [°] | $H^*$ | $R[m]$ | $N_r$,$N_\theta$,$N_z$ | $\Delta r_i^+(\Delta r_o^+)$ | $\Delta\theta_0^+(\Delta\theta_\alpha^+)$ | $\delta t[s]$ | $\text{CFL}_{\text{max}}$ | FTT | CPU [hr] |
|---|---|---|---|---|---|---|---|---|---|---|
| **D1** | 15 | 5 | 2 | 31, 60, 138 | 0.2163 (0.8771) | 0.3988 (0.2728) | 0.005 | 3.5053 | 14.2 | 157.35 |
| **D2** | 40 | 10 | 2 | 45, 45, 117 | 0.4464 (0.9696) | 0.6644 (0.4828) | 0.010 | 0.6456 | 18.6 | 330.52 |
| **D3** | 75 | 5 | 2 | 61, 35, 50 | 0.5344 (0.8986) | 0.6988 (0.5647) | 0.100 | 2.4801 | 48.1 | 68.47 |

Two-point correlation functions are shown in Fig. 7.28. From the profiles, it is seen that the duct height was chosen appropriately.

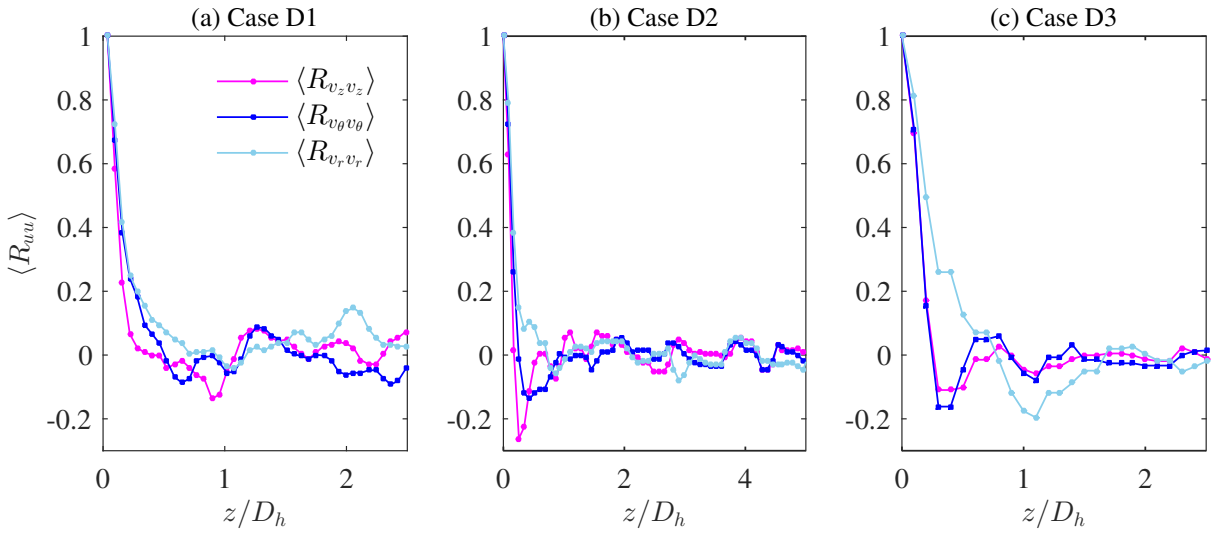


Figure 7.28 – Two-points correlation functions evaluated at $r^* = 0.05$. (a) Case D1. (b) Case D2. (c) Case D3.

### 7.6.1 Mean flow

The effect of $\alpha$ on the radial and tangential distributions of the mean axial velocity $\langle v_z \rangle$ is shown in Fig. 7.29a and 7.29b, respectively. For Case D1, the fluid separates earlier so that the primary vortex occupies the upper half of the duct cross-section. From the D1 profile shown in Fig. 7.29a, two distinct regions are created and limited by the profile inflexion at $r^* \approx 0.3$. The inner region flows more slowly and the flow is almost purely axial (see Fig. 7.31a). The upper region develops the helical pattern resulting from the combination of the axial and circulating motions. A similar phenomenon occurs for Case D3. The axial flow departures from the symmetry plane as two counter-circulating structures develop.

The effect of $\alpha$ can be visualised in Fig. 7.30, in which the contours of the mean axial velocity are shown for cases D1, D2 and D3. In Fig. 7.30a, the preference of the axial flow for the upper part of the

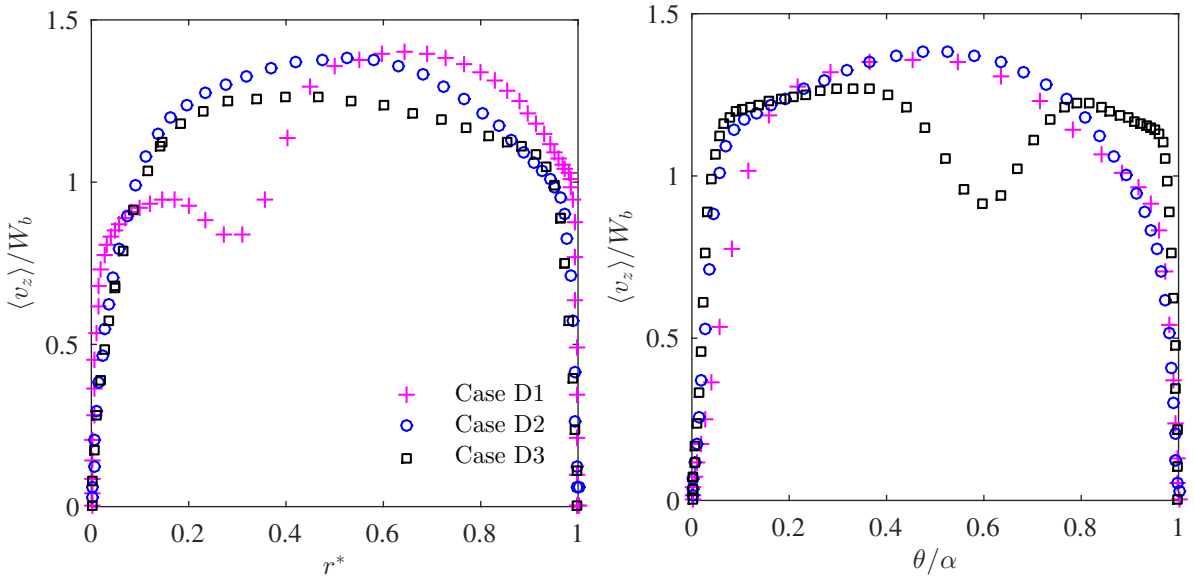


(a) Mean axial velocity profile evaluated at $\theta = 0.5\alpha$ (b) Mean axial velocity profile evaluated at $r^* = 0.5$

Figure 7.29 – Radial and tangential distributions of the mean axial velocity normalised by the bulk velocity.

duct is evidenced. In a process where heat generated by the inner wall must be convected is considered, a flow pattern like the one of Case D1 would be, probably, more ineffective than for other geometric configurations considered in this study. Since the main driving force for the secondary motion is provided by the outer wall, the more fluid in contact with it the higher the strength of the swirling motion within the duct. For Case D3, in Fig. 7.30c, the flow assumes a complex pattern with two separated cores with the left one resembling the pattern developed by D2. In this configuration, the maximum axial velocity is also substantially affected, being lessened in approximately 8%, compared to Case D2.

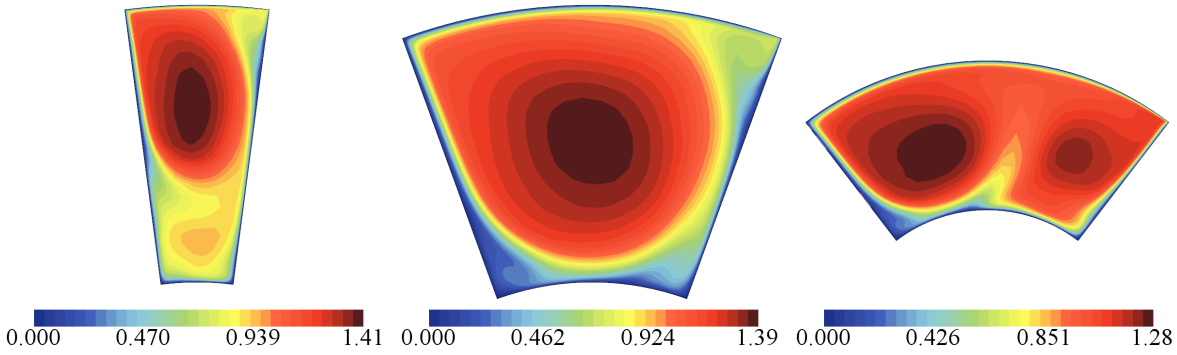


(a) Case D1 (b) Case D2 (c) Case D3

Figure 7.30 – Contours of the mean axial velocity as a function of $\alpha$. The contours were normalised by the bulk velocity. 32 levels are shown. (a) Case D1 with $\alpha = 15°$. (b) Case D2 with $\alpha = 40°$. (c) Case D3 with $\alpha = 75°$.

The profiles for $\langle v_\theta \rangle$ and $\langle v_r \rangle$ respectively evaluated at $\theta = 0.5\alpha$ and $r^* = 0.5$ are shown in Fig. 7.31. The radial distribution of $\langle v_\theta \rangle$ for Case D1, in Fig. 7.31a, matches the expected behaviour seen in Fig.

7.30a. $\langle v_\theta \rangle$ is practically null for $r^* < 0.3$. The primary vortex for D1, in Fig. 7.32a, develops an elliptical shape rather than circular as in the other cases. It causes the velocity gradient in the $r$-direction to be less steep. In Fig. 7.31b, the counter-circulating pattern for Case D3 appears through the profile inflexion at $\theta/\alpha \approx 0.58$. The absence of the upstream wall allows the ascending jet to penetrate through the symmetry plane. This can be elucidated by the deviation of the $\langle v_r \rangle$ profile from the others.

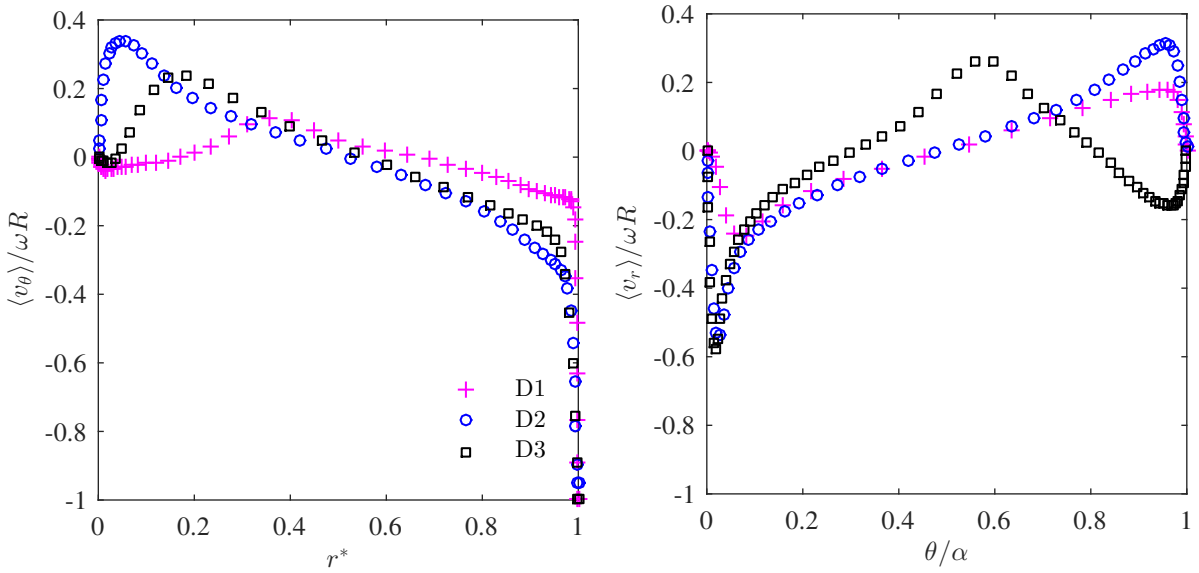


(a) Mean tangential velocity profile evaluated at $\theta = 0.5\alpha$

(b) Mean radial velocity profile evaluated at $r^* = 0.5$

Figure 7.31 – Radial distribution of the mean tangential velocity and tangential distribution of the mean radial velocity for Group D. Both profiles were normalised by $\omega R$.

The effect of $\alpha$ on the secondary motion configuration is illustrated in Fig. 7.32. The line integral convolution of the secondary velocity field, normalised by $\omega R$ is shown. Colour bands represent the velocity magnitude. For Case D1, in Fig. 7.32a, the DSE forms in the inner-right corner, as a result of the global motion of the counter-circulating vortex. The same happens for the USE which is reallocated at the inner-left corner. Compared to cases D2 and D3, the magnitude of the secondary motion is smaller due to the hindering action of the wall stresses. The high velocities become confined close to the outer wall and downstream jet. For case D3, the downstream jet penetrates through the symmetry plane as it separates from the inner wall. The USE is replaced by a primary counter-circulating structure which interacts in a very complex manner with the outer wall boundary layer.

The apex angle influence on the friction factor is represented in Fig. 7.33. The value for the Taylor-Couette-Poiseuille (TCP) problem obtained from a steady RANS solution is also displayed. Increasing the duct apex angle causes a reduction in the friction factor, which tends to the TCP value. This can be explained by the contribution of the outer wall to the total wall shear stress magnitude. Since the friction factor is calculated by averaging the wall shear stress along the duct perimeter, the more the available area the less the stress peaks at the outer wall contribute to the wall total stress. As in the TCP configuration there are no corner, the friction factor for the given $\eta$ is minimum.

It is noteworthy to mention that, in the stationary laminar case, the behaviour of the friction factor is completely different. In the study of Sparrow et al. (1964), the analytical solution of an annular-sector

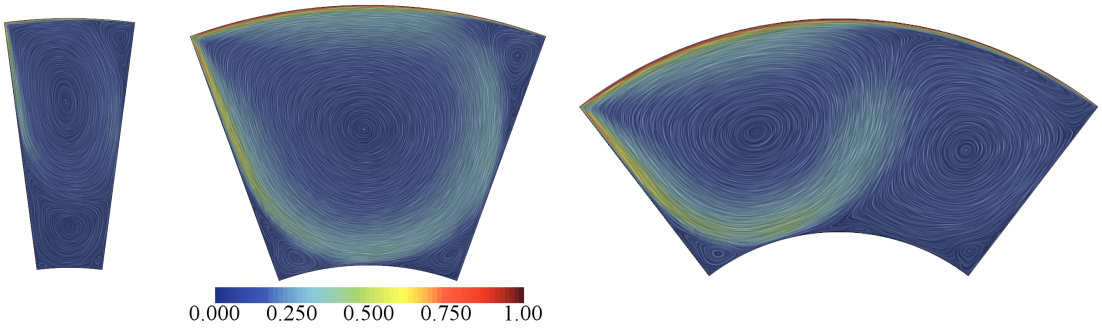


(a) Case D1 (b) Case D2 (c) Case D3

Figure 7.32 – Line integral convolution of the secondary motion. Colour bands represent the field magnitude normalised by $\omega R$. 32 levels are shown. (a) Case D1 with $\alpha = 15°$. (b) Case D2 with $\alpha = 40°$. (c) Case D3 with $\alpha = 75°$.

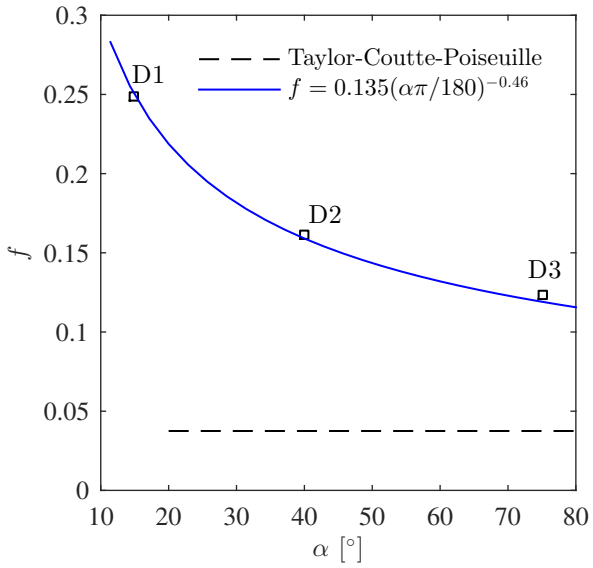


Figure 7.33 – Effect of the duct apex angle $\alpha$ on the friction factor $f$. The dashed line represents the $f$ for the Taylor-Coutte-Poiseuille problem with the same boundary conditions obtained from a steady RANS solution.

is derived for different radius ratios and apex angles. The friction factor does not show a monotonic behaviour with $\alpha$, neither with $\eta$. The same pattern cannot be verified for the present study due to the contributions of rotation and outer wall shear, which outshine the contribution of the pure axial flow.

As done for Group C, a power-law expression may be obtained to characterize the influence of $\alpha$ on the friction factor as follows:

$$f = 0.135 \left( \frac{\alpha\pi}{180} \right)^{-0.46} \tag{7.7}$$

The usage of the relation above is, however, restricted to $\eta = 0.5$ and $\Gamma = 1$. The average deviation for the correlation is 4.01%.

### 7.6.2 Turbulent statistics

Figure 7.34 displays the radial and tangential distributions of the axial velocity fluctuation along $\theta = 0.5\alpha$ and $r^* = 0.5$. The counter-circulating pattern created in cases D1 and D3 alters the distributions seen so far. Apparently, the flow is more unstable at the contact region between the counter-circulating vortices. This can be evidenced by the profiles of $\langle v_z' \rangle_{\mathrm{rms}}$ for cases D1 and D3 peaking near the duct centre.

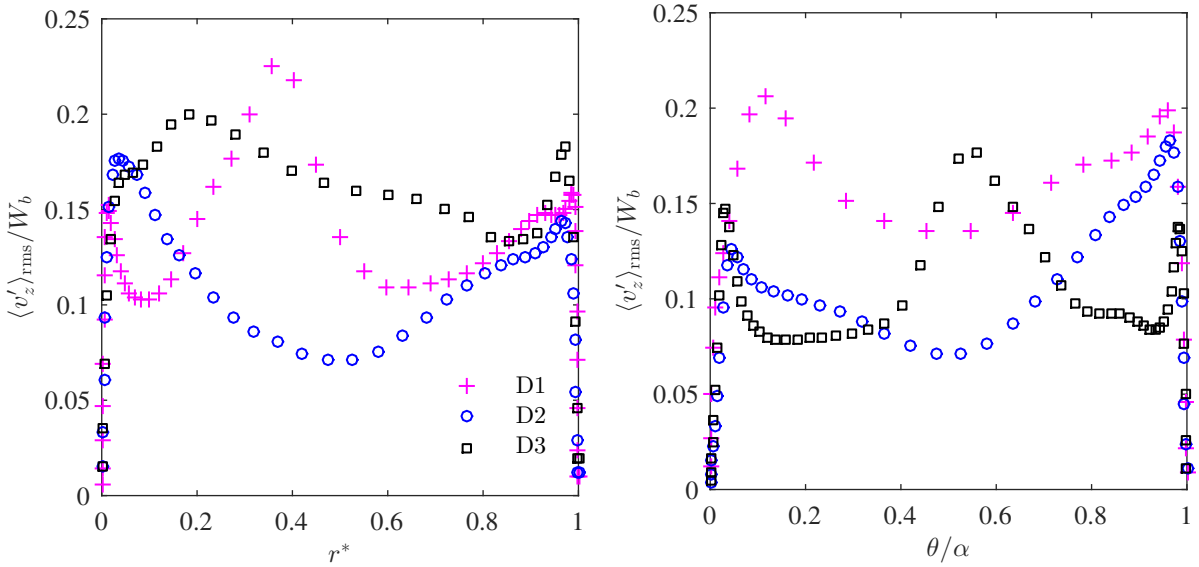


(a) RMS of the axial velocity fluctuation evaluated at $\theta = 0.5\alpha$

(b) RMS of the axial velocity fluctuation evaluated at $r^* = 0.5$

Figure 7.34 – Root mean square of the axial velocity fluctuation. The profiles were normalised by $W_b$.

In Fig. 7.35, the contour plot of the mean turbulent kinetic energy corroborates with the pattern of Fig. 7.34. The contact region between the counter-circulating vortices holds most of the turbulent kinetic energy. For Case D2, however, this region cannot be verified. Comparing every flow configuration shown so far, it can be postulated that the greatest instabilities are somehow related to the downstream jet detachment at some point. For Cases C1(D2) and D3, it happens as the flow separates from the inner wall. For Cases C2, C3 and D1, it happens as the flow separates from the downstream wall.

The radial distribution of $\langle v_\theta' \rangle_{\mathrm{rms}}$ and $\langle v_r' \rangle_{\mathrm{rms}}$ along the geometry symmetry plane are illustrated in Fig. 7.36. The profiles for Case D3 stand out from the others, which is a confirmation that the absence of the wall hindering the ascending jet contributes to turbulence intensification.

## 7.7 Effect of the radius ratio $\eta$

This section presents the effect of the radius ratio $\eta$ on the mean flow dynamics and turbulent quantities. The swirl parameter is kept constant at $\Gamma = 1$ and the value of $\eta$ varies as described in Tab. 7.7. The cases related to this section are referred to as E1, E2 and E3.

The details concerning the geometric and grid characteristics are summarised in Tab. 7.7.

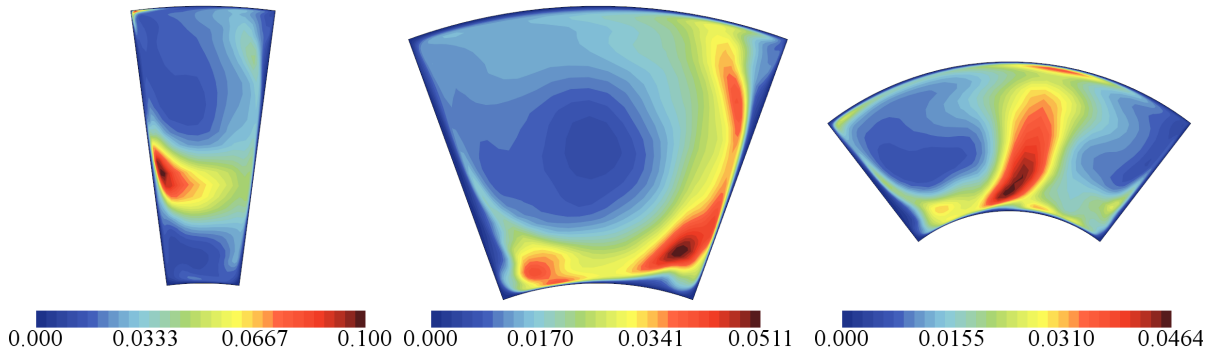


(a) Case D1 (b) Case D2 (c) Case D3

Figure 7.35 – Contours of the mean turbulent kinetic energy $\langle k \rangle$ normalised by $W_b^2$. (a) Case D1 with $\alpha = 15°$. (b) Case D2 with $\alpha = 40°$. (c) Case D3 with $\alpha = 75°$.

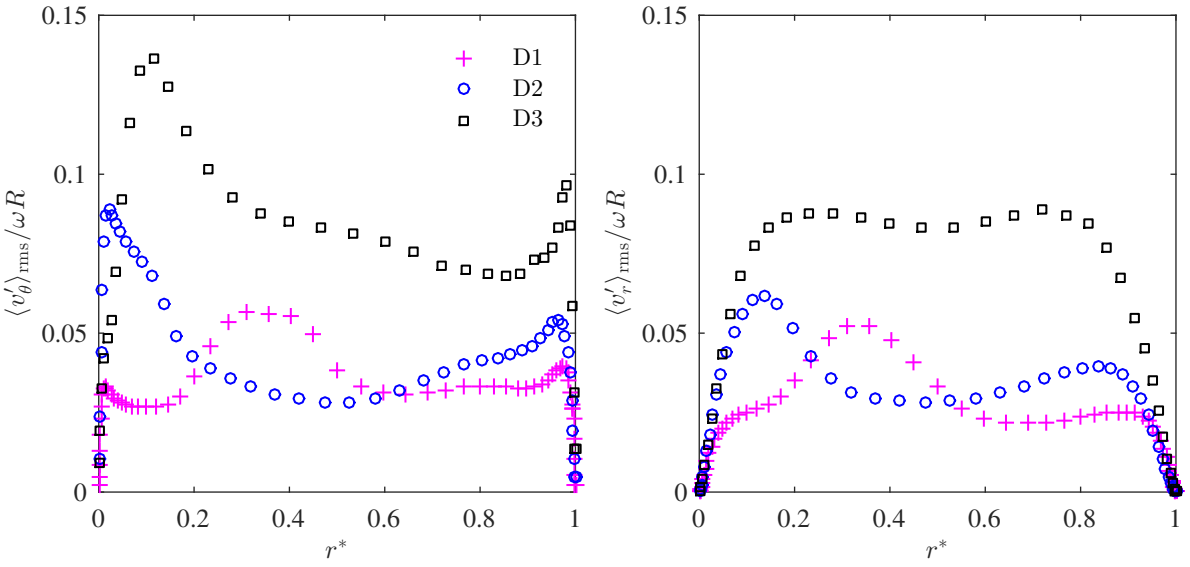


(a) RMS of the tangential velocity fluctuation (b) RMS of the radial velocity fluctuation

Figure 7.36 – Root mean square of the radial and tangential velocity fluctuations evaluated at $\theta = 0.5\alpha$. Both profiles were normalised by $\omega R$.

Table 7.7 – Numerical details of Group E

| | $\eta$ | $H^*$ | $R[m]$ | $N_r$,$N_\theta$,$N_z$ | $\Delta r_i^+(\Delta r_o^+)$ | $\Delta\theta_0^+(\Delta\theta_\alpha^+)$ | $\delta t[s]$ | $\text{CFL}_{\text{max}}$ | FTT | CPU [hr] |
|---|---|---|---|---|---|---|---|---|---|---|
| **E1** | 0.3 | 6.5 | 10 | 35, 41, 64 | 0.3765 (0.8586) | 0.5475 (0.4357) | 0.250 | 0.5531 | 13.11 | 171.85 |
| **E2** | 0.5 | 10 | 2 | 45, 45, 117 | 0.4464 (0.9696) | 0.6644 (0.4828) | 0.010 | 0.6456 | 18.60 | 330.52 |
| **E3** | 0.7 | 3 | 10 | 55, 45, 55 | 0.4042 (0.8427) | 0.6409 (0.3823) | 0.100 | 0.6906 | 25.96 | 252.60 |

Two-point correlation functions are shown in Fig. 7.37. For Case E1, in Fig. 7.37a, the profile behaves strangely what may indicate some incoherence in the numerical setup. The correlation functions fall to zero before the maximum streamwise separation though.

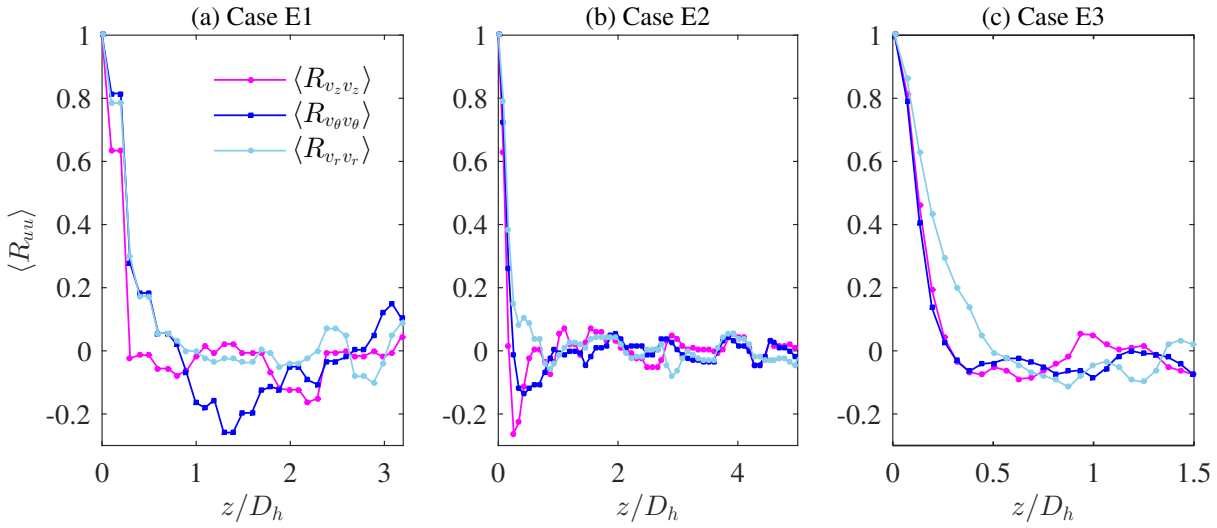


Figure 7.37 – Two-points correlation functions evaluated at $r^* = 0.05$. (a) Case E1. (b) Case E2. (c) Case E3.

### 7.7.1 Mean flow

The effect of $\eta$ on the mean streamwise velocity is represented in Fig. 7.38. The profiles were normalised by $W_b$ and evaluated at $\theta = 0.5\alpha$ and $r^* = 0.5$, in Figs. 7.38a and 7.38b, respectively. The effect of $\eta$ is very similar to that of $\alpha$. For Case E1, the radial distribution shows the same pattern of Case D1, with a slow moving inner core. For Case E3, the tangential distribution reveals two separate cores with a slowing fluid near the geometry symmetry plane.

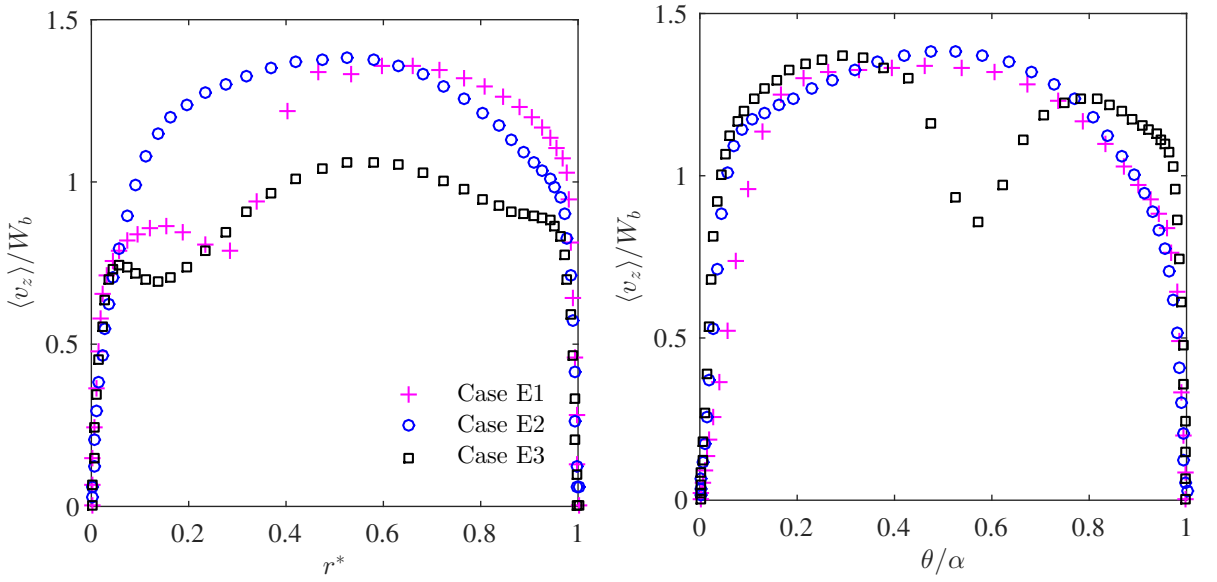


(a) Mean axial velocity profile evaluated at $\theta = 0.5\alpha$

(b) Mean axial velocity profile evaluated at $r^* = 0.5$

Figure 7.38 – Effect of $\eta$ on the radial and tangential distributions of the mean axial velocity. The profiles were normalised by the bulk velocity.

For the tangential velocity distribution, in Fig. 7.39a, Case E1 presents a slight difference when compared with Case D1, from Fig. 7.29a. The secondary motion is more intense for Case E1, which

can be verified by means of the velocity magnitude in the slow moving region and also by the velocity gradient in the primary vortex, which is steeper for Case E1. For Case E3, on the other hand, no substantial difference can be noticed in the profiles for both $\langle v_\theta \rangle$ and $\langle v_r \rangle$ when compared with Case D3.

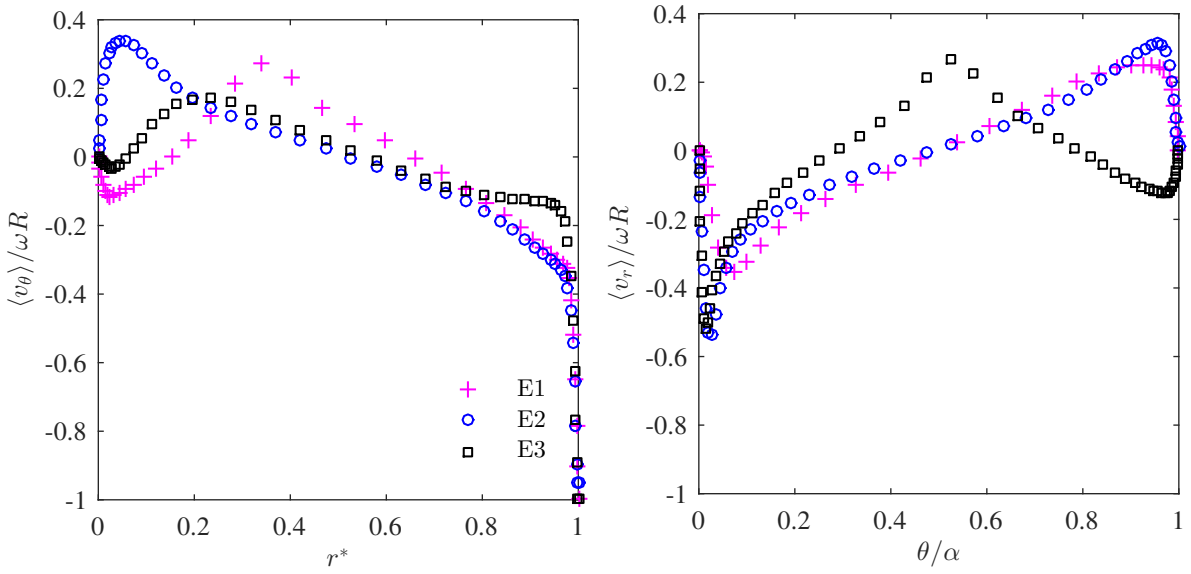


(a) Mean tangential velocity profile evaluated at $\theta = 0.5\alpha$

(b) Mean radial velocity profile evaluated at $r^* = 0.5$

Figure 7.39 – Radial distribution of the mean tangential velocity and tangential distribution of the mean radial velocity. Both profiles were normalised by $\omega R$.

Figure 7.40 compares the velocity distributions for cases D1×E1 and D3×E3. The $\langle v_\theta \rangle$ profiles, in Fig. 7.40a, and $\langle v_r \rangle$ profiles, in Fig. 7.40b, of cases D3 and E3 are indeed similar.

The contour of the axial velocity for Group E are shown in Fig. 7.41. In Fig. 7.41a, a strange distortion in the axial contours points, possibly, to a poor grid resolution. Nevertheless, the velocity distribution and magnitude present a similar pattern to that seen for Case D1. In Fig. 7.41c, the contact region between the counter-circulating cores is better defined but no substantial difference is noted in the distribution as a whole. As seen for group D, the maximum axial velocity is shifted from the duct centre for cases E1 and E3. The $\eta$ influence on its magnitude, however, is less relevant than the effect caused by $\Gamma$, with variations ranging from 1% to 3%.

The resulting secondary motion when $\eta$ is varied is illustrated in Fig. 7.42. The elliptical shape for the primary vortex seen for Case D1 no longer exists for Case E1, in Fig. 7.42a. The available space allows the expected circular shape to establish. Case E3 pattern, in Fig. 7.42c, is practically identical to D3. The main difference lies in the shape and position of the secondary eddy formed in the inner-right corner, which is slightly bigger and tilted toward the vertical wall for Case E3.

Despite the fact that the streamwise and spanwise flow fields are very similar for Groups E and D, the friction factor follows a different behaviour. The $f$ curve is not monotonic as for Group D. Instead, it places Case E2 as the minimum point of $f$ for the investigated configurations. The effect of $\eta$, as represented in Fig. 7.43, is also more significant than the effect of $\alpha$ (see Fig. 7.33). The friction factor for cases E1 and E3 are approximately 3 times higher than for cases D1 and D3.

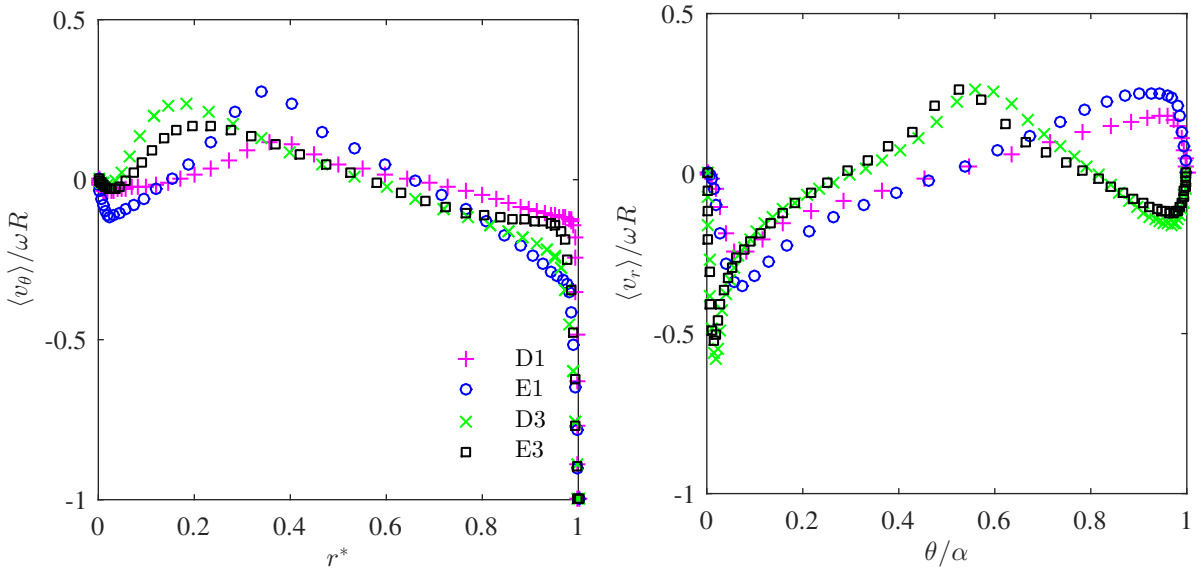


(a) Mean tangential velocity profile evaluated at $\theta = 0.5\alpha$

(b) Mean radial velocity profile evaluated at $r^* = 0.5$

Figure 7.40 – Similarity between cases D1-E1 and D2-E2. (a) Radial distribution of the mean tangential velocity and (b) tangential distribution of the mean radial velocity. Profiles were normalised by $\omega R$.

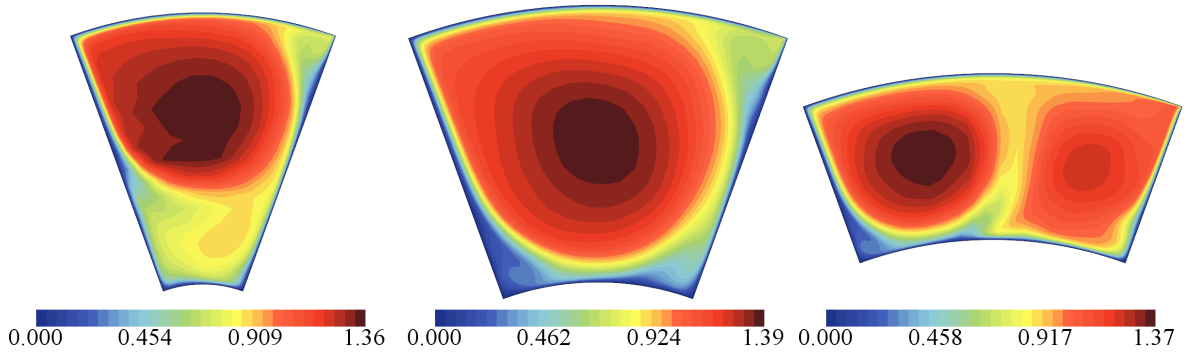


(a) Case E1 (b) Case E2 (c) Case E3

Figure 7.41 – Contours of the mean axial velocity normalised by the bulk velocity. 32 levels are shown. (a) Case E1 with $\eta = 0.3$. (b) Case E2 with $\eta = 0.5$. Case E3 with $\eta = 0.7$.

### 7.7.2 Turbulent statistics

The effect of $\eta$ on the axial velocity fluctuation is represented in Fig. 7.44. As seen for Group D, besides the near wall region, the profiles present peaks in the contact region between the counter-circulating cores. The $\langle v_z \rangle_{\text{rms}}$ distribution for both groups is pretty much the same. The $\eta$ contribution to the magnitude of $\langle v_z \rangle_{\text{rms}}$ is more pronounced for case D1 than for E1. The bad characterisation of the peak for case E1, in Fig. 7.44a, is another indication of poor grid resolution.

The effect of $\eta$ on the radial and tangential normal components of the Reynolds stress tensor, shown in Fig. 7.45, is the opposite of $\alpha$. Using case E2=D2 as base for comparison, increasing $\eta$ shifts both radial and tangential profiles downwards for case E3 while the profiles of case E1 are shifted upwards.

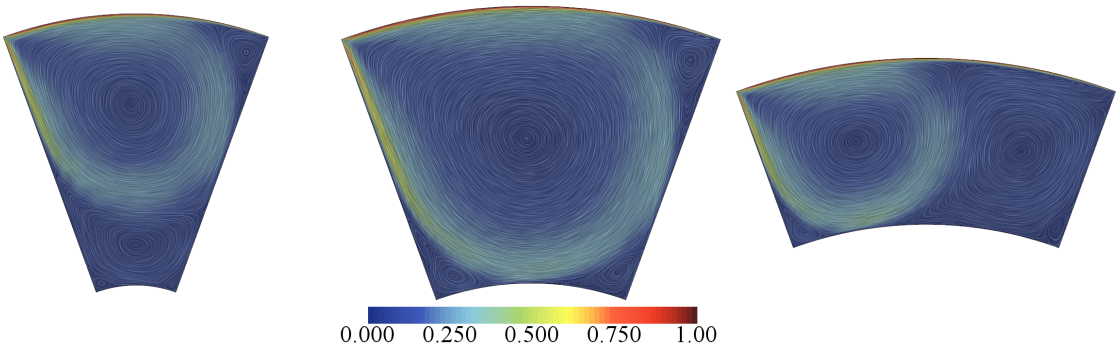


(a) Case E1 (b) Case E2 (c) Case E3

Figure 7.42 – Line integral convolution of the secondary motion. Colour bands represent the field magnitude normalised by $\omega R$. 32 levels are shown. (a) Case E1 with $\eta = 0.3$. (b) Case E2 with $\eta = 0.5$. Case E3 with $\eta = 0.7$.

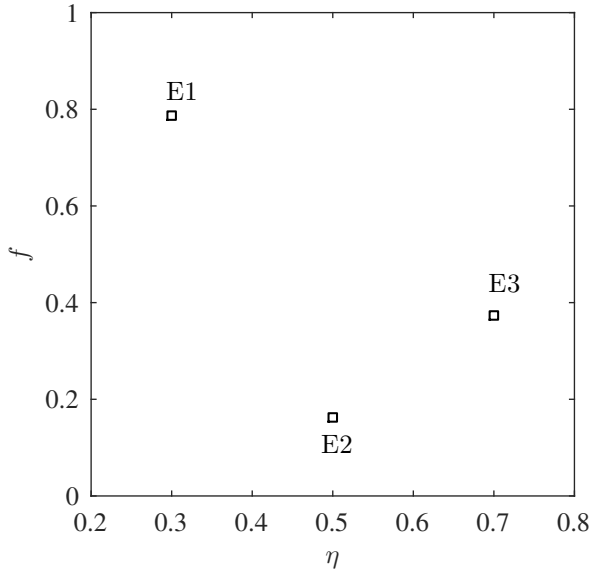


Figure 7.43 – Effect of the radius ratio $\eta$ on the friction factor $f$.

The overall effect of $\eta$ on the turbulent kinetic energy is not as expected. From the contours of $\langle k \rangle$, shown in Fig. 7.46, it is found that the magnitude of $\langle k \rangle$ for Case E1, in Fig. 7.46a, is less than half of Case D1, from Fig. 7.35a. On the other hand, the friction factor is three times higher for Case E1. The same effect is not verified when comparing cases D3 and E3, in Figs. 7.35c and 7.46c, respectively. For the latter, the higher the $\langle k \rangle$, the higher the $f$.

A plausible explanation for that is the fact that for Case E1, although $\langle k \rangle$ is smaller, the secondary motion is more intense, convecting $\langle k \rangle$ across the duct more effectively. This can be verified by the area occupied by the red shades in Fig. 7.46a.

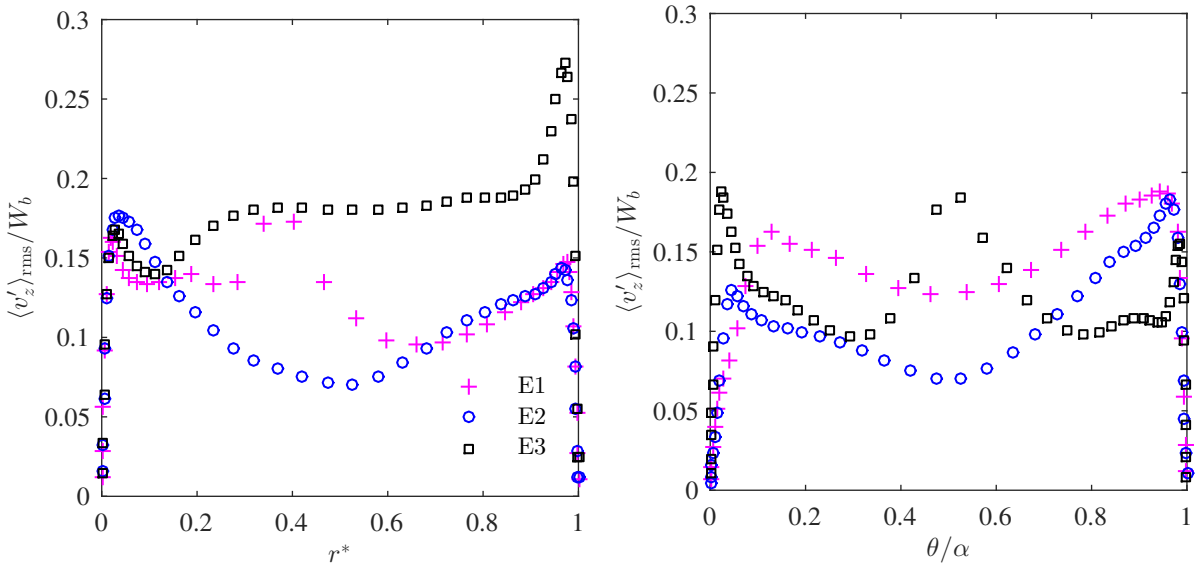


(a) RMS of the axial velocity fluctuation evaluated at $\theta = 0.5\alpha$

(b) RMS of the axial velocity fluctuation evaluated at $r^* = 0.5$

Figure 7.44 – Effect of $\eta$ on the axial velocity fluctuation. The profiles were normalised by $W_b$.

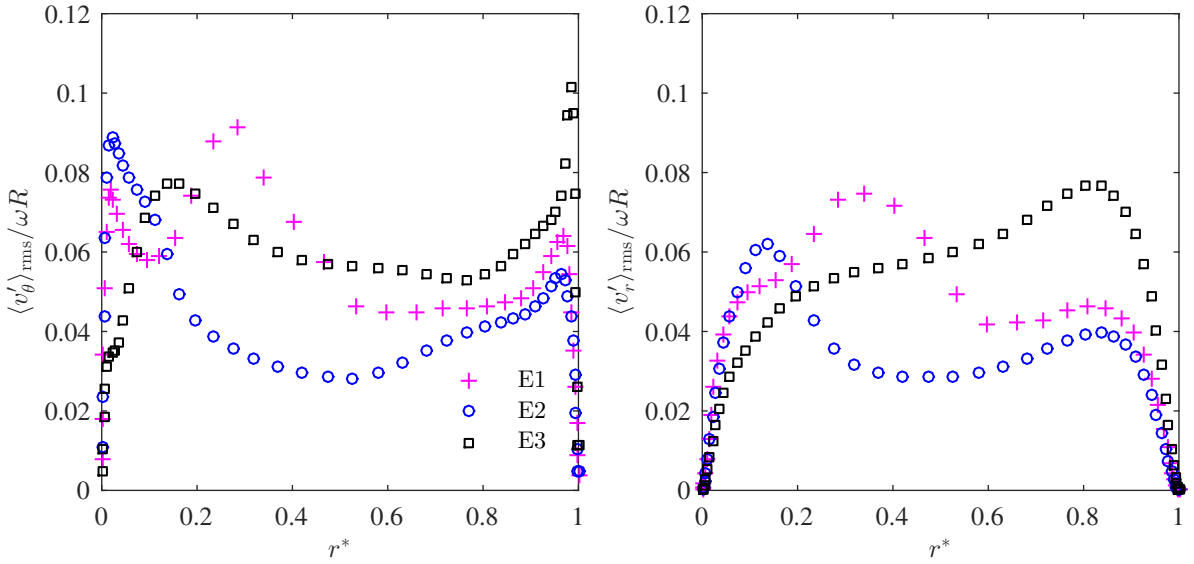


(a) RMS of the tangential velocity fluctuation

(b) RMS of the radial velocity fluctuation

Figure 7.45 – Effect of $\eta$ on the radial and tangential velocity fluctuations evaluated at $\theta = 0.5\alpha$. The profiles were normalised by $\omega R$.

## 7.8 Conclusion

The stationary duct case, presented in section 7.2, was found to resemble the characteristics of the square duct case. The mean profiles were compared with the DNS study of Pinelli et al. (2010). The difference found for the results, although not substantial, was attributed to the effect of the duct curvature. The secondary motion arrangement formed the same pattern of the square duct with octant-organised counter-rotating vortices. The maximum intensity of the secondary motion, 2.6% of the bulk flow, agreed very well with the results presented by Madabhushi and Vanka (1991). The friction factor was obtained

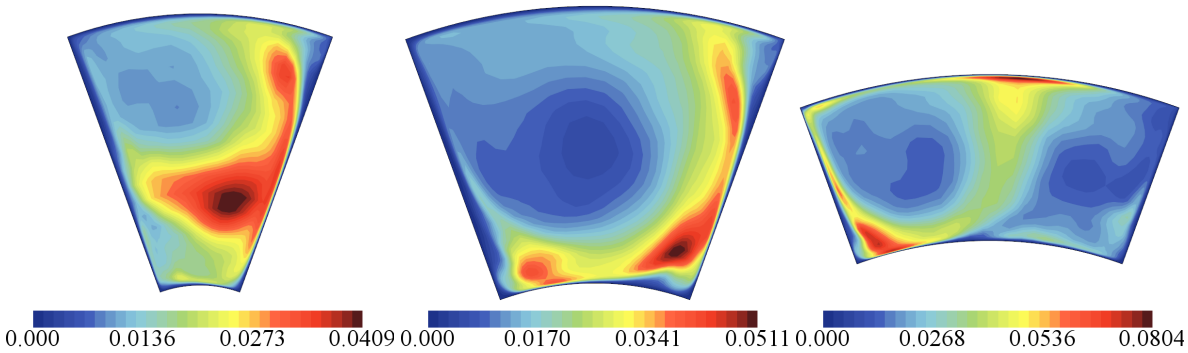


(a) Case E1 (b) Case E2 (c) Case E3

Figure 7.46 – Contours of the mean turbulent kinetic energy $\langle k \rangle$ normalised by $W_b^2$. (a) Case E1 with $\eta = 0.3$. (b) Case E2 with $\eta = 0.5$. Case E3 with $\eta = 0.7$.

and compared with the experimental prediction of Tao et al. (2000). The departure from the experimental correlation was of less than 1%.

The presence of rotation, described in section 7.3, caused the flow to experience the centrifugal and Coriolis effects. The secondary motion, besides having its intensity increased to approximately 10% of the bulk flow, was completely altered. The octant-organised pattern was replaced by a primary Coriolis-induced vortex with small and less intense structures near the corners. The friction factor was increased in 25%. The Coriolis-induced swirling motion was found to contribute to turbulent kinetic energy convection, increasing its volume-average in almost 50%.

By fixing the outer wall, the secondary motion assumed a flow pattern very similar to that found for lid-driven cavity problems. As described in section 7.4, the primary and secondary structures mentioned in the study of Koseff and Street (1984a) were all verified for Group C, in which the duct cross-section shape is closer to the square cavity. The fixed wall contributed to the swirling motion, driving the flow intensity from 10% to almost 200% of the bulk flow. The friction factor was increased by a factor of 4.

With the fixed outer wall, in section 7.5, the rotation speed of the duct was varied according with the investigated range of the swirl parameter $\Gamma$. The axial mean flow was substantially affected by $\Gamma$. Increasing $\Gamma$, for the investigated configuration, creates some sort of low turbulent intensity bulk region and the axial velocity profile develops a laminar-like shape. The tendencies regarding the secondary motion structures, as described in the the study of Koseff and Street (1984b) when increasing the lid speed, were also verified as the effect of $\Gamma$. A correlation for the friction factor was proposed as the sum of the stationary duct friction factor and the rotation-induced friction factor. For the highest $\Gamma$, Taylor-Göertler-like vortices formed as the flow is curved along the downstream secondary eddy. As $\Gamma$ was increased, the more energetic turbulence tended to concentrate near the walls with higher intensities near the inner wall. The viscous contribution to the total shear followed the same trends as the boundary layers thickness was reduced. The tendency to more stable bulk region was confirmed by the behaviour of the Reynolds stress tensor components.

The more unstable regions, on the other hand, were for every configuration, somehow related to the separation of the fluid from the walls. The point where it separates from the downstream wall and the way

it penetrates the duct cross-section have profound effect on the turbulent quantities and friction factor.

The duct geometry effect was then investigated by varying the duct apex angle $\alpha$ and radius ratio $\eta$. The influence of both parameters presented several similarities. For both smaller $\alpha$ and $\eta$ the motion induced by the stationary outer wall caused the primary vortex to occupy the upper part of the duct. The axial flow was then separated into a slow (inner wall region) and a fast (outer wall region) moving core. For the case regarding the smaller $\alpha$, the slow moving core was organised in a quasi purely-axial flow. For both bigger $\alpha$ and $\eta$, the flow also separated into two horizontally arranged cores.

The geometry effect on the friction factor showed an intriguing behaviour. While increasing $\alpha$ reduces the friction factor, driving it to the value found for the annular case, increasing $\eta$ displays a minimum point. The minimum point in $f$, found for case E2, suggests that an optimal hydrodynamical configuration may be determined. However, the confirmation would require a broader parametric analysis.

# 8 Conclusions

In this thesis the turbulent flow of a Newtonian fluid within an annular-sector duct subjected to parallel-mode rotation was solved numerically with the aid of a commercial CFD software. The study was motivated by the lack of in-depth understanding of the interplay between rotation- and shear-induced phenomena over the mean flow and turbulence-related quantities for a problem that has vast applicability in rotating machinery and internal cooling systems.

The momentum exchange between the mean flow and turbulent structures was accounted through a Large-Eddy Simulation technique. The numerical procedure and solution methodology were extensively tested against literature reference data. The comparison allowed to explore the software capabilities and limitations when dealing with complex turbulent flows. The results showed, in general, an excellent agreement with the reference data, granting reliability to the results regarding the annular-sector problem. For the latter, the influence of rotation and the shear effect of the stationary wall caused substantial change in the mean flow and turbulent quantities, which the analysis was restricted to second-order statistics.

The numerical investigation was performed by varying the swirl parameter $\Gamma = Re_\omega/Re_b$, the duct apex angle $\alpha$ and the radius ratio $\eta$. In general, the secondary motion presented characteristics strikingly similar to the problem known as lid-driven cavity. The typical flow structures found for the lid-driven problem could be also identified in the results, including Taylor-Göertler-like vortices. The secondary and streamwise motions were found to be highly coupled. The way the secondary motion develops has profound effect in the streamwise velocity distribution.

From an engineering perspective, the study contributed to the comprehension of the friction factor sensibility to the characteristic parameters. Increasing $\Gamma$ results in the monotonic increase of $f$. Increasing $\alpha$, on the other hand, results in the monotonic decrease (for the investigated range of $\alpha$) of $f$ toward the value found for the annular duct with same $\Gamma$ and $\eta$. For the radius ratio $\eta$, however, the friction factor presented a non-monotonic behaviour which suggests that there may be an optimal hydraulic configuration.

## 8.1 Suggestions for future research

For the annular-sector duct with the set of boundary conditions used in this study, the following topics could be considered in future research:

- The study of the stationary case, which presented substantial similarities with the square duct case, could be deeply investigated for a different set of $\alpha$ and $\eta$ configurations. This could help to isolate the effect of transverse curvature.
- The rotating case with non-stationary outer wall could also be investigated for different geometric configurations. One could also mimic the centrifugal force resulting from rotation as a source

term in the momentum equations and retain the duct stationary. That would help to access the contribution of the Coriolis force to the flow dynamics.

- With the contribution of the stationary wall, the secondary motion was found to resemble the lid-driven cavity problem. The behaviour of the secondary eddies, the downstream jet separation point and the nature of the boundary layers could be investigated in detail. The stabilising effect of the swirling motion could also be investigated for a broader range of $Re_\omega$ and $Re_b$.

- Discussions regarding the mean axial motion were conducted somewhat superficially. However, the results found in the literature showed that there is in fact a lot of room for discussion. As far as the author is aware of, relevant studies regarding the combination of lid-driven with axial throughflow are not available.

- The effect of the governing parameters on the turbulent quantities could be extended to the budgets of the turbulent kinetic energy. The production mechanisms could then be accessed allowing more insights on the turbulence dynamics.

- Finally, as a general suggestion, turbulence fundamental studies may always consider the use of high-order numerical methods. Model-free simulations with accurate numerical schemes can serve as an access road the fundamental concepts of turbulence and contribute to improve turbulence models.

# Bibliography

BERGER, S.; TALBOT, L.; YAO, L. Flow in curved pipes. *Annual review of fluid mechanics*, Annual Reviews 4139 El Camino Way, PO Box 10139, Palo Alto, CA 94303-0139, USA, v. 15, n. 1, p. 461–512, 1983.

BOURGOYNE, A. T.; MILLHEIM, K. K.; CHENEVERT, M. E.; YOUNG, F. *Applied drilling engineering*. [S.l.]: Society of Petroleum Engineering of AIME, 1986.

BRADSHAW, P. *Effects of Streamline Curvature on Turbulent Flow.* [S.l.], 1973.

CABRAL, B.; LEEDOM, L. C. Imaging vector fields using line integral convolution. In: ACM. *Proceedings of the 20th annual conference on Computer graphics and interactive techniques*. [S.l.], 1993. p. 263–270.

CELIK, I. Random flow generation technique for large eddy simulations and particle-dynamics modeling. 2001.

CHALLONER, J.; BAYLIS, T. *1001 inventions that changed the world*. [S.l.]: Cassell Illustrated, 2009.

CHIU, H.-C.; JANG, J.-H.; YAN, W.-M. Combined mixed convection and radiation heat transfer in rectangular ducts rotating about a parallel axis. *International journal of heat and mass transfer*, Elsevier, v. 50, n. 21, p. 4229–4242, 2007.

CHUNG, S. Y.; RHEE, G. H.; SUNG, H. J. Direct numerical simulation of turbulent concentric annular pipe flow: Part 1: Flow field. *International Journal of Heat and Fluid Flow*, Elsevier, v. 23, n. 4, p. 426–440, 2002.

DAI, Y.-J.; HUANG, W.-X.; XU, C.-X.; CUI, G.-X. Direct numerical simulation of turbulent flow in a rotating square duct. *Physics of Fluids*, AIP Publishing, v. 27, n. 6, p. 065104, 2015.

DARWISH, M.; MOUKALLED, F. Normalized variable and space formulation methodology for high-resolution schemes. *Numerical Heat Transfer*, Taylor & Francis, v. 26, n. 1, p. 79–96, 1994.

DAVIDSON, P. *Turbulence: An Introduction for Scientists and Engineers*. [S.l.]: OUP Oxford, 2004. ISBN 9780191589850.

DAVIDSON, P. *Turbulence in Rotating, Stratified and Electrically Conducting Fluids*. [S.l.]: Cambridge University Press, 2013. ISBN 9781107026865.

DAVIDSON, P. *Turbulence: an introduction for scientists and engineers*. [S.l.]: Oxford University Press, 2015.

DAVIES, S.; WHITE, C. An experimental study of the flow of water in pipes of rectangular section. In: THE ROYAL SOCIETY. *Proceedings of the Royal Society of London A: Mathematical, Physical and Engineering Sciences*. [S.l.], 1928. v. 119, n. 781, p. 92–107.

DEAN, R. Reynolds number dependence of skin friction and other bulk flow variables in two-dimensional rectangular duct flow. *J. Fluids Eng*, Citeseer, v. 100, n. 2, p. 215–223, 1978.

DEAN, W. Xvi. note on the motion of fluid in a curved pipe. *The London, Edinburgh, and Dublin Philosophical Magazine and Journal of Science*, Taylor & Francis, v. 4, n. 20, p. 208–223, 1927.

DEAN, W. Fluid motion in a curved channel. In: THE ROYAL SOCIETY. *Proceedings of the Royal Society of London A: Mathematical, Physical and Engineering Sciences*. [S.l.], 1928. v. 121, n. 787, p. 402–420.

DEAN, W. Lxxii. the stream-line motion of fluid in a curved pipe (second paper). *The London, Edinburgh, and Dublin Philosophical Magazine and Journal of Science*, Taylor & Francis, v. 5, n. 30, p. 673–695, 1928.

DEARDORFF, J. W. A numerical study of three-dimensional turbulent channel flow at large reynolds numbers. *Journal of Fluid Mechanics*, Cambridge Univ Press, v. 41, n. 02, p. 453–480, 1970.

Di Piazza, I.; CIOFALO, M. Numerical prediction of turbulent flow and heat transfer in helically coiled pipes. *International Journal of Thermal Sciences*, Elsevier Masson SAS, v. 49, n. 4, p. 653–663, 2010. ISSN 12900729.

DONG, S. Direct numerical simulation of turbulent taylor–couette flow. *Journal of Fluid Mechanics*, Cambridge Univ Press, v. 587, p. 373–393, 2007.

DURBIN, P. A.; REIF, B. P. *Statistical theory and modeling for turbulent flows*. [S.l.]: John Wiley & Sons, 2011.

ESKINAZI, S.; YEH, H. An investigation on fully developed turbulent flows in a curved channel. *Journal of the Aeronautical Sciences*, 1956.

EUSTICE, J. Flow of water in curved pipes. *Proceedings of the Royal Society of London. Series A, Containing Papers of a Mathematical and Physical Character*, JSTOR, v. 84, n. 568, p. 107–118, 1910.

EUSTICE, J. Experiments on stream-line motion in curved pipes. *Proceedings of the Royal Society of London. Series A, Containing Papers of a Mathematical and Physical Character*, JSTOR, v. 85, n. 576, p. 119–131, 1911.

FANG, X.; YANG, Z.; WANG, B.-C.; BERGSTROM, D. J. Direct numerical simulation of turbulent flow in a spanwise rotating square duct at high rotation numbers. *International Journal of Heat and Fluid Flow*, Elsevier, 2016.

FASQUELLE, A.; PELLÉ, J.; HARMAND, S.; SHEVCHUK, I. V. Numerical study of convective heat transfer enhancement in a pipe rotating around a parallel axis. *Journal of Heat Transfer*, American Society of Mechanical Engineers, v. 136, n. 5, p. 051901, 2014.

FÉNOT, M.; BERTIN, Y.; DORIGNAC, E.; LALIZEL, G. A review of heat transfer between concentric rotating cylinders with or without axial flow. *International journal of thermal sciences*, Elsevier, v. 50, n. 7, p. 1138–1155, 2011.

FERZIGER, J. H. Large eddy numerical simulations of turbulent flows. *AIAA J*, v. 15, n. 9, p. 1261–1267, 1977.

GERMANO, M.; PIOMELLI, U.; MOIN, P.; CABOT, W. H. A dynamic subgrid-scale eddy viscosity model. *Physics of Fluids A: Fluid Dynamics*, AIP, v. 3, n. 7, p. 1760–1765, 1991.

GRUNDESTAM, O.; WALLIN, S.; JOHANSSON, A. V. Direct numerical simulations of rotating turbulent channel flow. *Journal of Fluid Mechanics*, Cambridge Univ Press, v. 598, p. 177–199, 2008.

HART, J. E. Instability and secondary motion in a rotating channel flow. *Journal of Fluid mechanics*, Cambridge Univ Press, v. 45, n. 02, p. 341–351, 1971.

HSIEH, A. S.; BIRINGEN, S.; KUCALA, A. Simulation of rotating channel flow with heat transfer: Evaluation of closure models. *Journal of Turbomachinery*, American Society of Mechanical Engineers, v. 138, n. 11, p. 111009, 2016.

HUNT, I.; JOUBERT, P. Effects of small streamline curvature on turbulent duct flow. *Journal of Fluid Mechanics*, Cambridge Univ Press, v. 91, n. 04, p. 633–659, 1979.

HUSER, A.; BIRINGEN, S. Direct numerical simulation of turbulent flow in a square duct. In: *31st Aerospace Sciences Meeting*. [S.l.: s.n.], 1992. p. 198.

ITO, H. Flow in Curved Pipes. *JSME Int. J.*, v. 30, p. 543–552, 1987.

JARRIN, N.; BENHAMADOUCHE, S.; LAURENCE, D.; PROSSER, R. A synthetic-eddy-method for generating inflow conditions for large-eddy simulations. *International Journal of Heat and Fluid Flow*, Elsevier, v. 27, n. 4, p. 585–593, 2006.

JIMÉNEZ, J. Near-wall turbulence. *Physics of Fluids*, AIP, v. 25, n. 10, p. 101302, 2013.

JOHNSON, A.; MORRIS, W. Experimental investigation of the effect of entry conditions and rotation on flow resistance in circular tubes rotating about a parallel axis. *International journal of heat and fluid flow*, Elsevier, v. 5, n. 2, p. 121–127, 1984.

JOHNSTON, J. P.; HALLEENT, R. M.; LEZIUS, D. K. Effects of spanwise rotation on the structure of two-dimensional fully developed turbulent channel flow. *Journal of Fluid Mechanics*, Cambridge Univ Press, v. 56, n. 03, p. 533–557, 1972.

KANG, C.; YANG, K.-S. Large eddy simulation of turbulent heat transfer in curved-pipe flow. *Journal of Heat Transfer*, American Society of Mechanical Engineers, v. 138, n. 1, p. 011704, 2016.

KAO, H. C. Torsion effect on fully developed flow in a helical pipe. *Journal of Fluid Mechanics*, Cambridge Univ Press, v. 184, p. 335–356, 1987.

KAWAHARA, G.; AYUKAWA, K.; OCHI, J.; ONO, F.; KAMADA, E. Wall shear stress and reynolds stresses in a low reynolds number turbulent square duct flow. *Trans. JSME B*, v. 66, n. 641, p. 95–102, 2000.

KIM, J.; MOIN, P.; MOSER, R.; KIM, B. J. Turbulence statistics in fully developed channel flow at low Reynolds number. *Journal of Fluid Mechanics*, v. 177, n. 1987, p. 133, 1987.

KOLMOGOROV, A. N. The local structure of turbulence in incompressible viscous fluid for very large reynolds numbers. In: JSTOR. *Dokl. Akad. Nauk SSSR*. [S.l.], 1941. v. 30, n. 4, p. 301–305.

KOSEFF, J.; STREET, R. The lid-driven cavity flow: a synthesis of qualitative and quantitative observations. *Journal of Fluids Engineering*, American Society of Mechanical Engineers, v. 106, n. 4, p. 390–398, 1984.

KOSEFF, J. R.; STREET, R. On end wall effects in a lid-driven cavity flow. *Journal of fluids engineering*, American Society of Mechanical Engineers, v. 106, n. 4, p. 385–389, 1984.

KREPLIN, H.-P.; ECKELMANN, H. Behavior of the three fluctuating velocity components in the wall region of a turbulent channel flow. *Physics of Fluids*, v. 22, n. 1979, p. 1233–1239, 1979.

KUBACKI, S.; ROKICKI, J.; DICK, E. Simulation of the flow in a ribbed rotating duct with a hybrid k-omega. *Flow, Turbulence and Combustion*, Springer, v. 97, n. 1, p. 45–78, 2016.

LAUFER, J. Investigation of turbulent flow in a 2-d channel. *Tech. Note*, v. 2123, 1950.

LEE, M.; MOSER, R. D. Direct numerical simulation of turbulent channel flow up to re=5200. *Journal of Fluid Mechanics*, Cambridge University Press, v. 774, p. 395–415, 2015.

LEONARD, A. Energy cascade in large-eddy simulations of turbulent fluid flows. *Advances in geophysics*, Elsevier, v. 18, p. 237–248, 1974.

LEONARD, B. The ultimate conservative difference scheme applied to unsteady one-dimensional advection. *Computer methods in applied mechanics and engineering*, Elsevier, v. 88, n. 1, p. 17–74, 1991.

LESIEUR, M.; MÉTAIS, O.; COMTE, P. *Large-eddy simulations of turbulence*. [S.l.]: Cambridge University Press, 2005.

LEVY, E.; KANNAN, K. Computation of laminar heat transfer in rotating rectangular ducts. *Journal of heat transfer*, v. 107, p. 575, 1985.

LEVY, N.; BROWN, G.; BAYAT, F.; KADAMBI, V. Laminar heat transfer and pressure drop in a rectangular duct rotating about a parallel axis. 1986.

LILLY, D. K. On the application of eddy viscosity concept in the inertial sub-range of turbulence. *NCAR manuscript*, v. 123, 1966.

LILLY, D. K. A proposed modification of the germano subgrid-scale closure method. *Physics of Fluids A: Fluid Dynamics*, AIP, v. 4, n. 3, p. 633–635, 1992.

MADABHUSHI, R. K.; VANKA, S. Large eddy simulation of turbulence-driven secondary flow in a square duct. *Physics of Fluids A: Fluid Dynamics*, AIP, v. 3, n. 11, p. 2734–2745, 1991.

MENTER, F. R. Improved two-equation k-omega turbulence models for aerodynamic flows. 1992.

MOIN, P.; KIM, J. Numerical investigation of turbulent channel flow. *Journal of Fluid Mechanics*, v. 118, n. April 2006, p. 341, 1982.

MOIN, P.; REYNOLDS, W.; FERZIGER, J. H. Large eddy simulation of incompressible turbulent channel flow. 1978.

MOORE, J. A wake and an eddy in a rotating radial-flow passage. *ASME J. Eng. Power*, v. 95, p. 205–212, 1973.

MORI, Y.; NAKAYAMA, W. Forced convective heat transfer in a straight pipe rotating around a parallel axis:(1st report, laminar regionit). *International Journal of Heat and Mass Transfer*, Elsevier, v. 10, n. 9, p. 1179–1194, 1967.

MOSER, R. D.; KIM, J.; MANSOUR, N. N. Direct numerical simulation of turbulent channel flow up to Re=590. *Physics of Fluids*, v. 11, n. 4, p. 943–945, 1999.

MOSER, R. D.; MOIN, P. The effects of curvature in wall-bounded turbulent flows. *Journal of Fluid Mechanics*, v. 175, p. 479, 1987.

NANBU, K. Flow in rotating straight pipes of circular cross section. *Journal of Basic Engineering*, p. 383, 1971.

NICOUD, F.; DUCROS, F. Subgrid-scale stress modelling based on the square of the velocity gradient tensor. *Flow, turbulence and Combustion*, Springer, v. 62, n. 3, p. 183–200, 1999.

OSTILLA-MÓNICO, R.; VERZICCO, R.; GROSSMANN, S.; LOHSE, D. The near-wall region of highly turbulent taylor–couette flow. *Journal of fluid mechanics*, Cambridge Univ Press, v. 788, p. 95–117, 2016.

PATANKAR, S. *Numerical heat transfer and fluid flow*. [S.l.]: CRC press, 1980.

PATANKAR, S.; LIU, C.; SPARROW, E. Fully developed flow and heat transfer in ducts having streamwise-periodic variations of cross-sectional area. *Journal of Heat Transfer*, American Society of Mechanical Engineers, v. 99, n. 2, p. 180–186, 1977.

PATANKAR, S. V.; PRATAP, V.; SPALDING, D. Prediction of turbulent flow in curved pipes. *Journal of Fluid Mechanics*, Cambridge Univ Press, v. 67, n. 03, p. 583–595, 1975.

PINELLI, A.; UHLMANN, M.; SEKIMOTO, A.; KAWAHARA, G. Reynolds number dependence of mean flow structure in square duct turbulence. *Journal of fluid mechanics*, Cambridge Univ Press, v. 644, p. 107–122, 2010.

PONCET, S.; HADDADI, S.; VIAZZO, S. Numerical modeling of fluid flow and heat transfer in a narrow taylor–couette–poiseuille system. *International Journal of Heat and Fluid Flow*, Elsevier, v. 32, n. 1, p. 128–144, 2011.

PONCET, S.; VIAZZO, S.; OGUIC, R. Large eddy simulations of taylor-couette-poiseuille flows in a narrow-gap system. *Physics of Fluids*, AIP, v. 26, n. 10, p. 105108, 2014.

POPE, S. B. *Turbulent flows*. [S.l.]: Cambridge university press, 2000.

PRASAD, A. K.; KOSEFF, J. R. Reynolds number and end-wall effects on a lid-driven cavity flow. *Physics of Fluids A: Fluid Dynamics*, AIP, v. 1, n. 2, p. 208–218, 1989.

REIF, B. P.; ANDERSSON, H. Prediction of turbulence-generated secondary mean flow in a square duct. *Flow, turbulence and combustion*, Springer, v. 68, n. 1, p. 41, 2002.

REYNOLDS, O. An experimental investigation of the circumstances which determine whether the motion of water shall be direct or sinuous, and of the law of resistance in parallel channels. *Proceedings of the royal society of London*, The Royal Society, v. 35, n. 224-226, p. 84–99, 1883.

REYNOLDS, O. On the dynamical theory of incompressible viscous fluids and the determination of the criterion. *Proceedings of the Royal Society of London*, The Royal Society, v. 56, n. 336-339, p. 40–45, 1894.

RODI, W. Turbulence modeling and simulation in hydraulics: A historical review. *Journal of Hydraulic Engineering*, American Society of Civil Engineers, p. 03117001, 2017.

RODI, W.; CONSTANTINESCU, G.; STOESSER, T. *Large-eddy simulation in hydraulics*. [S.l.]: Crc Press, 2013.

SCHMITT, F. G. About boussinesq's turbulent viscosity hypothesis: historical remarks and a direct evaluation of its validity. *Comptes Rendus Mécanique*, Elsevier, v. 335, n. 9-10, p. 617–627, 2007.

SCHULTZ, M. P.; FLACK, K. A. Reynolds-number scaling of turbulent channel flow. *Physics of Fluids*, AIP, v. 25, n. 2, p. 025104, 2013.

SLEITI, A. K.; KAPAT, J. S. Heat transfer in channels in parallel-mode rotation at high rotation numbers. *Journal of thermophysics and heat transfer*, v. 20, n. 4, p. 748–753, 2006.

SOONG, C.; YAN, W. Development of secondary flow and convective heat transfer in isothermal iso-flux rectangular ducts rotating about a parallel axis. *International Journal of heat and mass transfer*, Elsevier, v. 42, n. 3, p. 497–510, 1999.

SPARROW, E.; CHEN, T.; JONSSON, V. Laminar flow and pressure drop in internally finned annular ducts. *International Journal of Heat and Mass Transfer*, Elsevier, v. 7, n. 5, p. 583–585, 1964.

TAO, W.-Q.; LU, S.-S.; KANG, H.; LIN, M. Experimental study on developing and fully developed fluid flow and heat transfer in annular-sector ducts. *Journal of Enhanced Heat Transfer*, Begel House Inc., v. 7, n. 1, 2000.

TAYLOR, G. The criterion for turbulence in curved pipes. In: THE ROYAL SOCIETY. *Proceedings of the Royal Society of London A: Mathematical, Physical and Engineering Sciences*. [S.l.], 1929. v. 124, n. 794, p. 243–249.

VENKATAKRISHNAN, V. *On the convergence of limiters and convergence to steady state solutions*. [S.l.], 1993.

VERSTEEG, H.; MALALASEKERA, W. *An Introduction to Computational Dynamics: The Finite Volume Method*. [S.l.]: Prentice Hill, 2007.

WATTENDORF, F. L. A study of the effect of curvature on fully developed turbulent flow. In: THE ROYAL SOCIETY. *Proceedings of the Royal Society of London A: Mathematical, Physical and Engineering Sciences*. [S.l.], 1935. v. 148, n. 865, p. 565–598.

WHITE, C. Streamline flow through curved pipes. In: THE ROYAL SOCIETY. *Proceedings of the Royal Society of London A: Mathematical, Physical and Engineering Sciences*. [S.l.], 1929. v. 123, n. 792, p. 645–663.

WHITE, F. M.; CORFIELD, I. *Viscous fluid flow*. [S.l.]: McGraw-Hill New York, 2006. v. 3.

ZOLLNER, F. *Leonardo Da Vinci, 1452-1519: Sketches and Drawings*. [S.l.]: Taschen, 2004.

# APPENDIX A – Governing equations in cylindrical coordinates

## A.1 Conservation equaions

As seen from Fig. 4.1, $\mathbf{\Omega} = \omega\hat{\mathbf{e}}_z$ and therefore, the Centrifugal and Coriolis forces in Eq. 4.5 reduce to:

$$\mathbf{\Omega} \times (\mathbf{\Omega} \times \mathbf{r}) = -\nabla \left[\frac{1}{2}(\mathbf{\Omega} \times \mathbf{r})^2\right] = -\frac{\partial}{\partial r}\left[\frac{1}{2}(\omega r)^2\right]\hat{\mathbf{e}}_r \tag{A.1}$$

$$2\mathbf{\Omega} \times \mathbf{u} = 2\omega(v_r\hat{\mathbf{e}}_\theta - v_\theta\hat{\mathbf{e}}_r) \tag{A.2}$$

The continuity and momentum equations are presented in cylindrical coordinates for a newtonian incompressible fluid. The gravity is neglected.

Continuity:

$$\frac{1}{r}\frac{\partial}{\partial r}(rv_r) + \frac{1}{r}\frac{\partial}{\partial \theta}(v_\theta) + \frac{\partial}{\partial z}(v_z) = 0 \tag{A.3}$$

$r$-component:

$$\rho\left(\frac{\partial v_r}{\partial t} + v_r\frac{\partial v_r}{\partial r} + \frac{v_\theta}{r}\frac{\partial v_r}{\partial \theta} - \frac{v_\theta^2}{r} + v_z\frac{\partial v_r}{\partial z}\right) - 2\omega v_\theta = \tag{A.4}$$
$$-\frac{\partial p}{\partial r} - \frac{\partial}{\partial r}\left(\frac{1}{2}(\omega r)^2\right) + \mu\left\{\frac{\partial}{\partial r}\left(\frac{1}{r}\frac{\partial}{\partial r}[rv_r]\right) + \frac{1}{r^2}\frac{\partial^2 v_r}{\partial \theta^2} - \frac{2}{r^2}\frac{\partial v_\theta}{\partial \theta} + \frac{\partial^2 v_r}{\partial z^2}\right\}$$

$\theta$-component:

$$\rho\left(\frac{\partial v_\theta}{\partial t} + v_r\frac{\partial v_\theta}{\partial r} + \frac{v_\theta}{r}\frac{\partial v_\theta}{\partial \theta} + \frac{v_r v_\theta}{r} + v_z\frac{\partial v_\theta}{\partial z}\right) + 2\omega v_r = \tag{A.5}$$
$$-\frac{\partial p}{\partial \theta} + \mu\left\{\frac{\partial}{\partial r}\left(\frac{1}{r}\frac{\partial}{\partial r}[rv_\theta]\right) + \frac{1}{r^2}\frac{\partial^2 v_\theta}{\partial \theta^2} - \frac{2}{r^2}\frac{\partial v_r}{\partial \theta} + \frac{\partial^2 v_\theta}{\partial z^2}\right\}$$

$z$-component:

$$\rho\left(\frac{\partial v_z}{\partial t} + v_r\frac{\partial v_z}{\partial r} + \frac{v_\theta}{r}\frac{\partial v_z}{\partial \theta} + v_z\frac{\partial v_z}{\partial z}\right) = \tag{A.6}$$
$$-\frac{\partial p}{\partial z} + \mu\left\{\frac{1}{r}\frac{\partial}{\partial r}\left(r\frac{\partial v_z}{\partial r}\right) + \frac{1}{r^2}\frac{\partial^2 v_z}{\partial \theta^2} + \frac{\partial^2 v_z}{\partial z^2}\right\}$$

## A.2 Reynolds-averaged equations

The Reynolds decomposition states that any flow quantity $\phi(\mathbf{x},t)$ may represented as the sum of a mean $\phi(\mathbf{x})$ and a time-varying fluctuating component $\phi'(\mathbf{x},t)$, that is:

$$\phi(\mathbf{x},t) = \overline{\phi}(\mathbf{x}) + \phi'(\mathbf{x},t) \tag{A.7}$$

where the following relations apply:

$$\overline{\phi(\mathbf{x},t)} = \frac{1}{T}\int_{t-\frac{T}{2}}^{t+\frac{T}{2}} \phi(\mathbf{x},t)dt \tag{A.8}$$

$$\overline{\phi'(\mathbf{x},t)} = 0 \tag{A.9}$$

From Eq. A.8 and A.9 it is easy to show that:

$$\overline{s\phi} = \frac{1}{T}\int_{t-\frac{T}{2}}^{t+\frac{T}{2}} s\phi dt = \frac{s}{T}\int_{t-\frac{T}{2}}^{t+\frac{T}{2}} \phi dt = s\overline{\phi} \tag{A.10}$$

$$\overline{\frac{\partial\phi}{\partial x}} = \frac{1}{T}\int_{t-\frac{T}{2}}^{t+\frac{T}{2}} \frac{\partial\phi}{\partial x}dt = \frac{\partial}{\partial x}\left[\frac{1}{T}\int_{t-\frac{T}{2}}^{t+\frac{T}{2}} \phi dt\right] = \frac{\partial\overline{\phi}}{\partial x} \tag{A.11}$$

$$\overline{\frac{\partial\phi}{\partial t}} = \frac{1}{T}\int_{t-\frac{T}{2}}^{t+\frac{T}{2}} \frac{\partial\phi}{\partial t}dt = \frac{\partial}{\partial t}\left[\frac{1}{T}\int_{t-\frac{T}{2}}^{t+\frac{T}{2}} \phi dt\right] = \frac{\partial\overline{\phi}}{\partial t} \tag{A.12}$$

$$\overline{\overline{\phi}} = \frac{1}{T}\int_{t-\frac{T}{2}}^{t+\frac{T}{2}} \overline{\phi}dt = \overline{\phi} \tag{A.13}$$

$$\overline{\phi\psi} = \frac{1}{T}\int_{t-\frac{T}{2}}^{t+\frac{T}{2}} \phi\psi dt = \frac{1}{T}\int_{t-\frac{T}{2}}^{t+\frac{T}{2}} \left(\overline{\phi}+\phi'\right)\left(\overline{\psi}+\psi'\right)dt = \overline{\overline{\phi}\,\overline{\psi}} + \overline{\overline{\phi}\,\psi'} + \overline{\phi'\,\overline{\psi}} + \overline{\phi'\psi'} \tag{A.14}$$

$$\overline{\phi\psi} = \overline{\phi}\,\overline{\psi} + \overline{\phi'\psi'}$$

$$\overline{\phi+\psi} = \frac{1}{T}\int_{t-\frac{T}{2}}^{t+\frac{T}{2}} (\phi+\psi)\,dt = \overline{\phi} + \overline{\psi} \tag{A.15}$$

where $s$ represents a constant.

### A.2.1 Time-averaged continuity equation

Substituting Eq. A.7 into A.3 and averaging over time yields:

$$\overline{\frac{1}{r}\frac{\partial}{\partial r}\left(r(\overline{v_r}+v_r')\right)}+\overline{\frac{1}{r}\frac{\partial}{\partial \theta}\left(\overline{v_\theta}+v_\theta'\right)}+\overline{\frac{\partial}{\partial z}\left(\overline{v_z}+v_z'\right)}=0 \tag{A.16}$$

$$\frac{1}{r}\frac{\partial}{\partial r}\left(r\overline{v_r}\right)+\frac{1}{r}\frac{\partial}{\partial \theta}\left(\overline{v_\theta}\right)+\frac{\partial}{\partial z}\left(\overline{v_z}\right)=0 \tag{A.17}$$

$$\frac{1}{r}\frac{\partial}{\partial r}\left(r\overline{v_r'}\right)+\frac{1}{r}\frac{\partial}{\partial \theta}\left(\overline{v_\theta'}\right)+\frac{\partial}{\partial z}\left(\overline{v_z'}\right)=\frac{1}{r}\frac{\partial}{\partial r}\left(rv_r'\right)+\frac{1}{r}\frac{\partial}{\partial \theta}\left(v_\theta'\right)+\frac{\partial}{\partial z}\left(v_z'\right)=0 \tag{A.18}$$

### A.2.2 Time-averaged Navier-Stokes

$$\rho\left(\overline{\frac{\partial(\overline{v_r}+v_r')}{\partial t}}+\overline{(\overline{v_r}+v_r')\frac{\partial(\overline{v_r}+v_r')}{\partial r}}+\overline{\frac{(\overline{v_\theta}+v_\theta')}{r}\frac{\partial(\overline{v_r}+v_r')}{\partial\theta}}-\overline{\frac{(\overline{v_\theta}+v_\theta')^2}{r}}+\overline{(\overline{v_z}+v_z')\frac{\partial(\overline{v_r}+v_r')}{\partial z}}\right)-\overline{2\omega(\overline{v_\theta}+v_\theta')}= \tag{A.19}$$
$$-\overline{\frac{\partial}{\partial r}\left(p+\frac{1}{2}(\omega r)^2\right)}+\mu\left\{\overline{\frac{\partial}{\partial r}\left(\frac{1}{r}\frac{\partial}{\partial r}\left[r(\overline{v_r}+v_r')\right]\right)}+\overline{\frac{1}{r^2}\frac{\partial^2(\overline{v_r}+v_r')}{\partial\theta^2}}-\overline{\frac{2}{r^2}\frac{\partial(\overline{v_\theta}+v_\theta')}{\partial\theta}}+\overline{\frac{\partial^2(\overline{v_r}+v_r')}{\partial z^2}}\right\}$$

Term by term, Eq. A.19 becomes:

$$\overline{\frac{\partial(\overline{v_r}+v_r')}{\partial t}}=\frac{\partial}{\partial t}\left(\overline{\overline{v_r}+v_r'}\right)=\frac{\partial\overline{v_r}}{\partial t} \tag{A.20}$$

$$\overline{(\overline{v_r}+v_r')\frac{\partial(\overline{v_r}+v_r')}{\partial r}}=\overline{\overline{v_r}\frac{\partial(\overline{v_r}+v_r')}{\partial r}+v_r'\frac{\partial(\overline{v_r}+v_r')}{\partial r}}=\overline{\overline{v_r}\frac{\partial\overline{v_r}}{\partial r}+\overline{v_r}\frac{\partial v_r'}{\partial r}+v_r'\frac{\partial\overline{v_r}}{\partial r}+v_r'\frac{\partial v_r'}{\partial r}}=\overline{v_r}\frac{\partial\overline{v_r}}{\partial r}+\overline{v_r'\frac{\partial v_r'}{\partial r}} \tag{A.21}$$

$$\overline{\frac{(\overline{v_\theta}+v_\theta')}{r}\frac{\partial(\overline{v_r}+v_r')}{\partial\theta}}=\overline{\frac{\overline{v_\theta}}{r}\frac{\partial(\overline{v_r}+v_r')}{\partial\theta}+\frac{v_\theta'}{r}\frac{\partial(\overline{v_r}+v_r')}{\partial\theta}}=\overline{\frac{\overline{v_\theta}}{r}\frac{\partial\overline{v_r}}{\partial\theta}+\frac{\overline{v_\theta}}{r}\frac{\partial v_r'}{\partial\theta}+\frac{v_\theta'}{r}\frac{\partial\overline{v_r}}{\partial\theta}+\frac{v_\theta'}{r}\frac{\partial v_r'}{\partial\theta}}=\frac{\overline{v_\theta}}{r}\frac{\partial\overline{v_r}}{\partial\theta}+\overline{\frac{v_\theta'}{r}\frac{\partial v_r'}{\partial\theta}} \tag{A.22}$$

$$\overline{\frac{(\overline{v_\theta}+v_\theta')^2}{r}}=\overline{\frac{(\overline{v_\theta}+v_\theta')(\overline{v_\theta}+v_\theta')}{r}}=\overline{\frac{\overline{v_\theta}\overline{v_\theta}+2\overline{v_\theta}v_\theta'+v_\theta'v_\theta'}{r}}=\frac{\overline{v_\theta}\overline{v_\theta}}{r}+\frac{\overline{v_\theta'v_\theta'}}{r} \tag{A.23}$$

$$\overline{(\overline{v_z}+v_z')\frac{\partial(\overline{v_r}+v_r')}{\partial z}}=\overline{\overline{v_z}\frac{\partial(\overline{v_r}+v_r')}{\partial z}+v_z'\frac{\partial(\overline{v_r}+v_r')}{\partial z}}=\overline{v_z}\frac{\partial\overline{v_r}}{\partial z}+\overline{v_z'\frac{\partial v_r'}{\partial z}} \tag{A.24}$$

$$\overline{2\omega(\overline{v_\theta}+v_\theta')}=2\omega(\overline{v_\theta}+\overline{v_\theta'})=2\omega\overline{v_\theta} \tag{A.25}$$

The Centrifugal and pressure terms are add together to form the modified pressure term:

$$\overline{\frac{\partial}{\partial r}\left(p+\frac{1}{2}\left(\omega r\right)^2\right)}=\frac{\partial\overline{P}}{\partial r} \tag{A.26}$$

$$\overline{\frac{\partial}{\partial r}\left(\frac{1}{r}\frac{\partial}{\partial r}\left[r(\overline{v_r}+v_r')\right]\right)}=\frac{\partial}{\partial r}\left(\frac{1}{r}\frac{\partial}{\partial r}\left[r(\overline{\overline{v_r}+v_r'})\right]\right)=\frac{\partial}{\partial r}\left(\frac{1}{r}\frac{\partial}{\partial r}\left[r(\overline{v_r})\right]\right)+\frac{\partial}{\partial r}\left(\frac{1}{r}\frac{\partial}{\partial r}\left[r(\overline{v_r'})\right]\right)=\frac{\partial}{\partial r}\left(\frac{1}{r}\frac{\partial}{\partial r}\left[r(\overline{v_r})\right]\right) \tag{A.27}$$

$$\overline{\frac{1}{r^2}\frac{\partial^2(\overline{v_r}+v_r')}{\partial\theta^2}}=\frac{1}{r^2}\frac{\partial^2(\overline{\overline{v_r}+v_r'})}{\partial\theta^2}=\frac{1}{r^2}\frac{\partial^2(\overline{v_r})}{\partial\theta^2}+\frac{1}{r^2}\frac{\partial^2(v_r')}{\partial\theta^2}=\frac{1}{r^2}\frac{\partial^2\overline{v_r}}{\partial\theta^2} \tag{A.28}$$

$$\overline{\frac{2}{r^2}\frac{\partial(\overline{v_\theta}+v_\theta')}{\partial\theta}}=\frac{2}{r^2}\frac{\partial(\overline{\overline{v_\theta}+v_\theta'})}{\partial\theta}=\frac{2}{r^2}\frac{\partial(\overline{v_\theta})}{\partial\theta}+\frac{2}{r^2}\frac{\partial(\overline{v_\theta'})}{\partial\theta}=\frac{2}{r^2}\frac{\partial(\overline{v_\theta})}{\partial\theta} \tag{A.29}$$

$$\overline{\frac{\partial^2(\overline{v_r}+v_r')}{\partial z^2}}=\frac{\partial^2(\overline{\overline{v_r}+v_r'})}{\partial z^2}=\frac{\partial^2(\overline{v_r})}{\partial z^2}+\frac{\partial^2(\overline{v_r'})}{\partial z^2}=\frac{\partial^2\overline{v_r}}{\partial z^2} \tag{A.30}$$

Therefore, the $r$-component of the N-S equation becomes:

$$\begin{aligned}\rho\left(\frac{\partial\overline{v_r}}{\partial t}+\overline{v_r}\frac{\partial\overline{v_r}}{\partial r}+\frac{\overline{v_\theta}}{r}\frac{\partial\overline{v_r}}{\partial\theta}-\frac{\overline{v_\theta}^2}{r}+\overline{v_z}\frac{\partial\overline{v_r}}{\partial z}+\overline{v_z'\frac{\partial v_r'}{\partial z}}-\overline{\frac{v_\theta'^2}{r}}+\overline{v_r'\frac{\partial v_r'}{\partial r}}+\overline{\frac{v_\theta'}{r}\frac{\partial v_r'}{\partial\theta}}\right)-2\omega\overline{v_\theta}=\\ -\frac{\partial\overline{P}}{\partial r}+\mu\left(\frac{\partial}{\partial r}\left(\frac{1}{r}\frac{\partial}{\partial r}\left[r(\overline{v_r})\right]\right)+\frac{1}{r^2}\frac{\partial^2\overline{v_r}}{\partial\theta^2}-\frac{2}{r^2}\frac{\partial(\overline{v_\theta})}{\partial\theta}+\frac{\partial^2\overline{v_r}}{\partial z^2}\right)\end{aligned} \tag{A.31}$$

Recalling the continuity equation for the fluctuating quantities to rearrange the terms in the left-hand side yields:

$$\overline{\frac{1}{r}\frac{\partial}{\partial r}\left(rv_r'v_r'\right)+\frac{1}{r}\frac{\partial}{\partial\theta}\left(v_\theta'v_r'\right)+\frac{\partial}{\partial z}\left(v_r'v_z'\right)}=\overline{\frac{\partial}{\partial r}\left(v_r'v_r'\right)+\frac{v_r'v_r'}{r}+\frac{v_r'}{r}\frac{\partial v_\theta'}{\partial\theta}+\frac{v_\theta'}{r}\frac{\partial v_r'}{\partial\theta}+v_r'\frac{\partial v_z'}{\partial z}+v_z'\frac{\partial v_r'}{\partial z}} \tag{A.32}$$

Expanding the first derivative and evidencing $v_r'$:

$$\overline{\frac{1}{r}\frac{\partial}{\partial r}\left(rv_r'v_r'\right)+\frac{1}{r}\frac{\partial}{\partial\theta}\left(v_\theta'v_r'\right)+\frac{\partial}{\partial z}\left(v_r'v_z'\right)}=\overline{v_r'\left(\cancel{\frac{\partial v_r'}{\partial r}+\frac{v_r'}{r}+\frac{1}{r}\frac{\partial v_\theta'}{\partial\theta}+\frac{\partial v_z'}{\partial z}}\right)+v_r'\frac{\partial v_r'}{\partial r}+\frac{v_\theta'}{r}\frac{\partial v_r'}{\partial\theta}+v_z'\frac{\partial v_r'}{\partial z}} \tag{A.33}$$

Finally, for analogy purposes, it is easier to identify the Reynolds stress-tensor components by representing the viscous stresses in terms of $\tau$. Obviously, for a Newtonian incompressible fluid, the normal stresses vanish. Eq. A.31 becomes:

$$\rho\left(\frac{\partial\overline{v_r}}{\partial t}+\overline{v_r}\frac{\partial\overline{v_r}}{\partial r}+\frac{\overline{v_\theta}}{r}\frac{\partial\overline{v_r}}{\partial\theta}-\frac{\overline{v_\theta}^2}{r}+\overline{v_z}\frac{\partial\overline{v_r}}{\partial z}\right)-2\omega\overline{v_\theta}= \tag{A.34}$$
$$-\frac{\partial\overline{P}}{\partial r}+\left[\frac{1}{r}\frac{\partial}{\partial r}\left(r\overline{\tau}_{rr}\right)+\frac{1}{r}\frac{\partial}{\partial\theta}\left(\overline{\tau}_{\theta r}\right)+\frac{\partial}{\partial z}\left(\overline{\tau}_{zr}\right)-\frac{\overline{\tau}_{\theta\theta}}{r}\right]-\rho\left(\frac{1}{r}\frac{\partial}{\partial r}\left(r\overline{v_r'v_r'}\right)+\frac{1}{r}\frac{\partial}{\partial\theta}\left(\overline{v_\theta'v_r'}\right)+\frac{\partial}{\partial z}\left(\overline{v_r'v_z'}\right)-\frac{\overline{v_\theta'^2}}{r}\right)$$

The $\theta$-component may then be written as:

$$\rho\left(\frac{\partial\overline{v_\theta}}{\partial t}+\overline{v_r}\frac{\partial\overline{v_\theta}}{\partial r}+\frac{\overline{v_\theta}}{r}\frac{\partial\overline{v_\theta}}{\partial\theta}-\frac{\overline{v_rv_\theta}}{r}+\overline{v_z}\frac{\partial\overline{v_\theta}}{\partial z}\right)+2\omega\overline{v_r}= \tag{A.35}$$
$$-\frac{1}{r}\frac{\partial\overline{P}}{\partial\theta}+\left[\frac{1}{r^2}\frac{\partial}{\partial r}\left(r^2\overline{\tau}_{r\theta}\right)+\frac{1}{r}\frac{\partial}{\partial\theta}\left(\overline{\tau}_{\theta\theta}\right)+\frac{\partial}{\partial z}\left(\overline{\tau}_{z\theta}\right)+\frac{\overline{\tau}_{\theta r}-\overline{\tau}_{r\theta}}{r}\right]-\rho\left(\frac{1}{r}\frac{\partial}{\partial r}\left(r^2\overline{v_r'v_\theta'}\right)+\frac{1}{r}\frac{\partial}{\partial\theta}\left(\overline{v_\theta'v_\theta'}\right)+\frac{\partial}{\partial z}\left(\overline{v_z'v_\theta'}\right)+\frac{\overline{v_\theta'v_r'-v_r'v_\theta'}}{r}\right)$$

As for Eq. A.35, by analogy, the $z$-component may be written as:

$$\rho\left(\frac{\partial\overline{v_z}}{\partial t}+\overline{v_r}\frac{\partial\overline{v_z}}{\partial r}+\frac{\overline{v_\theta}}{r}\frac{\partial\overline{v_z}}{\partial\theta}+\overline{v_z}\frac{\partial\overline{v_z}}{\partial z}\right)= \tag{A.36}$$
$$-\frac{\partial\overline{P}}{\partial z}+\left[\frac{1}{r}\frac{\partial}{\partial r}\left(r\overline{\tau}_{rz}\right)+\frac{1}{r}\frac{\partial}{\partial\theta}\left(\overline{\tau}_{\theta z}\right)+\frac{\partial}{\partial z}\left(\overline{\tau}_{zz}\right)\right]-\rho\left(\frac{1}{r}\frac{\partial}{\partial r}\left(r\overline{v_r'v_z'}\right)+\frac{1}{r}\frac{\partial}{\partial\theta}\left(\overline{v_\theta'v_z'}\right)+\frac{\partial}{\partial z}\left(\overline{v_z'v_z'}\right)\right)$$

Therefore, the Reynolds stress-tensor for a cylindrical coordinate system is defined as:

$$\mathbf{R} = -\rho \begin{bmatrix} \overline{v_r' v_r'} & \overline{v_r' v_\theta'} & \overline{v_r' v_z'} \\ \overline{v_\theta' v_r'} & \overline{v_\theta' v_\theta'} & \overline{v_\theta' v_z'} \\ \overline{v_z' v_r'} & \overline{v_z' v_\theta'} & \overline{v_z' v_z'} \end{bmatrix} \tag{A.37}$$

The turbulent kinetic energy $k$ is then obtained from the half of the trace of $\mathbf{R}$:

$$k = \frac{1}{2}\mathrm{Tr}(\mathbf{R}) = \frac{1}{2}\left(\overline{v_r' v_r'} + \overline{v_\theta' v_\theta'} + \overline{v_z' v_z'}\right) \tag{A.38}$$